國立臺灣大學理學院應用物理研究所

博士論文

Graduate Institute of Applied Physics

College of Science

National Taiwan University

Doctoral Dissertation

外延石墨烯中的量子霍爾區域:載流子摻雜、傳輸和應用

Epitaxial graphene in the quantum Hall regime: charge carrier doping, transport, and applications

馬山寧

Swapnil Milind Mhatre

指導教授 ： 梁啟德 博士

Advisor: Chi-Te Liang, Ph.D.

中華民國 111 年 12 月

December 2022

doi:10.6342/NTU202210171

doi:10.6342/NTU202210171

國立臺灣大學博士學位論文
口試委員會審定書

外延石墨烯中的量子霍爾區域：載流子摻雜、傳輸和應用

Epitaxial graphene in the quantum Hall regime: charge carrier doping, transport, and applications

本論文係 馬山寧君 Swapnil Mhatre（D06245006）在國立臺灣大學物理學系、所完成之博士學位論文，於民國 111 年 12 月 20 日承下列考試委員審查通過及口試及格，特此證明

口試委員：

梁啟德（簽名）
（指導教授）

蔡宗惠　呂宥蓉

謝雅萍　莊家翔

doi:10.6342/NTU202210171

doi:10.6342/NTU202210171

Dedicated to my loving parents, dearest sister, friends, and respected teachers.

doi:10.6342/NTU202210171

doi:10.6342/NTU202210171

Abstract

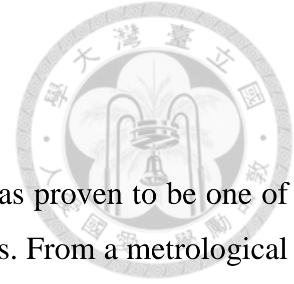

Since the Nobel-prize-winning discovery of graphene in 2004, it has proven to be one of the most important and versatile material due to its extraordinary properties. From a metrological perspective, graphene grown on silicon carbide - known as epitaxial graphene - has been shown to be an ideal platform to build resistance standards. From its robust and precise ν = 2 plateau, to its tunable charge carrier density, and long-term stability, all of its properties make graphene an excellent candidate to build quantum Hall resistance standards. The experiments described in this thesis, further our understanding of graphene in the quantum Hall regime.

We first attempted to use nitric acid as an adsorbent to understand the dynamics of desorption process in epitaxial graphene. The timescales associated with such a process are extracted from the data. This is important in order to fabricate devices with reversible hole doping without the use of a gate. Transport properties were measured on several devices post-nitric- acid-exposure at temperatures between 300 K and 1.5 K. In order to replicate the laboratory conditions, ambient conditions are applied. This would help in recreating similar conditions as to the ones in a laboratory when such devices are handled using this type of chemical vapor doping. Raman spectroscopy is used as a comparative tool to verify the timescales extracted from the transport measurements.

Hot electrons are expected to cause local disruption of quantized conduction in two-dimensional systems and may lead to breakdown of the quantum Hall effect. The extent of local heating is generally limited to small regions near contacts where a large current enters and leaves the device, since the existence of the electrochemical potential that produces the Hall voltage is established at these points. We investigated the effect of current introduced at downstream points near where the Hall voltage is typically measured. For contact separation as small as a few micrometers we did not observe substantial interactions due to the internal distribution of current, even when a resistance of hundreds of ohms of is generated by dissipation at the side contacts.

Using the above knowledge, the limiting factors for developing metrology grade epitaxial graphene quantum Hall arrays are lifted with a combination of the implementation of closely spaced superconducting contacts, high-quality material, and centimeter-scale growth. The ν = 2

doi:10.6342/NTU202210171

Landau level has been the basis of a single quantized value that modern day resistance standard devices have been restricted to. Here, we demonstrate multiple quantized values from our devices, which could be used to disseminate the ohm all around the world. These devices are designed such that they give access to quantized resistances values from the standard 12.9 kΩ to more than three orders of magnitude, as high as 1.29MΩ. Several experimental methods such as Raman spectroscopy and standard electrical characterization using lock-in amplifier techniques are employed herein to verify the quality and demonstrate the versatility of these devices.

doi:10.6342/NTU202210171

Acknowledgements

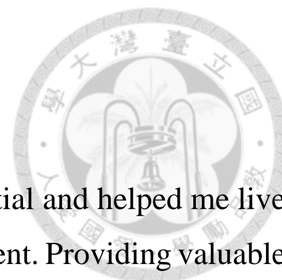

I would like to thank Prof. Chi-Te Liang who believed in my potential and helped me live up to it over the years. As a supervisor, guide, and mentor he has been excellent. Providing valuable feedback and engaging in scientific discussions, all of which enhanced my knowledge and capabilities. His friendly and patient nature helped when I would ask him some of the dumbest possible questions and he would still help me arrive at the correct answers. The football related conversations were always fun. His guidance regarding experimental methods was crucial for all my experiments at NIST, he shaped my experimental aptitude and skills with his hands on yet hands off approach while I was working on graphene nanoribbons. The weekly presentations with the lab group at NTU were crucial in improving my presentation skills. They taught me how to efficiently disseminate an article and present it in a clear and concise manner. The group members throughout the years, both Masters and PhD students were wonderful people. Their welcoming and friendly attitude helped me comfortably settle in an unfamiliar country when I first joined the group.

Dr. Randolph Elmquist played a crucial role in my growth at NIST. The discussions with him helped me understand the workings of the Janis cryostat at a much deeper level. I learnt so many useful experimental skills through him. The current distribution project was a wonderful time, where he would enthusiastically join in while performing the measurements and we would spend a good amount of time pondering over the results and trying to interpret them. Dr. Albert Rigosi's kind guidance cannot be understated. I am amazed at the speed at which he proposes an idea, designs the experiment and guides us to the results. The nitric acid doping study and the 1.29MΩ array project would not have been possible without his guidance.

A huge thank you to Dr. Dinesh K. Patel for being a mentor, a confidant, and a close friend. Whatever the problem maybe, Dinesh always has a solution or advice for it. Over the years, having engaging scientific discussions, bouncing off random ideas for experiments and discussing everything under the sun with him was extremely fruitful. Since before I landed in Taiwan, he helped me assimilate the local culture and introduced me to many folks from my home country, India. If it were not for him, the last 5 years would have been much more difficult for me. His wife,

doi:10.6342/NTU202210171

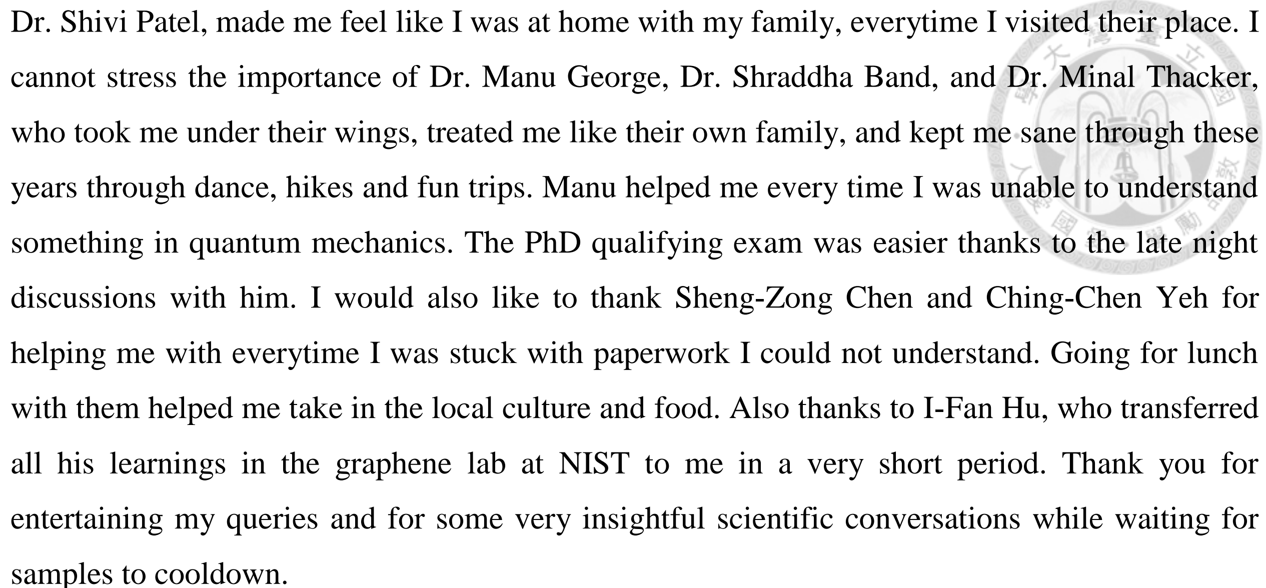

Dr. Shivi Patel, made me feel like I was at home with my family, everytime I visited their place. I cannot stress the importance of Dr. Manu George, Dr. Shraddha Band, and Dr. Minal Thacker, who took me under their wings, treated me like their own family, and kept me sane through these years through dance, hikes and fun trips. Manu helped me every time I was unable to understand something in quantum mechanics. The PhD qualifying exam was easier thanks to the late night discussions with him. I would also like to thank Sheng-Zong Chen and Ching-Chen Yeh for helping me with everytime I was stuck with paperwork I could not understand. Going for lunch with them helped me take in the local culture and food. Also thanks to I-Fan Hu, who transferred all his learnings in the graphene lab at NIST to me in a very short period. Thank you for entertaining my queries and for some very insightful scientific conversations while waiting for samples to cooldown.

Thank you to all the NTU group members throughout the years for their help and support, especially Sheng-Zong Chen, Ching-Chen Yeh, Hao-Chen Yeh, Pin-Chi Liao, I-Fan Hu, Wei-Chen (big and small), Yun-Wu, Pin-Hsuan Lai, Guan-Ming, and Dr. Bi-Yi Wu. Thank you to the NIST Resistance group members, Dr. Dipanjan Saha, Dr. Ngoc Mai Tran, Shamith Payagala, Charles Perera, Alireza Panna, and others for organizing Thai food Fridays, and spending that one afternoon talking about everything other than work. Thanks to Dr. David Newell, and Dr. Dean Jarrett for leading the weekly group meetings and keeping a close eye on my research progess, and for proving valuable inputs. They would also offer help with any problems I was facing. Thanks to Gail Griffin-Ferris for the efficient and fast official paperwork. Thanks to Dr. Myra Liu and Dr. Dipanjan Saha for teaching me the basic cleanroom skills and walking me through the graphene device fabrication process. Thanks for Dr. Yanfei Yang for the engaging conversations about graphene growth and for the continuing help in growing good quality graphene. Thanks Dr. Ngoc Mai Tran for help with the precision measurements and the nitric acid doping experiments.

I owe one of the biggest thanks -to the person who inspired me to take up research as a career- Dr. E. S. Kannan from the department of Physics, BITS Pilani Goa campus. Undertaking a thesis project under him for my Master's degree was a life changing experience. He not only saw my potential, but also helped me gain some very important knowledge about the quantum Hall effect, a major component of this thesis.

doi:10.6342/NTU202210171

Finally, the most important people in my life, my amazing parents and my dear sister. Their support has been the constant and unwavering. Thank you for all your love and for believing in me. This would not have been possible without every single person mentioned in this acknowledgement. I thank them all, once again.

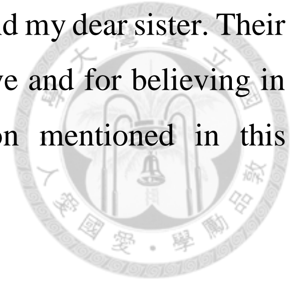

doi:10.6342/NTU202210171

List of Publications:

Directly related to the thesis:

[1] **S. M. Mhatre**, N.T.M. Tran, H.M. Hill, D. Saha, A.R. Hight Walker, C.-T. Liang, R.E. Elmquist, D.B. Newell, A.F. Rigosi, Dynamics of transient hole doping in epitaxial graphene, Physical Review B, 105 (2022) 205423.

[2] **S. M. Mhatre**, N. T. M. Tran, H. M. Hill, C.-C. Yeh, D. Saha, D. B. Newell, A. R. Hight Walker, C.-T. Liang, R. E. Elmquist, and A. F. Rigosi , "Versatility of uniformly doped graphene quantum Hall arrays in series", AIP Advances 12, 085113 (2022).

Other Publications:

[1] N.T.M. Tran, **S. M. Mhatre**, C.N. Santos, A.J. Biacchi, M.L. Kelley, H.M. Hill, D. Saha, C.-T. Liang, R.E. Elmquist, D.B. Newell, B. Hackens, C.A. Hacker, A.F. Rigosi, Desorption timescales on epitaxial graphene via Fermi level shifting and Reststrahlen monitoring, Carbon N Y, 197, 350-358 (2022).

[2] S.-Z. Chen, J.-W. Yang, T.-Y. Peng, Y.-C. Chu, C.-C. Yeh, I.F. Hu, **S.M. Mhatre**, Y.-J. Lu, C.-T. Liang, Disorder-induced 2D superconductivity in a NbTiN film grown on Si by ultrahigh-vacuum magneton sputtering, Superconductor Science and Technology 35, 064003 (2022).

[3] O.Z. Farinre, H. Alghamdi, **S. M. Mhatre**, M.L. Kelley, A.J. Biacchi, A.V. Davydov, C.A. Hacker, A.F. Rigosi, P. Misra, Comprehensive Data via Spectroscopy and Molecular Dynamics of Chemically Treated Graphene Nanoplatelets, Data 7, 38 (2022).

[4] P. K. Roy, R. K. Ulaganathan, C. M. Raghavan, **S. M. Mhatre**, H. I. Lin, W. L. Chen, Y.-M. Chang, A. Rozhin, Y.-T. Hsu, Y.-F. Chen, R. Sankar, F.-C. Chou, C.-T. Liang , Unprecedented random lasing in 2D organolead halide single-crystalline perovskite microrods, Nanoscale 12 (35), 18269-18277 (2020)

doi:10.6342/NTU202210171

Table of contents

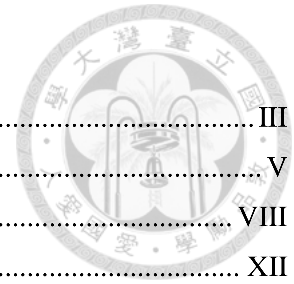

Abstract.. III

Acknowledgements V

List of Publications: VIII

List of Figures: XII

List of abbreviations:.. XV

Chapter 1 Introduction.. 1

1.1 Objective and Structure 1

1.2 History.. 2

1.3 Graphene 3

1.4 Epitaxial Graphene.. 5

1.5 Modulating carrier density 6

Chapter 2: Magneto-transport effects.. 8

2.1 Classical Hall Effect.. 8

2.2 Landauer-Büttiker Formalism 11

2.2.1 Landau levels.. 11

2.2.2 Landauer-Büttiker formalism 14

2.2.3 The Landauer formula 17

2.2.4 The Landauer formula for multiprobe systems 20

2.3 Quantum Hall Effect.. 21

2.4 Integer quantum Hall effect in EG.. 24

2.5 Edge States.. 25

2.6 Hot Spots.. 27

2.7 DC Equivalent circuits 29

2.7.1 Double series connections.. 30

2.7.1 Triple series connections 32

Chapter 3 Experimental design and instrumentation 33

3.1 Silicon Carbide (SiC) 33

3.1.1 Patterning a SiC substrate 34

3.1.2 Dicing SiC 35

3.1.3 Cleaning the pieces.. 36

3.2 Epitaxial Graphene Growth and Doping.. 37

3.2.1 Polymer Assisted Sublimation Growth.. 37

3.2.2 Confocal Microscopy 38

doi:10.6342/NTU202210171

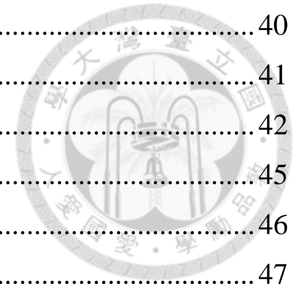

3.2.3 $Cr(CO)_3$ functionalization 40
3.2.4 Nitric Acid Doping 41
3.3 Fabrication of Graphene Devices 42
3.4 Raman Spectroscopy 45
3.5 Electrical and Magneto-Characterization 46
3.5.1 Basic electrical measurements 47
3.5.2 Current Sources and Voltmeters 48
3.5.3 Janis Cryostat 48
Chapter 4 Dynamics of Transient Hole Doping in Epitaxial Graphene 51
4.1 Experimental description 51
4.2 Transport and transient doping 53
4.3 Langmuir modelling and Raman monitoring 61
4.3.1 Three-Species Langmuir Model 61
4.3.2 Monitoring the 2D (G') Raman Mode 63
4.4 Illustration of dopant interaction 66
Chapter 5 Current Distribution in graphene quantum Hall devices 68
5.1 Device description 69
5.2 Contact and Longitudinal resistance 71
5.3 Current Distribution 73
Chapter 6 Versatility of uniformly doped graphene quantum Hall arrays in series 78
6.1 Device description 79
6.2 Raman Spectra 80
6.3 Hall transport measurements 82
6.4 Precision measurements 85
References: 89

doi:10.6342/NTU202210171

doi:10.6342/NTU202210171

List of Figures:

Figure 1.1: Crystal structure of Graphene

Figure 1.2: The experimental steps leading to the formation of monolayer epitaxial graphene on SiC

Figure 2.1: Edwin Hall's Hall data.

Figure 2.2: The Hall Effect.

Figure 2.3: The first quantum Hall data.

Figure 2.4: A 2DEG realized.

Figure 2.5*:* Formation of LL in 2D density of states

Figure 2.6*:* Two-terminal phase coherent conductance

Figure 2.7: A Hall Bar with idea contacts

Figure 2.8: Quantum Hall effect and the density of states in Graphene

Figure 2.9: Edge states in graphene**.**

Figure 2.10: Hot spots in QHE

Figure 2.11: Application of Hot spots.

Figure 2.12: The DC equivalent circuit.

Figure 2.13: Double-series connection of a quantum Hall system

Figure 2.14: Circuit for a triple series connection.

Figure 3.1: Structure of SiC

Figure 3.2: SiC alignment marks and dicing pattern.

Figure 3.3: Interference fringes on SiC chips.

Figure 3.4: Comparison of an optical microscope vs a CLSM.

doi:10.6342/NTU202210171

Figure 3.5: Nitric acid doping assembly.

Figure 3.6: Contact lithography masks for Hall bar devices

Figure 3.7: Graphene device fabrication process.

Figure 3.8: Chip carriers.

Figure 3.9: The Janis cryogenic system.

Figure 4.1 Devices for the Nitric Acid doping experiment and the EG quality

Figure 4.2: Transport and electrical data for the doping experiments.

Figure 4.3: Extracting time constants

Figure 4.4: Exponential decay analysis

Figure 4.5: Exponential decay analysis II

Figure 4.6: Spectroscopic verification of observed time constants

Figure 4.7: Illustrations of dopant interactions

Figure 5.1: Current distribution device designs.

Figure 5.2: Contact resistance as a function of the applied current**.**

Figure 5.3: Longitudinal resistance as a function of current

Figure 5.4: Circuit diagrams for the double series arrangement.

Figure 5.5: Measured currents in multi-series circuits

Figure 5.6: Longitudinal resistance in a double series connection compared with the deviation in Hall resistance.

Figure 6.1:1.29 MΩ Array

Figure 6.2: Raman analysis of the 1.29 MΩ Array.

Figure 6.3: Hall data for 1.29 MΩ

Figure 6.4: Precision measurement data for the first 51 elements of the array**.**

doi:10.6342/NTU202210171

doi:10.6342/NTU202210171

List of abbreviations:

- EG Epitaxial Graphene
- IQHE Integer Quantum Hall Effect
- LEED Low-energy electron diffraction
- HR-TEM High Resolution Transmission Electron Microscope
- HOPG Highly Ordered Pyrolytic Graphite
- QHRS Quantum Hall Resistance Standard
- CVD Chemical Vapor Deposition
- MOSFET Metal Oxide Semiconductor Field Effect Transistor
- LL Landau Levels
- MSR Mesoscopic Region
- 2DEG Two-Dimensional Electron Gas
- NIST National Institute of Standards and Technology
- HS Hot Spot
- CCC Cryogenic Current Comparator
- CNST Center for Nanoscience and Technology
- PASG Polymer Assisted Sublimation Growth
- CLSM Confocal Laser Scanning Microscope

doi:10.6342/NTU202210171

Chapter 1 Introduction

This chapter introduces the core component of this thesis, graphene. It also explores the history of graphene and arrives at its application with respect to this thesis. It provides a rough idea of what to expect in the later chapters of this thesis.

1.1 Objective and Structure

For the advancement of quantum Hall resistance metrology, it is important to understand and study how the materials we work with, behave under various conditions. It is also important to understand how we can control the materials and their behavior, in order to accommodate them in the future designs. The material at the center of this thesis is graphene, more specifically, epitaxial graphene (EG) grown on silicon carbide. This thesis aims to investigate how to reliably, and reproducibly modulate the carrier density of EG. This study further explores how the current behaves in the quantum Hall regime at low temperatures and in order to do so, pushes the limits of closely spaced contacts. It also explores how we can apply this knowledge to actual resistance standards.

This introductory Chapter **1** gives the readers a glimpse into what this wonder material called graphene is, followed by a more specific introduction to EG. We then peek into EG device fabrication and briefly discuss its doping. Chapter **2** provides a brief introduction to the classical Hall effect and then goes into the quantum Hall effect. The edge state picture and the integer quantum Hall effect (IQHE) are also discussed. Chapter **3** discusses the basic experimental procedures followed in this thesis and the various tools and instruments used to these experiments. It also discusses in detail the fabrication of EG devices.

Chapter **4** makes an in-depth dive into understanding the doping process for EG using an adsorbent in the form of nitric acid vapors. The process is analyzed through extracting various timescales from the experimental data and using it for modelling. It is then compared with the

doi:10.6342/NTU202210171

results from Raman spectroscopy. Chapter **5** describes the experiments performed to understand the current distribution in specially prepared close contact EG devices. The influence of hot spots and various resistances is described and the limits of scaling down EG resistance standards are pushed. Chapter **6** details the procedures for scaling the EG resistance standards. The magnetoresistance data and some precision measurements are discussed. Finally, a brief overview of the thesis, results, and future outlook are given in Chapter **7**.

1.2 History

In 1859, Benjamin Brodie discovered a new form of carbon called "graphon". Today we know this material as graphene oxide [1]. Boehm *et al*. published a paper titled, "Die Dünnste Kohlenstoff-Folien" - which translates quite literally to, "The thinnest carbon layers" -, where they looked at single layers of carbon [2, 3]. The term 'graphene', was later coined by Boehm *et al*. in 1986, where the first part of the word was derived from graphite and 'ene' was added to emphasize the polycyclic aromatic hydrocarbons [4]. The first graphitization of silicon carbide was patented in 1896 by Acheson [5]. This discovery of X-rays during this period boosted the study of crystal structures of various materials. It was however, in 1965, more than half a century later that X-rays were used to study the thermal decomposition of SiC, where Badami identified epitaxial graphene on SiC and published his study on the crystal structure on a 6-H SiC [6]. 10 years later, Van Bommel et al. investigated the graphite on SiC. This was obtained by sublimation of Si-atoms of SiC in high-vacuum. A low-energy electron diffraction (LEED) analysis revealed the so-called buffer layer, a $(6\sqrt{3} \times 6\sqrt{3})R30°$ surface reconstruction [7].

Looking back, they were so close to finding the wonder material, however, the unique properties of this freestanding layer was not discovered yet. Direct visualization of the thin graphene layer on the Si-face of SiC could directly be visualized using high-resolution transmission electron microscopy (HR-TEM) [7]. In 2004, there was a breakthrough, Berger *et al*. published a study that led to increasing interest in this area [8]. Then came a massive turning point,

doi:10.6342/NTU202210171

graphene flakes were isolated using mechanical exfoliation of highly ordered pyrolytic graphite (HOPG) by Geim and Novoselov in 2004. This work won them the Nobel prize in Physics in 2004 [9, 10].

The exfoliation of graphite led to numerous studies about the unique nature of graphene [11, 12]. However, there were many drawbacks, from the reproducibility, thickness control, to the small and uncontrollable sizes of the flakes. This led to a shift in focus towards EG on SiC. In-situ growth of EG was known to produce a rough graphene at the time. In 2008, EG growth was achieved in ambient argon environment with improved graphene layers [13, 14]. Quasi-freestanding monolayer graphene was obtained by annealing in hydrogen atmosphere, where the buffer layer turned into a monolayer [15].

In 2010, Tzalenchuk *et al*. introduced a consequential application of EG, as the quantum Hall resistance standard (QHRS). This encouraged the metrology groups to explore the use of EG as a replacement for the GaAs/AlGaAs heterostructures [16]. Various improvements were made to improve the growth of EG on SiC [17, 18]. Modern day QHRS using EG have shown long term electrical stability in ambient conditions. Their ability to output a single value of quantized resistance makes them an important material in metrology [19]. In pursuit of making the most out of this wonder material, EG provides an excellent platform to study the quantum Hall effect, a by-product of which is its application in metrology.

1.3 Graphene

Graphene is a single sheet of carbon atoms in a honey-comb structure. It exhibits excellent electronic, thermal and optical properties. It is a unique material because there are many other materials which are as conducting or as transparent as graphene, however, materials which are simultaneous conducting, transparent, and flexible are rare. Carbon is the 4th most abundant element in the world, of which graphene is an allotrope. It is low cost and sustainable and its two

doi:10.6342/NTU202210171

dimensional (2D) structure allows it to be readily integrated into the mainstream technological applications [12].

Two carbon atoms with sp^2 hybridization make up the unit cell of graphene. Due to this, three sp^2 hybridized orbitals are at a 120° angle relative to each other, resulting in a honeycomb structure or a hexagonal lattice structure (Figure 1.1(a)). Four electrons in the valence band are present in the carbon atoms of graphene. Three sp^2 hybridized planar orbitals are formed from these electrons to their adjacent carbon atoms through sigma bonds. The fourth electron bonds to the neighboring carbon atoms through a covalent out of plane pi-bond. Such a bonding structure makes graphene one of the most mechanically stable material. The pi bonded states provide the unique electrical properties and interlayer coupling to graphene. More importantly, the excellent electronic properties are from the delocalized electrons in its π-system [20].

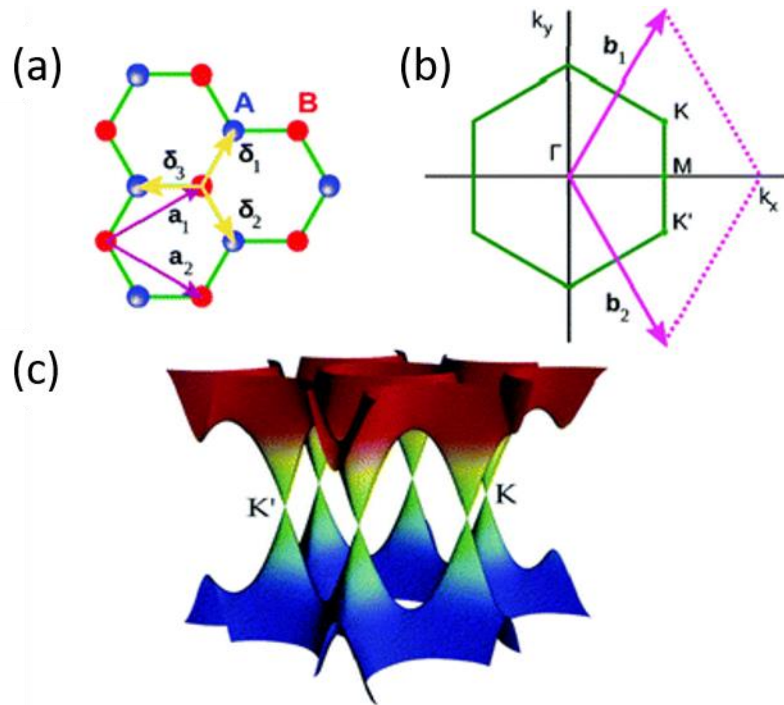

Figure 1.1: Crystal Structure of graphene: ***(a)*** *a_1, a_2 are the lattice unit vectors, and δi, i = 1,2,3 are the nearest-neighbour vector which show the hexagonal crystal lattice of graphene.* ***(b)*** *This figure shows the first brillioun zone of graphene. The Dirac cones are located at the K and K' points.* ***(c)*** *The energy dispersions of graph.(Taken from Ref. [21])*

doi:10.6342/NTU202210171

Simple nearest-neighbour tight-binding approximation is used to calculate the band structure of graphene. The bandgap of graphene is exactly zero, this can be inferred from the conduction band and the valence band meeting at the Dirac points, or the K-K' points, also known as the charge neutrality points. (Figure 2.1(b) and (c)). At the Dirac points, graphene's band spectrum is quite similar to the Dirac spectrum for massless fermions. Thus, graphene is considered a gapless semi-conductor. Accordingly, the energy-dispersion spectra shows a linear behavior ($E \propto k$), as opposed to the $E \propto k^2$ in conventional semi-conductors [21].

1.4 Epitaxial Graphene

Graphene can be produced in numerous ways. Mechanical exfoliation of HOPG was one of the first ways to produce it. Although it produces high-quality graphene, it was not fit for industrial use. Liquid phase exfoliation of graphite was attempted, wherein, the graphite is dissolved in a solvent and through sonication, one can produce flakes of monolayer graphene. A high yielding method with low quality graphene [22]. The most commonly used and 'industry-scalable' method to produce graphene is the chemical vapor deposition (CVD) method [23]. CVD graphene can be grown on various metals like Ni [24], and Ir [25]. The most commonly used metal us Cu [26]. However, this method again suffers from drawbacks like a high chance of contamination and having a risk of damaging the monolayer graphene during transfer [27].

EG on the other hand, requires no transfer and is formed directly on the surface. It requires no further contamination from acids or polymers to be used. EG is grown by annealing a SiC substrate in argon atmosphere at temperatures up to 1900°C. At these temperatures, the Si atoms sublimate, leaving behind a single sheet of carbon atoms. This takes place in three stages: (i) An initial Si sublimation that takes place in an inductively heated graphite furnace filled with argon at 1atm pressure. (ii) Buffer layer formation: C-rich $6\sqrt{3} \times 6\sqrt{3}$ R30° surface reconstruction of (0001) face of 4H-SiC. (iii) Final formation: topmost graphene layer is formed above the buffer layer [28]. These are illustrated in figure 1.2. A more in-depth discussion follows in Chapter 3.

doi:10.6342/NTU202210171

Another popular way to grow graphene is using the chemical vapor deposition technique, wherein graphene is deposited onto a copper substrate in a uniform manner using vapors from a carbon source. This means that in order to use this graphene for practical purposes, it has to be transferred onto an insulating substrate, typically using a sacrificial polymer layer. This polymer layer leaves a residue which negatively affects the electrical properties of the graphene. Transferring it also leads to line defects forming on the graphene. All these factors make CVD graphene non-ideal for quantum Hall metrology purposes, when compared to Epitaxial graphene.[29]

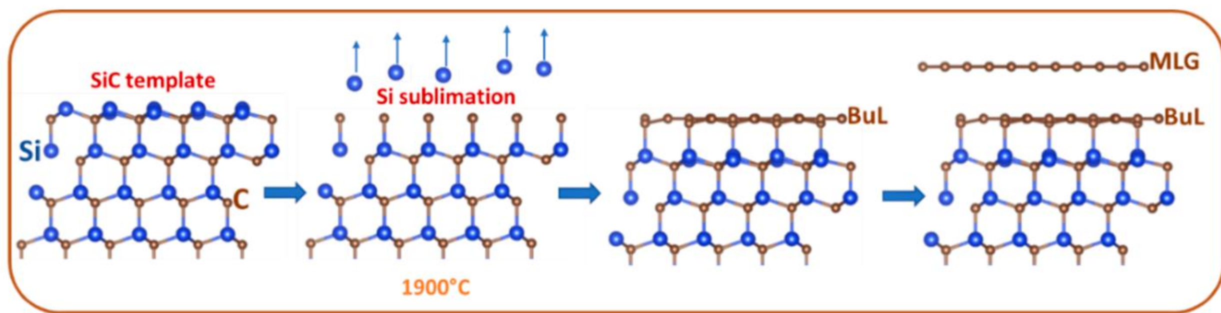

Figure 1.2*: An illustration of steps leading to the formation of monolayer epitaxial graphene on SiC. This schematic has been adapted from Ref. [28].*

1.5 Modulating carrier density

A carbon lattice in graphene is a very effective pathway for charge carriers. An introduction of a heteroatom is an effective way to modulate its carrier density. Atoms such as those of B, N, P, *etc*, disrupt the lattice and create a strong polarization in the carbon network [30]. This is due to the differences in electronegativities of boron (2.04), oxygen (3.44), nitrogen (3.04), and carbon (2.55). These disruptions modulate the electrical, chemical, and optical properties of graphene. A downside to these disruptions are that they create charge scattering centers, thereby degrading the extraordinary properties of graphene. There are *in-situ* (during synthesis) and *ex-situ* (post-synthesis) ways of achieving this. An example of an *in-situ* approach would be the production of

doi:10.6342/NTU202210171

nitrogen doped graphene through CVD by using NH_3 as one of the precursors. Here, the controlled number of N atoms from the precursor form covalent bonds with the graphene [31]. An example of an *ex-situ* process would be that used by Wu *et al*. [32], wherein they used C_3N_4 while annealing as a dopant source to achieve n-type doping in CVD graphene. Light is also offers a way to stimulate switching between two conductive states in graphene. It is a form of reversible doping. A simple example would be the work of Luo *et al.* [33], where they used deep UV light (λ = 220 nm) to dope graphene with a p-type carriers with very little damage to its crystal structure.

Although substitutional doping is advantageous, it is usually followed by a substantial decrease in carrier mobility due to defects and disorders in graphene. This hinders practical applications on an industrial scale, such as field effect transistors (FETs). Which leads us to another form of carrier modulation which takes a non-covalent anchoring approach. Adsorption of dopant molecules on the surface of graphene leads to interfacial events which allow for modulation without damaging the integrity of the graphene structure. A popular among metrologist working with graphene QHRS is to use $Cr(CO)_3$ as a functionalizing agent on the graphene surface which provides a reversible and controllable carrier density on EG [34]. A more detailed explanation and methodology is offered in chapter 3 on this process. A much simpler way would be to expose the EG to nitric acid vapors, a method which is a core element of chapter 4 of this thesis [35].

doi:10.6342/NTU202210171

Chapter 2: Magneto-transport effects

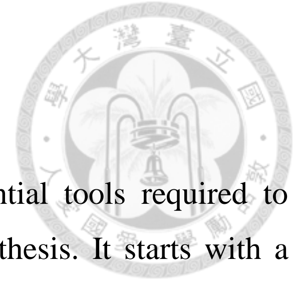

This chapter is an attempt to fill the readers toolkit with essential tools required to mathematically tackle the results presented in the core chapters of this thesis. It starts with a quantitative description of the classical Hall effect, followed by an introduction to the Landauer-Büttiker formalism which is then used to arrive at the quantum Hall effect. The concepts of hot spots is then introduced along with the circuit equations for the series connections for a quantum Hall system.

2.1 Classical Hall Effect

The Hall effect was discovered by Edwin Hall, a Johns Hopkins University graduate student, in 1879. He passed a current through a thin gold leaf sheet and measured two characteristic voltages, shown in Figure 2.1. The first voltage measured was along the current path, which when divided by the current, gave the electrical resistance of the material, R. The second voltage measured, was *across* the current path, denoted as V_H, which was expected to be zero since, intuitive thinking would point that the current, I, was perpendicular to it. This was until Hall applied a magnetic field perpendicular to the metal sheet. A non-zero V_H was observed when such a field was applied. V_H was proportional to both, I and B. Hence, an electrical resistance, R_H, yielded $R_H \propto B$. Ever since, this phenomenon is known as the Hall effect. The associated voltage

doi:10.6342/NTU202210171

and resistance became the Hall voltage and Hall resistance, respectively.

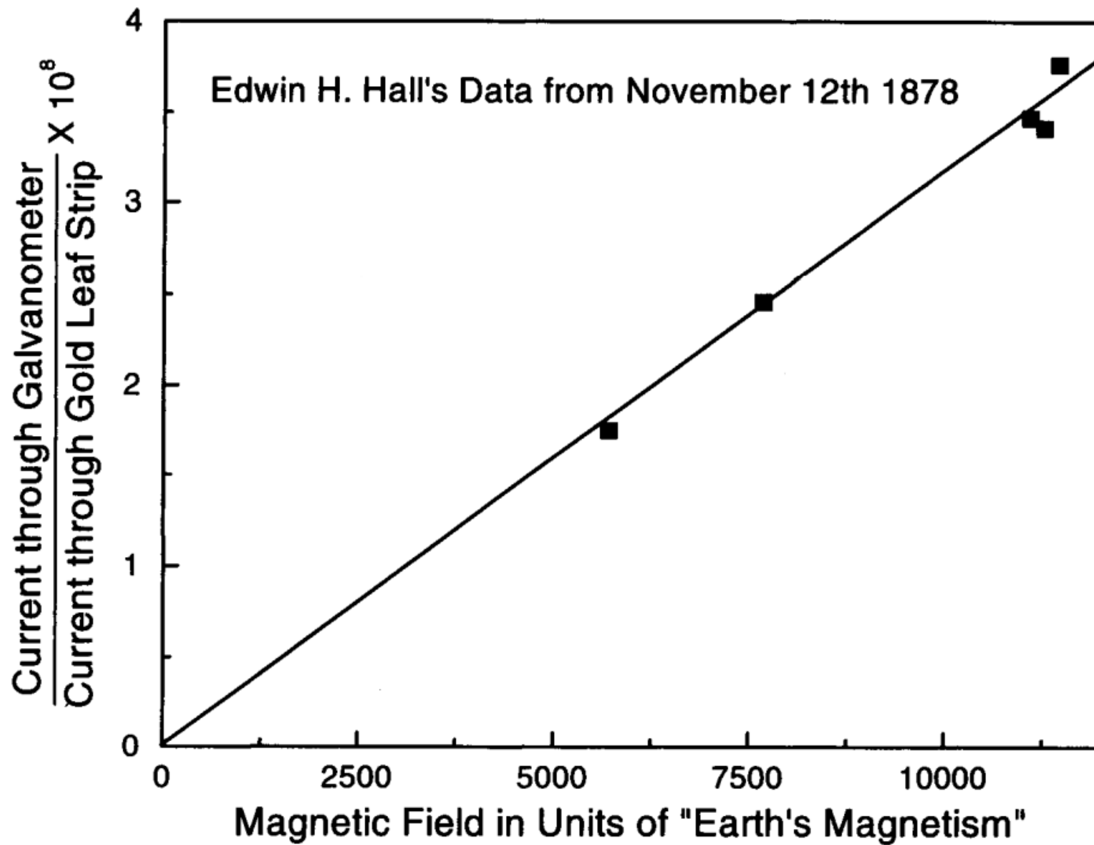

Figure 2.1: Edwin Hall's Hall data. As plotted from a table in his report by H.L. Stromer in his Nobel lecture.[36]

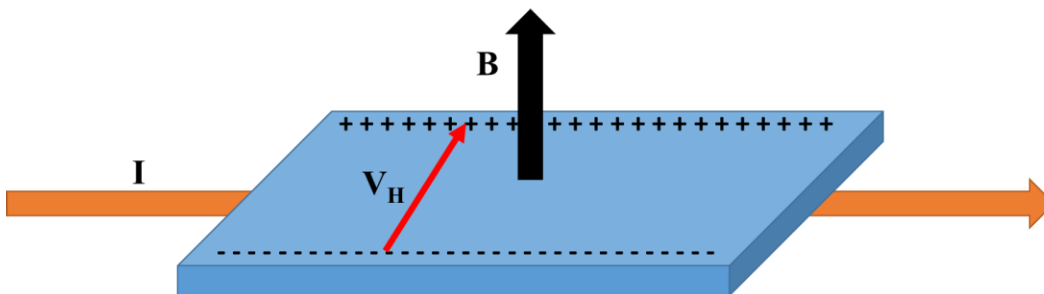

***Figure 2.2: The Hall Effect**. The electrons moving along the conductor are curved due to the perpendicular magnetic field and hence accumulate on one side and build up a potential difference know as the Hall voltage V_H. In case of hole carriers, it is a similar situation, with the exception that the Hall voltage has the opposite sign.*

doi:10.6342/NTU202210171

The presence of a magnetic field exerts a Lorentz force onto the electrons, which otherwise move in the direction of the current. This force causes the electrons to move in a circle with a cyclotron frequency $\omega_c = eB/m^*$, where m^* is the effective mass of the charge carriers. The carriers propagate to the edges of the sample leading to the buildup of charges as shown in figure 2.2, thus leading to the Hall voltage, V_H. The Hall voltage can be expressed as:

$$V_H = \frac{IB}{nte} \quad , \tag{2.1}$$

where n is the charge carrier density in three dimensions (3D), t is the thickness, and e is the charge of an electron. A Hall measurement allows us to determine a materials charge carrier density and its type of charge carriers. This effect can be described mathematically using the Drude model. In this model, the electrons are considered free and experience no coulomb interactions, while moving for a collision time τ before scattering. When such an electron is placed in an electromagnetic field, the equation of motion can be written as:

$$m\frac{dv_d}{dt} = -e(\boldsymbol{E} + v_d \times \boldsymbol{B}) - \frac{mv_d}{\tau} \quad , \tag{2.2}$$

where v_d is the drift velocity. There is no change in velocity for a stationary state, and for a 2D system, the electric fields are given by:

$$\begin{pmatrix} E_x \\ E_y \end{pmatrix} = \begin{pmatrix} \frac{-m}{e\tau} & -B \\ B & \frac{-m}{e\tau} \end{pmatrix} \begin{pmatrix} v_{d,x} \\ v_{d,y} \end{pmatrix} \quad , \tag{2.3}$$

$$= \begin{pmatrix} \frac{m}{e^2\tau n_e} & \frac{B}{n_e e} \\ \frac{-B}{n_e e} & \frac{m}{e^2\tau n_e} \end{pmatrix} \begin{pmatrix} j_x \\ j_y \end{pmatrix} \quad , \tag{2.4}$$

where the current density is $j = -en_e v_d$, with n_e being the carrier density, more specifically in this case, the electron density. In a stationary state, there is no current flowing in the y-direction. Hence, from the resistivity tensor in equation 2.4, we can find the so-called longitudinal and Hall resistivities as:

doi:10.6342/NTU202210171

$$\rho_{xx} = \frac{m}{e^2 n_e \tau} = \frac{1}{\sigma_0} \quad , \tag{2.5}$$

$$\rho_{xy} = -\frac{B}{en_e} \quad , \tag{2.6}$$

Thus, the Hall resistance being proportional to the magnetic field, there is no magnetoresistance in the x-direction. The constant R_H is denoted as the Hall coefficient and can be written as $R_H = E_y/j_xB = -1/en_e$.

2.2 Landauer-Büttiker Formalism

Before we dive into the quantum Hall effect, we need to understand some mathematical formalisms which we would be using to arrive at the quantum Hall effect. This section deals with the important Landauer-Büttiker formalism.

2.2.1 Landau levels

A 2D electron gas (2DEG) is an electron gas that is quantized in one dimension but free to move in the other 2 dimension. Such a system in the late 20th century, could be realized in between an intrinsic (GaAs) semiconductor and *n*-type (AlGaAs) (Figure 2.3). The conduction band is below Fermi energy in the junction, but the Fermi energy is between the conduction bands and the valence. The electrons are confined to two dimensions at sufficiently low temperatures, that is their movement is quantized in the z-direction. With inspiration from [37, 38], we now take a look at the quantum mechanical approach to understanding how Landau levels are formed in a 2DEG under a magnetic field.

doi:10.6342/NTU202210171

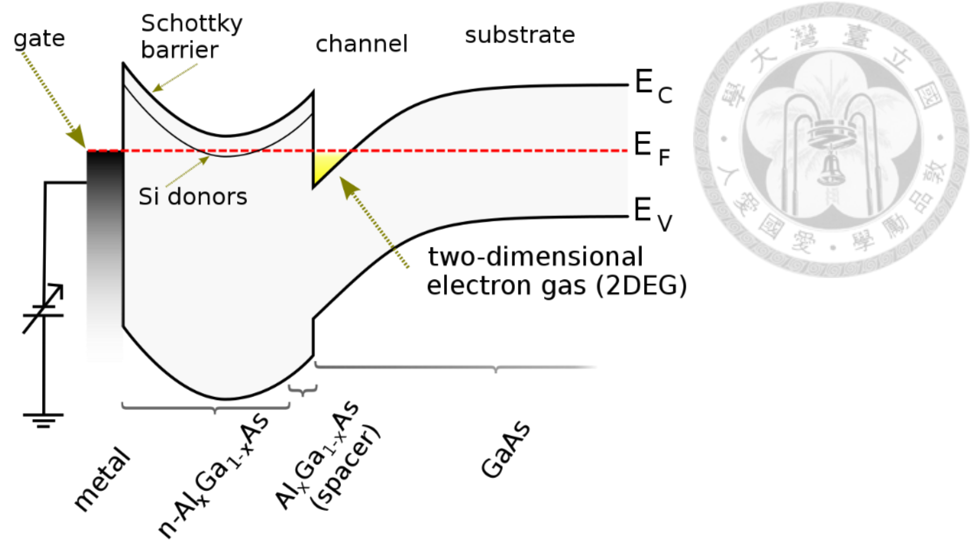

Figure 2.3: A 2DEG realized*. Band diagram of a GaAs/AlGaAs heterojunction showing the formation of a 2DEG. Adapted from Wikipedia.*

We use the kinetic momentum $\boldsymbol{p} + e\boldsymbol{A}$ instead of the canonical momentum $\boldsymbol{p}$, where $\boldsymbol{A}$ is the vector potential in order to incorporate the Lorentz force into the Hamiltonian. The magnetic field is given by the curl of the vector potential. When we consider non-interacting free electrons in a magnetic field

$$\frac{1}{2m}\left(\frac{\hbar}{i}\Delta + e\boldsymbol{A}\right)^2 \psi(\boldsymbol{r}) = \varepsilon\psi(\boldsymbol{r}) \qquad , \qquad (2.7)$$

Different vector potentials can be chosen for a magnetic field in the z-direction, such as the symmetric gauge $A = \frac{1}{2}B_0(-y, x, 0)$ and the Landau gauge $\boldsymbol{A} = B_0(0, x, 0)$. Here we use the landau gauge. For a 2D system, the Hamiltonian then becomes

$$H = \frac{p_x^2}{2m} + \frac{\left(P_y + exB_0\right)^2}{2m} \qquad , \qquad (2.8)$$

$$= \frac{p_x^2}{2m} + \frac{p_y^2}{2m} + \frac{1}{2}m\omega_c^2 x^2 + p_y\omega_c x \qquad , \qquad (2.9)$$

doi:10.6342/NTU202210171

where $\omega_c = \frac{eB_0}{m}$ is the cyclotron frequency. By using the wavefunction for free particle in the y-direction,

$$\psi(x,y) = u(x)e^{ik_y y} \tag{2.10}$$

The energy can be calculated as follows:

$$H\psi = e^{ik_y y}\left(\frac{p_x^2}{2m} + \frac{(\hbar k_y)^2}{2m} + \frac{1}{2}m\omega_c^2 x^2 + \hbar k_y \omega_c x\right)u(x) = \varepsilon u(x)e^{ik_y y} \tag{2.11}$$

$$\left(\frac{p_x^2}{2m} + \frac{1}{2}m\omega_c^2(x + l_0^2 k_y)^2\right)u(x) = \varepsilon u(x) \quad , \tag{2.12}$$

wherethe magnetic length is, $l_0 = \sqrt{\frac{\hbar}{m\omega_c}}$. The above equation is known as the Schrödinger equation for a 1-D harmonic oscillator with frequency ω_c centered around $x_0 = -l_0^2 k_y$. Thus, under the influence of a magnetic field, the energy of electrons becomes discreet as:

$$\varepsilon_n = \left(n + \frac{1}{2}\right)\hbar\omega_c \quad , \tag{2.13}$$

where n = 0, 1, 2, 3, … This expression using the symmetric gauge for quantized energy levels was first derived by Lev Landau, and hence these energy levels are known as *Landau levels* (LL).[37] With increasing magnetic field, more electrons collapse into each LL, since $\omega_c = \frac{eB}{m}$. The allowed values of k_y tells us the about the degeneracy of each LL.

Using a periodic boundary condition, each k_y value takes a space of $\frac{2\pi}{L_y}$ and the number of states in each LL n_L per unit area is:

$$n_L = \frac{m\omega_c}{\hbar} L_x \left(\frac{2\pi}{L_y}\right)^{-1} = \frac{eB}{h} \quad , \tag{2.14}$$

A filling factor ν is introduced.

$$\nu = \frac{n_e}{n_L} = \frac{hn_e}{eB} \tag{2.15}$$

doi:10.6342/NTU202210171

where n_e is the electron density. When $\nu = i$, where i is any integer, means that the lowest i LL are fully filled, while the ones above are empty. The filling factor depends only on the magnetic field and the electron density, which means we can modify it experimentally in two ways.

Considering the density of states, if the magnetic field is changed while the energy is fixed at the Fermi energy, the density of states condense into delta peaks which appear periodically in *1/B*. Scattering has been ignored for the Landau level derivation. In non-ideal conditions, however, the density of states ceases to be perfect delta peaks and instead broaden in the presence of impurities and defects, as shown in Figure 2.4.

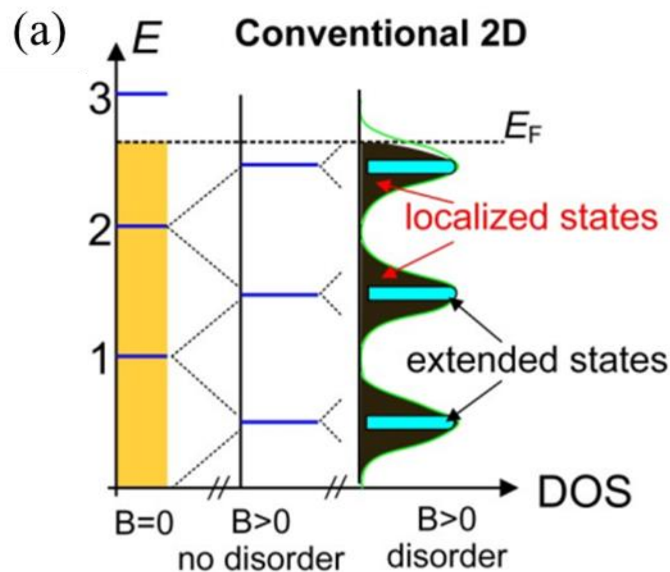

Figure 2.4: Formation of LL in 2D density of states. *The orange highlighted region shows a typical continuum of states at zero magnetic field. In the presence of a magnetic field and disorder (scattering), these collapse into quantized delta functions, in theory. However, in practical systems, there is a broadening of LL as shown above. The localized states do not participate in the conduction process, but the extended states do. The LL spacing is proportional to the magnetic field.*

2.2.2 Landauer-Büttiker formalism

doi:10.6342/NTU202210171

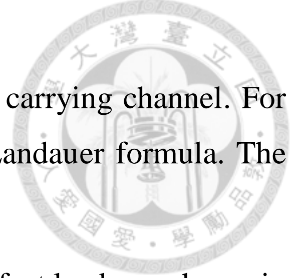

The Landauer-Büttiker formalism can be used to picture a current carrying channel. For simplicity, we start with a two terminal system to derive the important Landauer formula. The derivations in the following sections are heavily inspired from [39].

Consider a mesoscopic region with two reservoirs connected by perfect leads, as shown in Figure 2.5. The transport here is phase-coherent since the inelastic scattering length in the mesoscopic regime is longer than the size of the sample. Electrons coming from reservoir one moving to the second reservoir, equilibrate at its chemical potential and temperature as they reach. According to Büttiker's nomenclature, if all electrons leaving the mesoscopic region (MSR) enter the reservoir, they are denoted as reflectionless. In Figure 2.6, the leads are parallel to the x-axis. The electrons are confined to an area *A* in the y-z plane which has impenetrable walls at the boundary. We can then treat it as a 2D particle-in-a-box problem in the y-z plane.

Such a problem has a solution of plane waves X_n with discreet energies, ε_n. For the leads, the Hamiltonian and the eigenstates read as:

$$H = \frac{p_x^2}{2m} + \frac{p_\perp^2}{2m}, \qquad \boldsymbol{r}_\perp \in \boldsymbol{A} \tag{2.16}$$

$$\varphi_{\alpha n \mathrm{E}}^{\pm}(x, \boldsymbol{r}_\perp) = \sqrt{\frac{m}{2\pi\hbar^2}} \frac{1}{\sqrt{k_n(E)}} X_n(\boldsymbol{r}_\perp) e^{\pm i k_n(E) x}, \qquad (x, \boldsymbol{r}_\perp) \in \alpha \tag{2.17}$$

Here, for the plus sign, states move to the right and vice versa for opposite sign, with wavenumber $k_n(E) = \frac{\sqrt{2m(E-\varepsilon_n)}}{\hbar}$. Each eigenstate can carry a current, and hence *n* becomes the channel index. If an eigenstate is never occupied by a carrier for a sufficiently large $n > M$, then we can say that there are M_α channels for the lead α.

doi:10.6342/NTU202210171

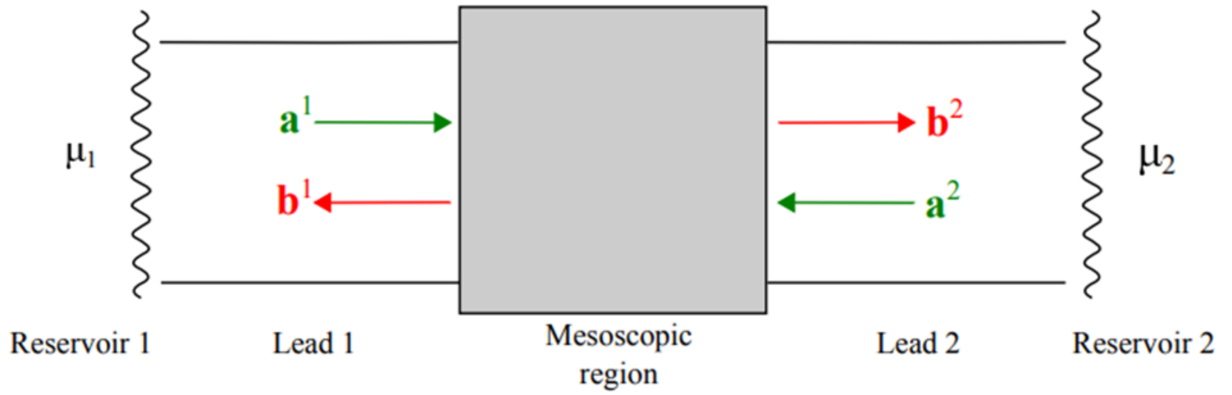

Figure 2.5: Two-terminal phase coherent conductance. *Two reflectionless reservoirs at chemical potential μ_1 and μ_2 are connected by perfect leads to a mesoscopic region.*

The eigenstates carry the same current due to normalization. An eigenstate has the unit of current per energy, when inserted into the current operator, however, the current unit appears when summing over contributions from more eigenstates. With the normalization, a sum over k for eigenstates $\varphi_k = {e^{ikx}}/{\sqrt{L}}$ can be written as $\sum_k \langle \varphi_k | A | \varphi_k \rangle \rightarrow \frac{L}{2\pi} \int_0^\infty dk \langle \varphi_k | A | \varphi_k \rangle$. In this normalization, the sum becomes:

$$\sum_k \langle \varphi_{\alpha n E} | A | \varphi_{\alpha n E} \rangle \rightarrow \frac{1}{2\pi} \frac{2\pi\hbar^2}{m} \int_0^\infty dk \langle \varphi_{\alpha n E} | A | \varphi_{\alpha n E} \rangle \tag{2.18}$$

$$= \frac{\hbar^2}{m} \int_0^\infty dE \frac{k}{dE/dk} \langle \varphi_{\alpha n E} | A | \varphi_{\alpha n E} \rangle \tag{2.19}$$

$$= \int_0^\infty dE \langle \varphi_{\alpha n E} | A | \varphi_{\alpha n E} \rangle \tag{2.20}$$

This is later used to derive the Landauer formula. A superposition of eigenstates can be used to write the wavefunction in lead α. With coefficients, a_n^α and b_n^α used to denote the incoming and outgoing waves, respectively, and n denotes the channel. At energy E,

doi:10.6342/NTU202210171

$$\psi_E(x,\boldsymbol{r}_\perp) = \begin{cases} \sum_n a_n^1 \varphi_{1nE}^{+}(x,\boldsymbol{r}_\perp) + b_n^1 \varphi_{1nE}^{-}(x,\boldsymbol{r}_\perp)\ , & (x,\boldsymbol{r}_\perp) \in Lead\ 1, \\ \quad \psi_{MSR,E}(x,\boldsymbol{r}_\perp)\ , & (x,\boldsymbol{r}_\perp) \in MSR \\ \sum_n a_n^2 \varphi_{2nE}^{+}(x,\boldsymbol{r}_\perp) + b_n^2 \varphi_{2nE}^{-}(x,\boldsymbol{r}_\perp)\ , & (x,\boldsymbol{r}_\perp) \in Lead\ 2, \end{cases} \tag{2.21}$$

Here, the mesoscopic region is denoted by MSR. The current through the MSR equals the current through the leads, meaning that it is not required to know the wavefuntion $\psi_{MSR,E}(x,\boldsymbol{r}_\perp)$ to determine the conductance. Instead, we can use the Scattering-matrix to relate the amplitudes of reflection and transmission in the region to the coefficients of the incoming and outgoing waves. This can be done as follows:

$$\begin{pmatrix} b_1^1 \\ b_2^1 \\ b_1^2 \\ b_2^2 \end{pmatrix} = \begin{pmatrix} r_{11} & r_{12} & t'_{11} & t'_{12} \\ r_{21} & r_{22} & t'_{21} & t'_{22} \\ t_{11} & t_{12} & r'_{11} & r'_{21} \\ t_{21} & t_{22} & r'_{21} & r'_{22} \end{pmatrix} \begin{pmatrix} a_1^1 \\ a_2^1 \\ a_1^2 \\ a_2^2 \end{pmatrix} \tag{2.22}$$

For a general case with M- channels, the coefficients can be written as vectors, and the S-matrix can be separated into 4 MxM submatrices, 2 each for reflection and transmission.

$$\boldsymbol{c}_{out} = \begin{pmatrix} \boldsymbol{b^1} \\ \boldsymbol{b^2} \end{pmatrix} = \begin{pmatrix} r & t' \\ t & r' \end{pmatrix} \begin{pmatrix} a^1 \\ a^2 \end{pmatrix} = \boldsymbol{S}\boldsymbol{c}_{in} \tag{2.23}$$

We can define new states known as the scattering states using this formalism. In such cases, the outgoing coefficients are found from the S-matrix, and the incoming co-efficient is set to 1.

2.2.3 The Landauer formula

A wavefuntion $\Psi(x,\boldsymbol{r}_\perp)$ carrying an electric current through a cross-section A can be calculated using the following equation:

doi:10.6342/NTU202210171

$$I = -\frac{e\hbar}{2mi}\int_A d\boldsymbol{r}_\perp\left[\Psi^*(x,\boldsymbol{r}_\perp)\left(\boldsymbol{\partial_x}\Psi(x,\boldsymbol{r}_\perp)\right) - \left(\boldsymbol{\partial_x}\Psi^*(x,\boldsymbol{r}_\perp)\right)\Psi(x,\boldsymbol{r}_\perp)\right] \quad (2.24)$$

The continuity equation can be used to derive this equation. By inserting a scattering state, one can determine the electric current per energy that this state carries. For a channel n in lead 1, the incoming state, we can say that:

$$I_{1nE} = -\frac{e\hbar}{2mi}\int_A d\boldsymbol{r}_\perp\left[\psi^*_{1nE}(\partial_x\psi_{1nE}) - (\partial_x\psi^*_{1nE})\psi_{1nE}\right] \quad (2.25)$$

$$= -\frac{e}{2ih}\int_A d\boldsymbol{r}_\perp\,[(\frac{1}{\sqrt{k_n}}X_n^* e^{-ik_nx} + \sum_{n'} r^*_{nn'}\frac{1}{\sqrt{k_{n'}}}X^*_{n'}e^{ik_{n'}x}) \times (i\sqrt{k_n}X_n e^{-ik_nx}$$

$$- i\sum_{n''} r_{nn''}\sqrt{k_{n''}}X_{n''}e^{-ik_{n''}x}) - (-i\sqrt{k_n}X_n^* e^{-ik_nx}$$

$$+ i\sum_{n'''} r^*_{nn'''}\sqrt{k_{n'''}}X^*_{n'''}e^{ik_{n'''}x}) \times (\frac{1}{\sqrt{k_n}}X_n e^{ik_nx}$$

$$+ i\sum_{n''''} r_{nn''''}\frac{1}{\sqrt{k_{n''''}}}X_{n''''}e^{-ik_{n''''}x})\,]$$

$$= -\frac{e}{2h}\left[1 - \sum_{n''}\delta_{nn''}r_{nn''}\frac{\sqrt{k_{n''}}}{\sqrt{k_n}}e^{-ik_nx}e^{-ik_{n''}x} + r^*_{nn}\,e^{2ik_nx}\right.$$

$$\left. - \sum_{n'} r^*_{nn'}\,r_{nn'} + 1 + r_{nn}e^{-2ik_nx} - r^*_{nn}e^{2ik_nx} - \sum_{n'''} r^*_{nn'''}r_{nn'''}\right]$$

$$= -\frac{e}{h}\left[1 - R_n^{11}\right] \quad (2.26)$$

$$= -\frac{e}{h}T_n^{21} \quad , \quad (2.27)$$

where we simplify the notation by suppressing the energy dependency of k_n. The total probability that a wavefunction coming into a channel n is reflected to another channel n' the same lead, is denoted as $R_n^{\alpha\alpha} = |\sum_{n'} r_{nn'}|^2$. The amount that is not reflected, has to be transmitted, and that is given by T_n^{21}.

Similarly, we can derive the current per energy for the scattering states coming from lead 2 as:

doi:10.6342/NTU202210171

$$I_{2nE} = \frac{e}{h} T_n^{12} \quad , \tag{2.28}$$

By adding up all the current contributions coming from all the channels, and then integrating them over the energy, we can find the total current. To find the total electric current, we must multiply each current contribution by the Fermi-Dirac distribution function for the incoming lead, to get:

$$I = -\frac{e}{h} \sum_n \int_0^\infty dE [T_n^{21} f(E - \mu_1) - T_n^{12} f(E - \mu_2)]$$

$$= -\frac{e}{h} \sum_n \int_0^\infty dE \ \mathrm{Tr}[t^+ t][f(E - \mu + eV_1) - f(E - \mu + eV_2)] \tag{2.29}$$

The above equation is derived using the unitarity condition of the S-matrix. At low temperatures, the Fermi-Dirac distribution becomes a step function. The derivative of a distribution function is therefore a negative Dirac delta function.

$$I = -\frac{e}{h} \sum_n \int_0^\infty dE \ \mathrm{Tr}[t^+ t] \left.\frac{\partial \mathrm{f}}{\partial \mathrm{E}}\right|_\mu (eV_1 - eV_2) \tag{2.30}$$

$$\xRightarrow{T \to 0} \frac{e^2}{h} \mathrm{Tr}[t^+ t](V_1 - V_2) \tag{2.31}$$

So far, we have suppressed the dependence of the transmission matrices on energy. But at sufficiently low temperatures, we can safely assume that they are constant in energy, which validates our integration above. The conductance, $G = I/(V_1 - V_2)$ gives us:

$$G = \frac{e^2}{h} \mathrm{Tr}[t^+ t] = \frac{e^2}{h} \sum_n T_n^{21} \tag{2.32}$$

which is known as the Landauer formula. A peculiar property of this derivation is that it mathematically proves that a perfect channel adds $\frac{e^2}{h}$ to the value of the conductance. We are one step closer to understanding the transport in the quantum Hall regime. We now need to derive the Landauer-Buttiker formula for multiprobe systems.

doi:10.6342/NTU202210171

2.2.4 The Landauer formula for multiprobe systems

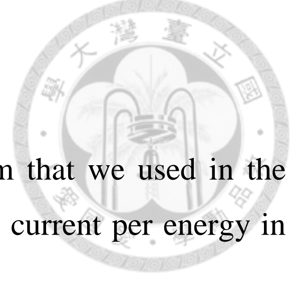

The derivation in this case is quite similar to a two probe system that we used in the previous section. However, here $\beta \neq \alpha$, hence the scattering states carry a current per energy in lead α as shown:

$$I^{\alpha}_{\alpha nE} = -\frac{e}{h}\sum_{\beta\neq\alpha} T^{\beta\alpha}_{n}, \qquad I^{\alpha}_{\beta nE} = \frac{e}{h}T^{\beta\alpha}_{n} \quad , \tag{2.33}$$

Same as earlier, we find the lead α's total current by adding the current contribution and multiply them with the distribution functions of the incoming reservoirs.

$$I^{\alpha} = \sum_{\beta n}\int_0^{\infty} dE\, I^{\alpha}_{\beta nE} f\left(E-\mu+eV_{\beta}\right) \tag{2.34}$$

$$= -\frac{e}{h}\sum_{\beta\neq\alpha,n}\int_0^{\infty} dE[T^{\beta\alpha}_{n} f(E-\mu+eV_{\alpha}) - T^{\alpha\beta}_{n} f(E-\mu+eV_{\alpha})$$

$$\overset{T\to 0}{\Longrightarrow} \frac{e^2}{h}\sum_{\beta\neq\alpha}(T^{\beta\alpha}V_{\alpha} - T^{\alpha\beta}V_{\beta}) \quad , \tag{2.35}$$

where $T^{\alpha\beta} = \sum_n T^{\alpha\beta}_{n}$ is the total transmission probability from lead $\beta\ to\ \alpha$. The total transmission probability is not always similar for contact $\alpha\ to\ \beta$ as it is from $\beta\ to\ \alpha$ for a multiprobe system. If lead α has M_{α} number of channels, and $R^{\alpha\alpha} = \sum_n^M R^{\alpha\alpha}_{n}$ is the total probability for reflection of the incoming waves, then because of the conservation of current, and the fact that there is no voltage difference between contacts, means that no current flows. We can then conclude that:

$$(M_{\alpha} - R^{\alpha\alpha}) - \sum_{\beta\neq\alpha} T^{\beta\alpha} = 0 \quad , \quad (M_{\alpha} - R^{\alpha\alpha}) - \sum_{\beta\neq\alpha} T^{\alpha\beta} = 0 \quad , \tag{2.36}$$

We now have an understanding of the tools we shall use to understand mathematically the integer quantum Hall effect.

doi:10.6342/NTU202210171

2.3 Quantum Hall Effect

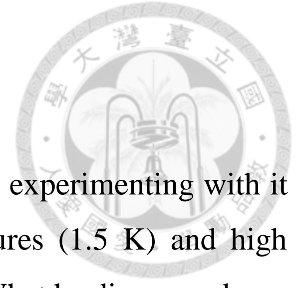

Pushing the limits of the Hall effect, Prof. Klaus von Klitzing was experimenting with it on a Si metal oxide field effect transistor (MOSFET) at low temperatures (1.5 K) and high magnetic field (>19 T). The Si-MOSFET served as a 2DEG under study. What he discovered was so groundbreaking that he was awarded the Nobel Prize in Physics in 1985. He found that the Hall resistance is not linear at those conditions, but instead, exhibits a series of plateaus at around 25.8 kΩ, 12.9 kΩ, 6.4 kΩ, and so on, as shown in Fig. 2.3. While the Hall resistance is at a plateau, the longitudinal resistance shows another peculiar behavior of being exactly zero! He also found that this behaviour was independent of the sample dimensions and type, as long as it was a 2DEG. At the moment of its discovery, it was published as a method to exactly determine the fine structure constant [40], which is defined as:

$$\alpha = \frac{e^2}{2\varepsilon_0 hc}$$

where h is the Planck's constant = 6.626 x 10^{-34} J.s, c is the speed of light in vacuum, and ε_0 is the permittivity of free space, respectively. To understand how this correlated to the Hall resistance, we will now use the tools derived in the earlier sections.

Consider six reservoirs connected in an ideal manner as shown in Figure 2.7. Such a geometric arrangement is known as a 'Hall bar', wherein the leftmost and the rightmost contacts serve as the source and drain contacts. Consider N available edge states. In order to avoid confusion with the direction of the current, let us assume holes are the carriers here. The holes coming in from the source, equilibrated at voltage V_1, follow the upper edge and get absorbed into contact 2. The current form reservoir 1 going into a perfect channel is $\frac{e^2}{h}V_1$, the current into the N edge states will then be, $\frac{e^2}{h}NV_1$. Now using the multiprobe Landauer formalism, we can deduce that $T^{\beta 1} = 0$ for $\beta \neq 2$ and $T^{21} = N$. In matrix form, we can arrive at:

doi:10.6342/NTU202210171

$$
\begin{pmatrix} I^1 \\ I^2 \\ I^3 \\ I^4 \\ I^5 \\ I^6 \end{pmatrix} = \frac{e^2}{h} \begin{pmatrix} N & 0 & 0 & 0 & 0 & -N \\ -N & N & 0 & 0 & 0 & 0 \\ 0 & -N & N & 0 & 0 & 0 \\ 0 & 0 & -N & N & 0 & 0 \\ 0 & 0 & 0 & -N & N & 0 \\ 0 & 0 & 0 & 0 & -N & N \end{pmatrix} \begin{pmatrix} V_1 \\ V_2 \\ V_3 \\ V_4 \\ V_5 \\ V_6 \end{pmatrix} \tag{2.37}
$$

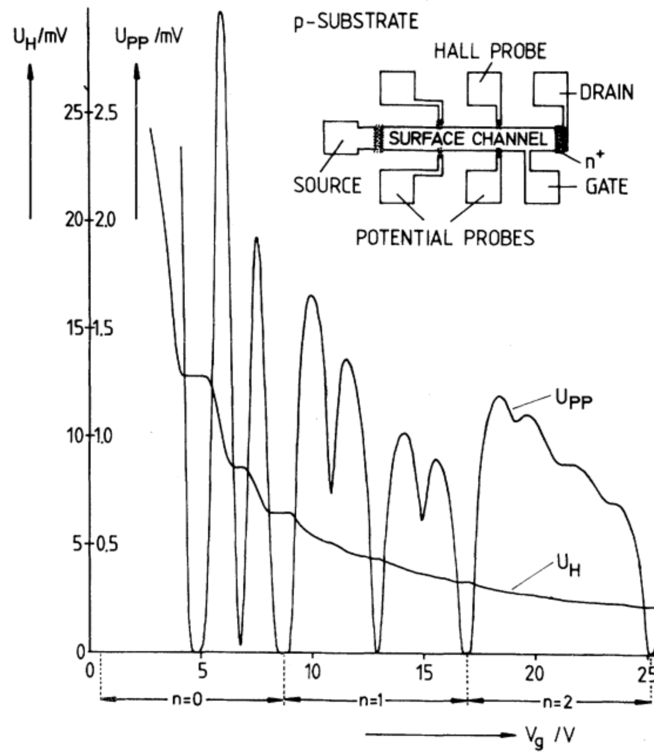

***Figure 2.6: The first quantum Hall data**. Von Klitzing's plot of the Hall Voltage U_H and the longitudinal voltage U_{pp} as a function of the gate voltage Vg at T = 1.5K at I = 1 μA and a constant magnetic field of B = 18T. Adapted from[40]*

doi:10.6342/NTU202210171

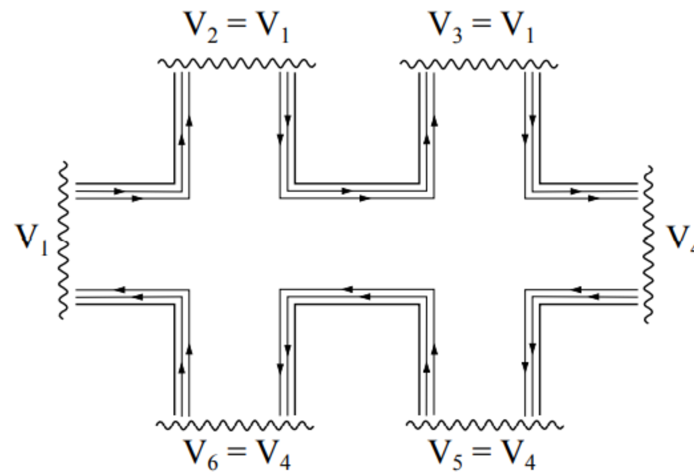

__Figure 2.7: A Hall Bar with idea contacts.__ 6 reservoirs connected ideally. No net current flows in any contacts other than the Source and the Drain. The direction of the current is indicated by the arrows. Adapted from[41]

The total current is $I = I^1 = -I^4 = (\frac{e^2}{h})N(V_1 - V_4)$. As contacts 1 and 4 are source and drain, it there is no current carried by other contacts. Which leads to $V_1 = V_2 = V_3$ and $V_4 = V_5 = V_6$, from the matrix. This implies there is no potential drop between these contacts, or in other words, the longitudinal resistance is zero!

$$R_L = R_{14,65} = \frac{V_6 - V_5}{I} = 0 \tag{2.38}$$

Here, the first two indices, 14, denote the current flow and the last two indices, 65, indicate where the voltage is measured. Then the Hall resistance is given by:

$$R_H = R_{14,26} = \frac{V_2 - V_6}{I} = \frac{h}{e^2}\frac{1}{N} \tag{2.39}$$

This groundbreaking result is that the longitudinal resistance becomes zero while the Hall resistance is quantized at integer filling factors, is known as the Integer quantum Hall effect.

There is no limit on how big the Hall bar can be for which the quantum Hall effect can be observed. However, if we make it too small, certain deviations can occur. Disordered contacts and phase coherence can breaks the effect for small samples. Electrons can travel from one edge to the other if the are placed too close to each other. Impurities localize the bulk states and hence play a

doi:10.6342/NTU202210171

crucial role. Due to this, the current in a large range of magnetic fields, only flows along the edges. The plateaus would be shorter for super clean samples, while, too many impurities can cause the wavefunctions to overlap, so that electrons can cross the Hall bar. Such considerations can be complicated, as it depends on both, the impurity locations and density, and on the electrostatic potential changes due to the impurity.

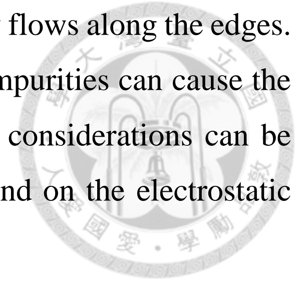

2.4 Integer quantum Hall effect in EG

The observation of an unconventional integer quantum Hall effect in graphene, soon after its discovery was a strong piece of evidence of the Dirac nature of its carriers. It was unconventional in the sense that its filling factors were

$$\nu = \pm 4\left(n + \frac{1}{2}\right), n = 0, 1, 2, \dots$$

The Hall plateau displayed a four-fold degeneracy. We can understand this by looking at the LL of graphene. There are three significant differences in the LL of graphene from conventional 2D systems. First, the energy spacing scales linearly in conventional 2D systems while here, it scales as $\Delta E \propto \sqrt{B}$. The valley degeneracy (recall K and K' from earlier sections on graphene) increases the degeneracy of each LL by an added factor of two. Lastly, a LL exists at zero energy which is shared by two valleys and is thus, only spin-degenerate. All these severely affect the Hall plateaus for graphene. The number of electrons required to fill a LL is $\frac{eB}{h}$, for a conventional 2D system. So including the spin and valley degeneracy, for N completely filled LL, above zero, the charge carrier density for graphene would be:

$$n = 4\frac{eB}{h}\left(N + \frac{1}{2}\right)$$

Hence, we see that,

doi:10.6342/NTU202210171

$$R_{xy} = \frac{B}{en} = \frac{h}{4e^2\left(N+\frac{1}{2}\right)} \tag{2.40}$$

We now understand why the resistances quantized exactly around 26 kΩ, 12.9 kΩ, 6.4 kΩ, and so on. The unique LL spacing in graphene has had a huge impact in technological applications. Due to the large spacing between the first LL and the zeroth LL in graphene, the $\nu = 2$ plateau can be observed at much lower magnetic fields (or higher temperatures). The precisely quantized values have since been made the standard for the SI unit of resistance, Ohm, epitaxial graphene being at the forefront of it.

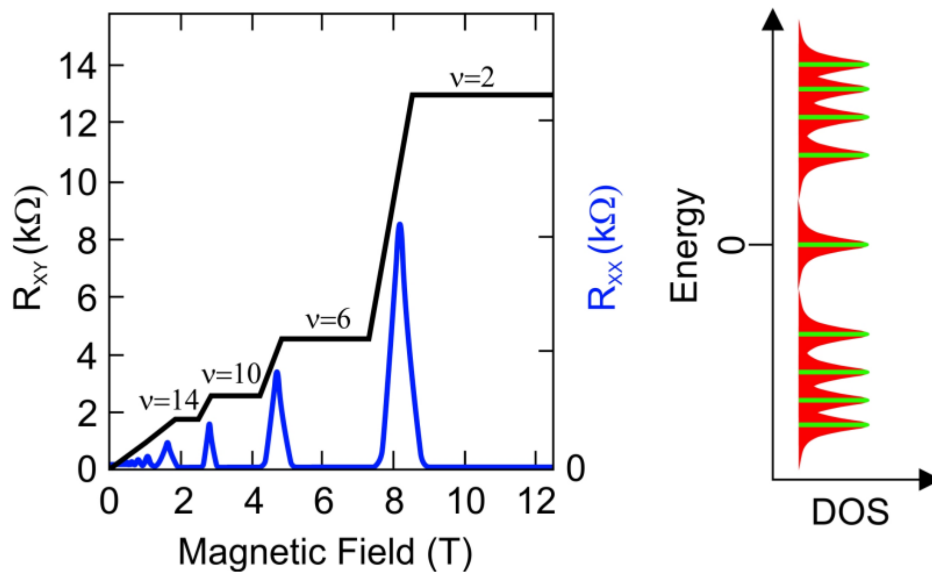

Figure 2.8: Quantum Hall effect and the density of states in Graphene. *Right: The Hall and longitudinal resistance verses the magnetic field for graphene. Left: LL spectrum for graphene. Adapted from [42]*

2.5 Edge States

Edge state picture is a common way to describe the transport in the QHE. Every real sample is confined by its edges. Landau levels bend in an upward irections for a confining potential. Edge states carry the current at the boundary of the sample. It doesn't matter where the Fermi level is located, it will cross the extended states at the boundary. These edge states are pictured as skipping orbits in a classical picture, with a radius l_B. The magnetic field here, suppresses backscattering[43].

doi:10.6342/NTU202210171

Using ideas from our derivations of the Landauer-Buttiker formalism, each edge states carrys a current of $I = \frac{e}{h}\Delta\mu$ and forms a one-dimensional channel, where $\Delta\mu = \mu_2 - \mu_1$ gives the difference of the electro chemical potential of the two current leads. We treat every channel with a corresponding transmission coefficient T and each contact with a reflection coefficient R. For ballistic channels and perfect contacts $R = T = 1$. M of those edge channels are thus carrying a current of $I = M\frac{e}{h}\Delta\mu$. The carries in the opposite edges are moving in the opposite direction due to the band bending and have the chemical potential of their originating current lead, as shown in Figure 2.9.

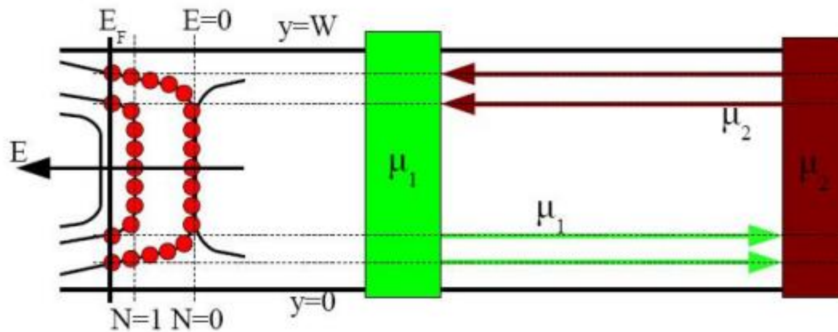

Figure 2.9: Edge states in graphene. *TDue to the confinement of the sample width W, the quantized energy levels, or Landau levels bend up. The dots in red signify all occupied states upto the Fermi level. The filled valence band states do not contribute to the current and are hence not shown here. At the edge, the Landau level is lifted and splits into two levels due to the valley degeneracy of the N=0 Landau level being lifted. Both states are double spin degenerated, and bend towards positive and negative energies. The N = 0 level is still fourfold degenerated (spin and valley). In this picture, we see a* $v = 2$ *filling factor with 6 ballistic edge channels at each side with chemical potential of* μ_1 *or* μ_2*. The transverse resistance is then given by* $R_H = R_K/6$*.*

With these ideas we can arrive at the same conclusion for the quantum Hall effect in graphene:

$$R_H = \frac{\frac{\Delta\mu}{E}}{M\Delta\mu\frac{e}{h}} = \frac{h}{Me^2} = \frac{R_K}{M} \quad , \tag{2.41}$$

For graphene, M = 2, 6, 10,…is given by the number of occupied LL. Every time the Fermi level is shifted through a higher LL, an additional channel is added to the system. Since the resistance

doi:10.6342/NTU202210171

will be lowest, when the Fermi level lies in between two levels, but highest, when it reaches a new Landau level, one can observe the Shubnikov-de Haas effect [44].

2.6 Hot Spots

In a study published in 1991, Klaß, and Dietsche imaged the spatial heat distribution of heat dissipation in the quantum Hall regime [45]. For this purpose, they utilized the fountain pressure effect of superfluid helium. They found that dissipation takes place at opposite corners at the current corners and is asymmetric after a critical current is reached, at integer filling factors (Figure 2.10). At non-integer filling factors, there is additional dissipation in the interior of the samples. This striking phenomenon has influenced modern metrology. The idea that the current has a point of entry and exit at the opposite corners was effectively used to obtain low noise measurements for QHRS at NIST [46](Figure 2.11).

Employing a split contact design as shown in Figure 2.11, they were able to perform quantum Hall measurements using just two terminals. The current injection through these hotspots in the quantum Hall regime, allowed for voltage and resistance measurements, irrespective of the contact resistances. This has allowed for smaller quantum Hall devices, which inturn allowed scaling to different resistance values. In chapter 5, these concepts are used to push the limits to how close such contacts can be placed and to study if that affects the distribution of the current in the quantum Hall regime.

The term hot spot (HS) in reference to the QHR applies to a region near any current-carrying contact where the local longitudinal resistance increases due to the power dissipation (Joule heating). Almost all Joule heating occurs where current enters the two-dimensional (2D) layer at one corner of the contact interface [47-51]. When this dissipation occurs only at the contacts it affects the two-terminal resistance and for metrological devices the contacts at each end of the device are typically well-separated. In our devices where multiple-series connections are present, the heating at a current-carrying side contact can be observed by measuring the increase in local resistance as current is increased and influences on nearby contacts may be observed

doi:10.6342/NTU202210171

electrically. Investigation of HS effects will enable understanding current flow and may lead to improved design architecture in QHR arrays by reducing the dimensions of devices.

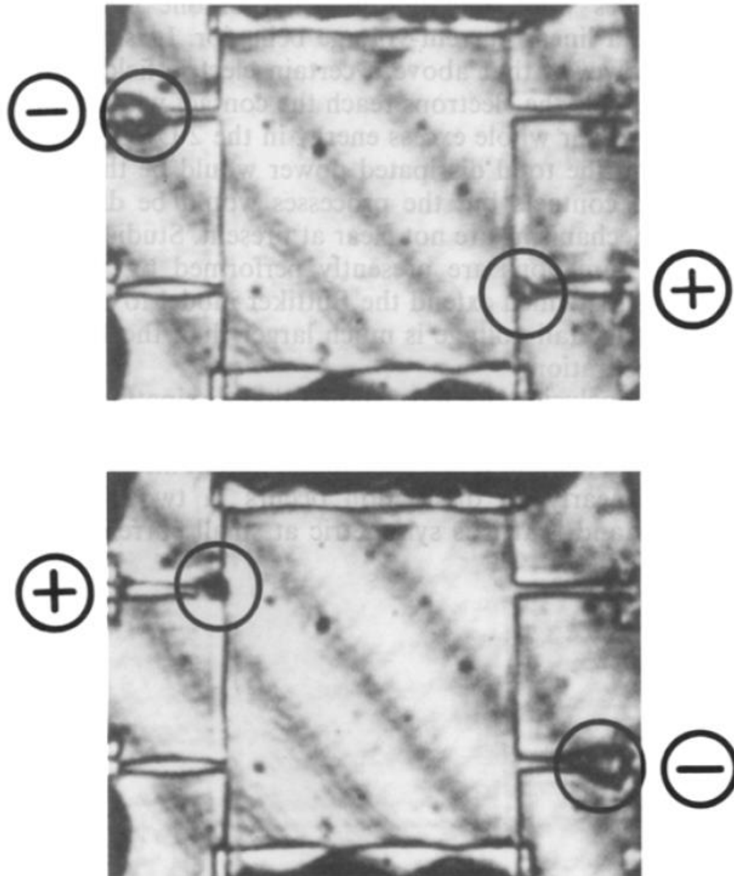

Figure 2.10: Hot spots in QHE. *In order to visualize the formation of hotspots, the voltage probes at the upper left and at the lower right have current fed through them. The above two photographs show two different current directions with respective polarities for the contacts marked. When electrons flow from a wide area into narrow leads, we can see the new drops in the circles. The optical interferences caused the broad fringes to appear in the photographs. Adapted from [45]*

doi:10.6342/NTU202210171

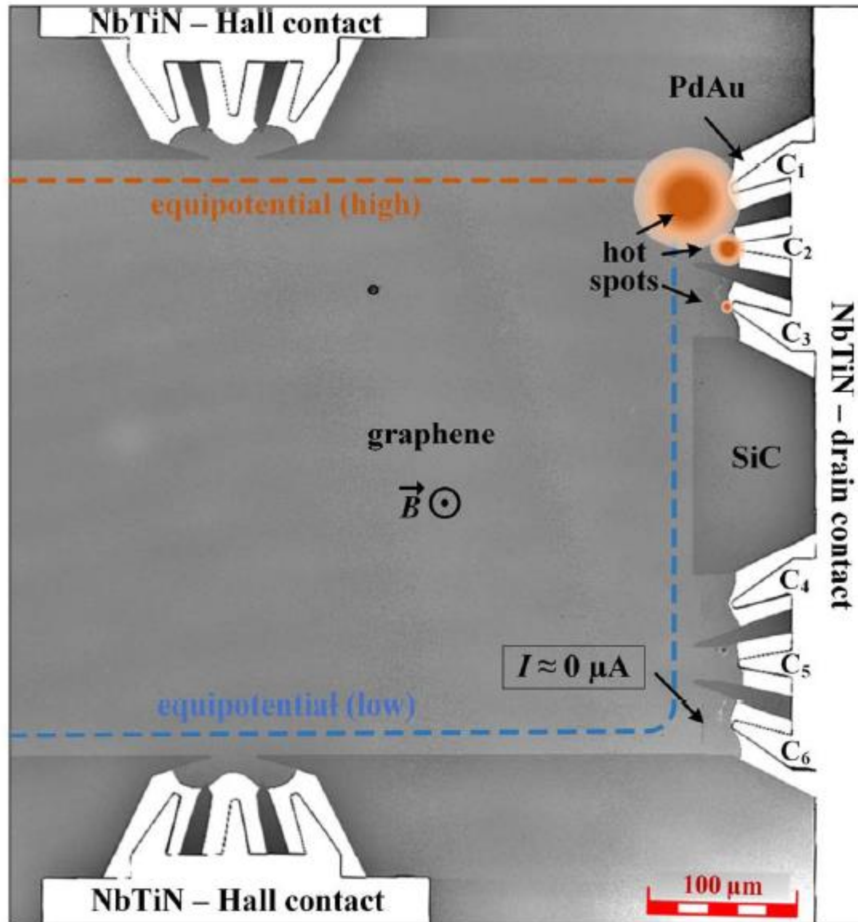

Figure 2.11: Application of Hot spots. *Confocal image of a graphene Hall bar device shows the drain contact (right) and two Hall contacts (top and bottom) and the graphene can be seen in contrast. The split contact design which branches the main contact into multiple parallel fingers makes the contact resistance in the quantum Hall regime negligible. The red spots indicate the region where most of the current enters the drain contact at the C1 branch, all the proceeding contact fingers have their current reduced by a factor of 2 each time. Hence, the current in the last branch is essentially 0 µA. This zero current describes the equilibrim between the QHE edge channels and the electric potential of the contacts. Adapted from [46]*

2.7 DC Equivalent circuits

Looking at a macroscopic picture, simplifying a quantum Hall system can be described in terms of circuit elements. One such attempt was made by Jeffery, Elmquist, and Cage, at NIST in

doi:10.6342/NTU202210171

1995 [48]. They used the double and triple series techniques from Delahaye [47] in order to come up with these precision tests. Taking into account every possible source of resistance in a circuit, the NIST group reduced a quantum Hall system to an equivalent circuit shown in Figure 2.12 below,

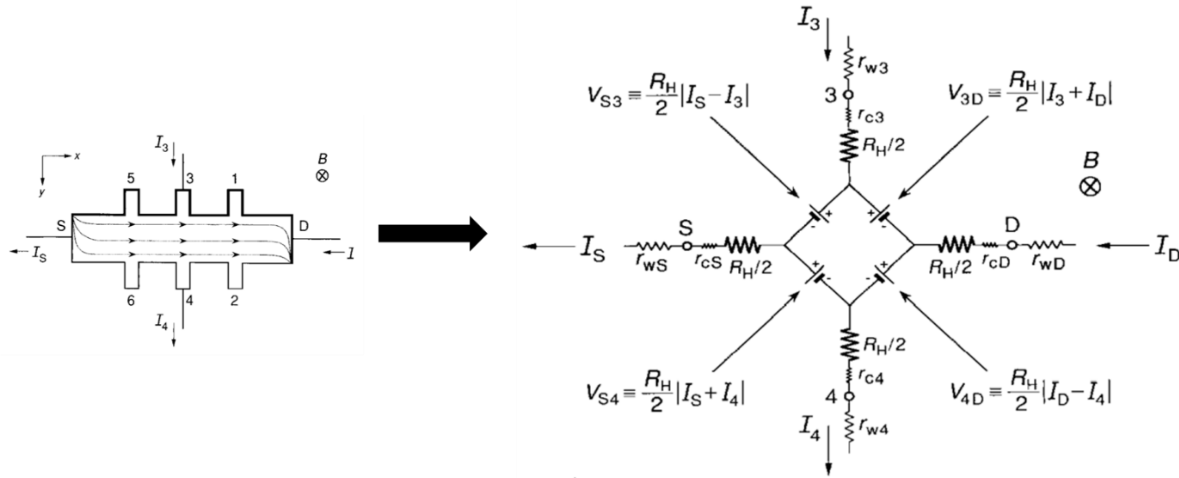

Figure 2.12: The DC equivalent circuit. *Left – Top view of a quantum Hall device showing the magnetic field and the direction of current flow. Right –The DC Equivalent circuit for the quantum Hall device on the left, showing a source and a drain and external leads going to the potential contacts 3 and 4.. The polarities of the voltages are shown along with the direction of the magnetic field. The positions of the contact resistances* r_c*, probe positions, intrinsic resistances* $R_H/2$*, lead resistances* r_w *are shown.*

2.7.1 Double series connections

According to their model, the total resistance in each arm, A, of the circuit can be split into its intrinsic resistance component s$R_H/2$ (R_H = 25 812.807 Ω) and the component r_A, defined as

$$r_A \equiv r_{cA} + r_{wA} + r_{test} + r_{CCC} \tag{2.42}$$

where, A represents S, D, 3 or 4, r_{cA} is the contact resistance, r_{wA} is the wire resistance, r_{test} is a resistor that can be added to test the circuit equations, and r_{CCC} is the resistance of a cryogenic current comparator (CCC) that can be placed in arm A to measure the current I_A. The circuit for a double series connection is shown in Figure 2.13.

doi:10.6342/NTU202210171

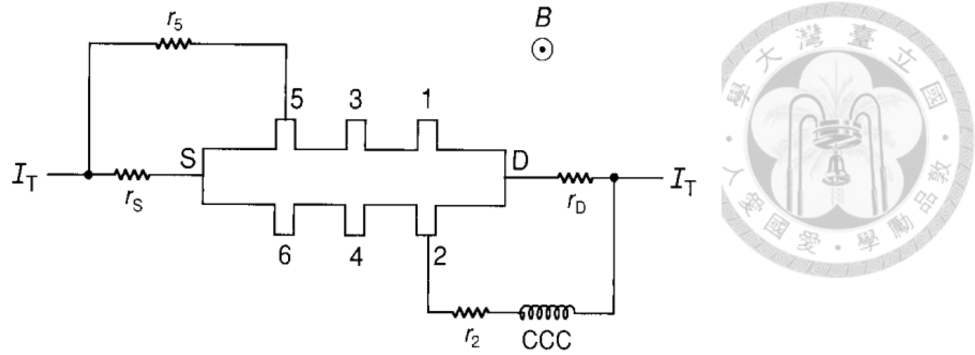

Figure 2.13: Double-series connection of a quantum Hall system. *Position of the CCC can be changed to measure any of the leads 2,4, and 6. Any ammeter can be used in place of a CCC for low accuracy measurements.*

By using basic Kirchoff's laws, one can obtain the following equations to determine the current in each arm:

$$I_3 = \frac{r_D}{(R_H + r_3)} I_D = \frac{r_D}{(R_H + r_D + r_3)} I_T \tag{2.43}$$

$$I_4 = \frac{r_S}{(R_H + r_4)} I_D = \frac{r_S}{(R_H + r_S + r_4)} I_T \tag{2.44}$$

where I_T is the total current flowing in and out of the system. This shows that I_3 and I_4 are small fractions of I_D and I_S and consequently, I_T.

doi:10.6342/NTU202210171

2.7.1 Triple series connections

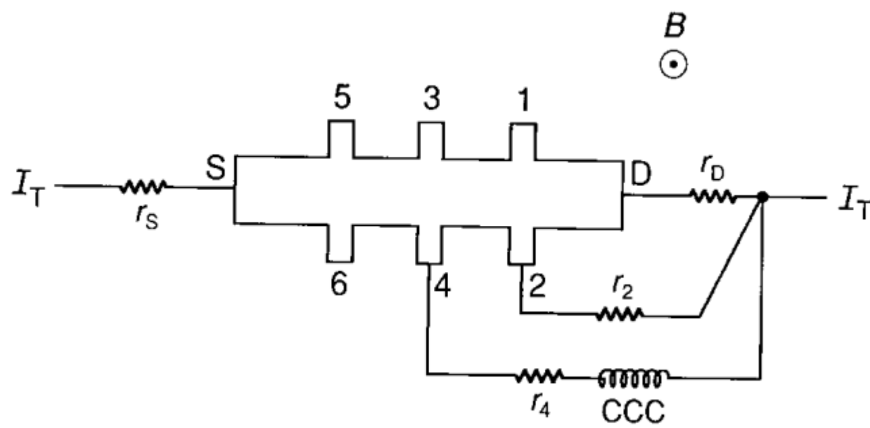

***Figure 2.14: Circuit for a triple series connection**. Here we can use a CCC to measure the current in either lead 4 or 6. We can also move the r_2 lead to 4 and measure the triple series current in lead 6.*

The equations for the circuit shown in the figure 2.14 above are as follows:

$$I_4 = \frac{r_S r_6}{[(R_H+r_S+r_6)(R_H+r_4)+r_S r_6]} I_T \tag{2.45}$$

$$I_6 = \frac{r_S}{(R_H+r_S+r_6)}(I_T - I_4) \tag{2.46}$$

Using these equations, we will test how the distribution of the current changes in contacts placed close to each other in the quantum Hall regime, in Chapter 5.

doi:10.6342/NTU202210171

Chapter 3 Experimental design and instrumentation

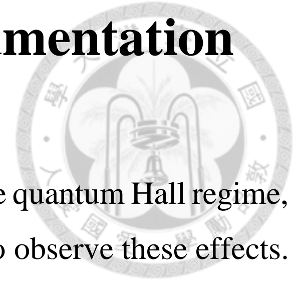

Now that we have the theoretical tools to understand the effects in the quantum Hall regime, we shall look at the experimental instrumentation and processes required to observe these effects. This chapter begins with a brief discussion on silicon carbide and leads up to graphene growth. A detailed process for graphene device fabrication is then discussed, followed by some basic electrical and magneto-characterization methods used in the core chapters of this thesis.

3.1 Silicon Carbide (SiC)

SiC is a wide-bandgap (2.3–3.3 eV) semiconductor [52] that is commonly used in high frequency, high temperature and high power device applications [53]. It is also used as a substrate for GaN-based LEDs [54]. SiC structure comprises of a covalently bonded tetrahedron with a four-fold symmetry. Closely packed double layers of Si and C atoms make up its crystalline structure. We can get many different stacking arrangements by varying the rotations and translations of this structure. The notable polytypes for SiC are:

- 2H – …ABAB..
- 4H-…ABCBABCB…
- 6H - …ABCACBABCACB…

4H and 6H are the most common polytypes. The EG grown and used in this thesis is on 4-H SiC. SiC has two faces, the Si-face (0001) and the C-face ($000\bar{1}$). The C-face is polycrystalline, allows a faster growth rate and the EG that grows on it is almost free standing, without coupling to the substrate. The Si-face on the other hand, is monocrystalline, has a slow growth rate which allows for a more controlled uniform growth and coverage. The graphene is also strongly coupled to the buffer layer, which is carbon rich and affects its transport properties [28, 55].

Depending on the face of the substrate under consideration, different morphologies and properties can be obtained. Modifications can be made to the process to achieve different results.

doi:10.6342/NTU202210171

For example, remove polishing damage on SiC, etching in hydrogen is commonly practiced in CVD reactions to and provide an atomically flat terrace and a well-defined surface EG growth[56].

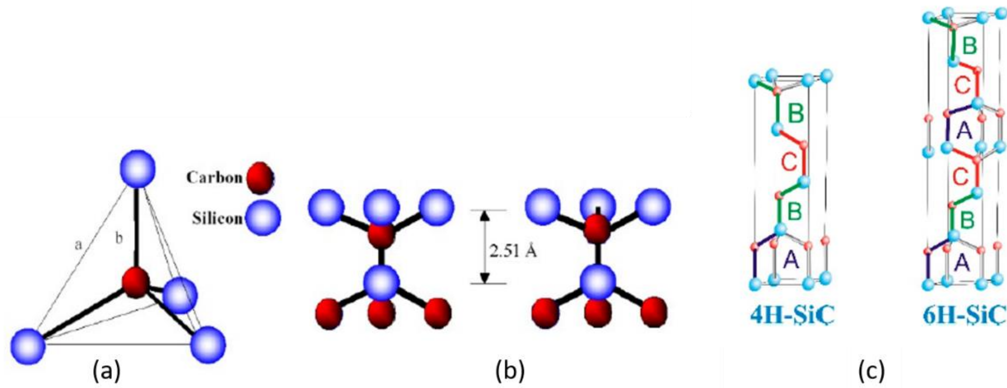

Figure 3.1: Structure of SiC. (a) Basic unit of a Silicon Carbide. The distance between C-C or Si-Si atoms, a, is about 3.08 Å. (b)The two configurations of carbon and silicon atoms rotated by 180º.(c) Stacking sequence of SiC polytypes. Adapted from[55].

3.1.1 Patterning a SiC substrate

It is important to identify different pieces of SiC on which graphene would be grown. Alignment marks to help identify and dice the wafer into smaller pieces, were etched into the C-face of the wafer. For this, the Si-face was first covered with a protective polymer AZ5214e, a positive photoresist. This layer ensured that the pre-polished Si-face of the wafer remained intact through the process of etching the C-face.

The C-face was then coated with S1813, another positive photoresist. We then exposed a pattern as shown in Figure 3.2 on the C-face of the wafer using a contact lithography mask on the SuSS MA-6 lithography tool. Note that this pattern is a mirror image, which is intentional as the idea is to be able to read the etching marks from the Si-face. This pattern was then developed using CD-26 developer for 60s. The development was done on an automated developing station which

doi:10.6342/NTU202210171

prevents the developer from touching the back of the wafer, thus keeping the protective polymer layer, intact.

Once developed, the pattern was ready to be etched into the SiC surface through the process of ion milling. The Denton 4-wave ion milling tool was used for this purpose. The recipe involved use of the highly reactive SF6 gas which under a large bias would ionize and attack the SiC surface, etching it. The surface was etched to a depth of at least 500 nm so that the marks will be visible from the other side. At the completion of the process, the photoresist polymer coating on both faces was dissolved by soaking the wafer in remover PG for one hour at 80C. After which the wafer is rinsed with IPA and dried by blowing it with N_2 gas. Before dicing this wafer, it is necessary to coat it with a protective polymer. Hence, the Si-face was again coated with AZ5214e.

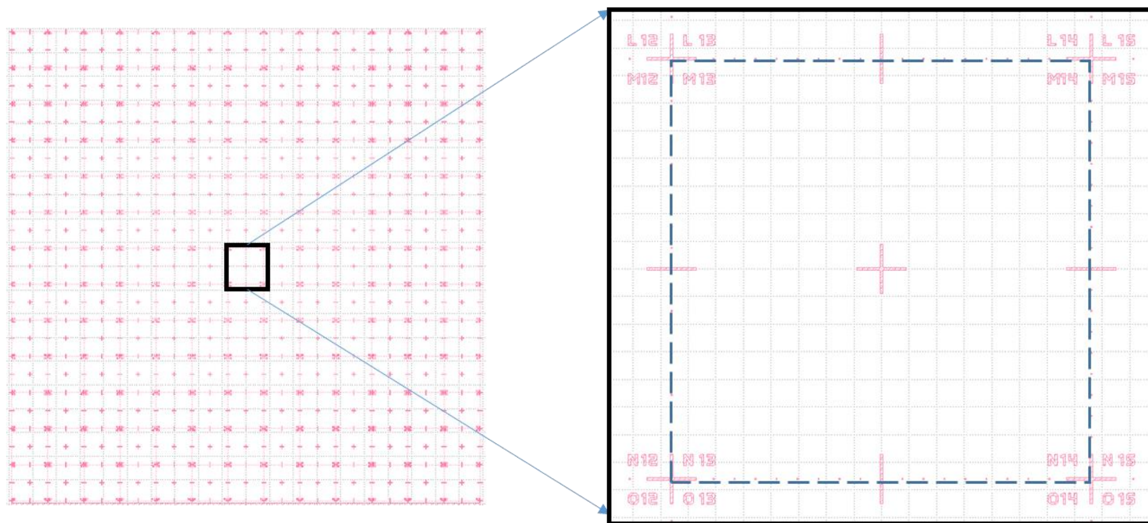

Figure 3.2: SiC alignment marks and dicing pattern. *Left: The pattern to be etched on the C-face of the SiC wafer. It is then diced along the dotted square marked in blue lines on the zoomed in image on the right.*

3.1.2 Dicing SiC

doi:10.6342/NTU202210171

SiC is a very hard material to cut into. A dicing saw with a special diamond blade has to be used. Thanks to the alignment marks, the wafer may be diced into 7.7 mm × 7.7 mm or 15.4 mm × 15.4 mm squares. We preferred 7.7 mm squares since graphene grows more consistently and uniformly on smaller pieces. Research is still ongoing to grow larger area EG. The figure on the right in figure 3.2 indicates the pattern to be diced. The dicing has to be performed in two passes so as to avoid damage to the blade. In the first pass, the wafer is diced about 30% of the way through, on the second pass, about 45% more is diced. The remaining 25% is enough to be physically broken after taking it off the tool. This also serves the purpose of being able to grow and process multiple small 7.7 mm × 7.7 mm pieces and then break them into individual pieces after the devices have been fabricated, saving time and processing cost. The dicing then leaves us with final chips with alphanumeric labelling on all 4 corners for easy identification.

3.1.3 Cleaning the pieces

Cleaning SiC pieces followed standard industrial cleaning procedures. The small chips were first cleaned in acetone using an ultrasonic bath cleaner. After which they were cleaned in IPA in the same ultrasonic bath. They were then dried with N_2 gas. The next step was to clean the chips using a piranha solution. The piranha solution is an industry standard and is a mixture of H_2SO_4 and H_2O_2 in a 3:1 ratio. The solution has to be carefully prepared in an acid hood by adding H_2O_2 to the sulfuric acid. It is a highly exothermic reaction, the solution heats upto a 100°C within seconds. Due to safety concerns while mixing the solution, users in the CNST nanofab have been advised to use a nanostrip solution. Nanostrip is a premixed but mild piranha solution. This solution needs to be heated on a hot plate to be effective at cleaning. The chips were soaked in this solution at 80 °C for 20-30 minutes. This would safely clean away all organic impurities on the SiC surface.

The final cleaning step would be to clean the chips in 49% HF acid. HF is one of the strongest and most dangerous acids in the world and hence has to be carefully handled. It is extremely hazardous and can cause long lasting damage to the human body. The chips need to be soaked in the HF for

doi:10.6342/NTU202210171

exactly 5 minutes. It cleans away most metal and ionic impurities from the surface, but a longer exposure will lead to the surface itself being damaged by the acid. These are then thoroughly rinsed with DI water for a few minutes each. Cleaning is the most important step in the process of graphene growth. The better the cleaning, the better the growth is what I have observed. The chips are then ready for PASG.

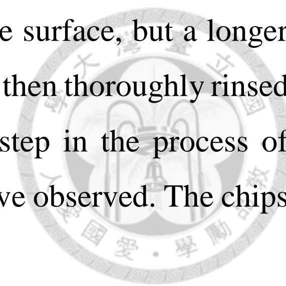

3.2 Epitaxial Graphene Growth and Doping

3.2.1 Polymer Assisted Sublimation Growth

PASG or polymer assisted sublimation growth is a novel method for EG growth first attempted by Krusprof *et. al.* [57]. The idea is that we coat the surface with a polymer to aid in the growth of graphene. The method that we used, involved first making a polymer solution of 75uL AZ5214e in 150mL IPA. This forms a colloidal suspension and hence it is important to shake it well for at least 2 minutes before using it every time. We spin coat this solution on the Si-face of our chips at 4K rpm on a CEE Apogee spin coater. The chips are now ready to be grown.

We follow a face-to-face growth method. This involves placing the SiC chips, Si-face down on a polished graphite planchet. This helps reduce the rate of sublimation of Si atoms and gives us more control over the growth process. It is important to minimize the time lag between the polymer being coated and the chips being placed on the planchet to be loaded into the furnace. When placing the chips on the planchet, one should try to press down gently and move it around to observe an interference pattern. The more circular the pattern looks, the closer the chip is to the graphite surface and consequently, the better the growth (figure 3.3).

doi:10.6342/NTU202210171

The furnace is first pumped and purged with Ar gas coming from a 99.99% liquid Ar source. 2 cycles of pumping and purging are followed by filling the chamber with a forming gas mixture (5% H_2 and 95% Ar). This step ensures a clean chamber at higher temperatures. The H_2 acts as a cleaning agent and eats away at any impurities in the chamber. We gradually bring the chamber to a temperature of 1200 ℃ and soak it at that in the presence of forming gas for 2h. After which, the chamber is purged again and filled with Ar gas. The growth then proceeds by elevating the

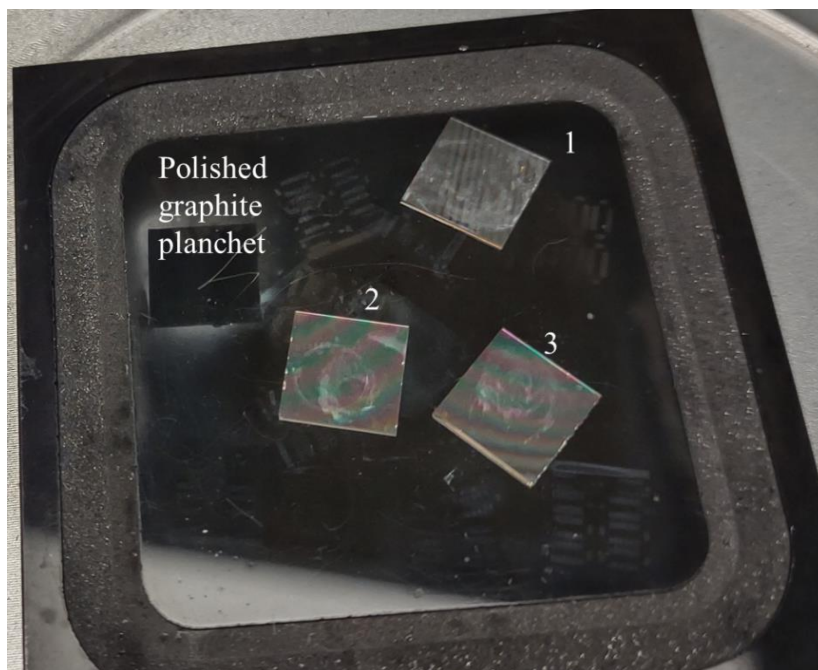

Figure 3.3: Interference fringes on SIC chips. *Chips are placed on a graphite planchet. Chips 2 and 3 have a wider pattern, indicating that the chips are in close contact (<50 μm) with the graphite planchet. Chip 1 has narrow fringes, meaning the chip is not in close contact with the planchet.*

temperature to around 1850 ℃ and holding it there for 3-4 minutes. The heating is immediately stopped and the chamber is cooled through cooling lines flowing around it. Once the chamber reaches RT, we unload the chips. The quality of the graphene grown on these chips can be verified using confocal laser scanning microscopy. AFM can also be used to verify it, as has been done in Figure 2 of reference [17].

3.2.2 Confocal Microscopy

doi:10.6342/NTU202210171

Confocal laser scanning microscopy (CLSM) is a powerful imaging technique. It can filter the out-of-focus light from the unwanted environment light, thereby enhancing the imaging resolution by the spatial pinhole. The spatial resolution in the horizontal directions is ≈ 150 nm for the image and the height resolved down to about 10 nm, respectively. Marvin Minsky patented the idea and design for this type of a microscope in 1957. In a regular optical microscope, the out-of-focus light from the environment makes the images blurry. CLSM uses two pin-holes in front of the laser source such that the detector blocks off the out-of-focus light, leading to sharper images. This also gives the CLSM the ability to perform a 3D scan. Laser scanning a graphene allows us to accurately image the surface of graphene, and determine the roughness, without having to use any expensive imaging like the any electron microscopy. A side-by-side comparison of a epitaxial graphene with and without laser scanning is shown in the figure below. Having this tool at our disposal at NIST has made processing and graphene growth much faster and easier.

doi:10.6342/NTU202210171

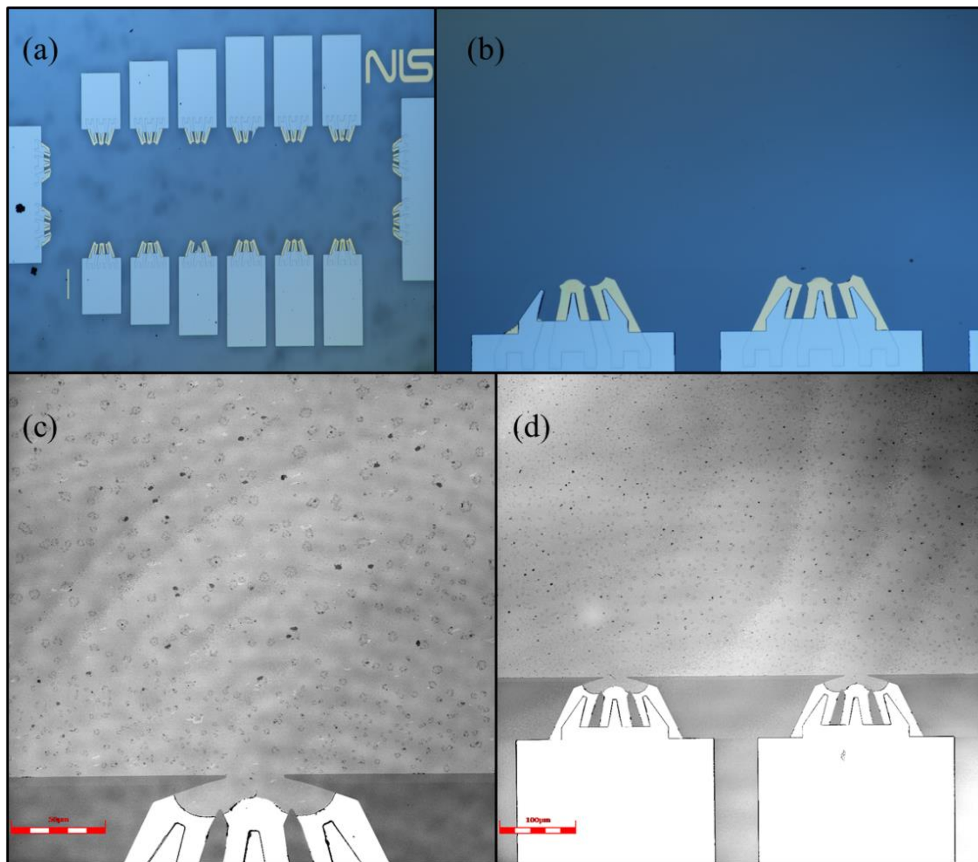

Figure 3.4: Comparison of an optical microscope vs a CLSM. *(a) A sample Hall bar device used to compare the optical microscope with the CLSM. (b) a zoomed in optical image of the device in (a), notice the fine outline of the graphene visible through image manipulation using lookup tables (LUT's). (c) and (d) a close up image of the same region in (b) using a CLSM. The graphene surface and bilayers are clearly visible in these images.*

3.2.3 $Cr(CO)_3$ functionalization

As grown EG has a non-uniform carrier density. In order to control the carrier density, there are two main methods. The first method, a standard in metrology, is $Cr(CO)_3$ functionalization. In order to achieve this, a small N_2 filled furnace is used. The sample space is first heated to 130 °C. The as grown EG chips are then baked in this atmosphere for 1 hr. This bake ensures better adsorption on the EG surface. The $Cr(CO)_3$ source is then loaded in the furnace and allowed to react for 30-45 minutes. Upon completion of the reaction, the chamber is evacuated via a cryo pump to freeze dry the contents of the chamber. Once the chamber is evacuated, the pump

doi:10.6342/NTU202210171

is closed and N_2 is flown back into the chamber to bring it to atmospheric pressure. The chips can then be unloaded.

As stated in the introduction, this method involves physio adsorption, meaning that the $Cr(CO)_3$ is not chemically bonded to the EG surface. Rigosi *et al.* go in depth of the mechanism for the change in carrier density using Langmuir modelling [34]. The beauty of this method is in the ability to 'reset' the carrier density of EG by simply leaving it in ambient atmosphere. The carrier density in this case defaults to around 10^{10} cm^{-2}, close to the Dirac point for EG. It can be increased by annealing it in vacuum. This type of functionalization does not affect quality of graphene, as is proven using precision measurements in [33]. One drawback of this method is that we cannot go towards a *p*-type behavior. There are still ongoing attempts to reliably and controllably tune the carrier density to *p*-type in EG, such as to maintain the EG at metrological standards.

3.2.4 Nitric Acid Doping

While Cr offers *n*-type doping for EG, the N^+ ions in HNO_3 dope the EG to a p-type carrier density. Chapter 4 offers a more in-depth explanation of the doping mechanism. Here we focus on the methodology. Due to the nature of nitric acid, this experiment was conducted in an acid hood. The device was mounted on a Teflon stand specially made for this experiment as shown in figure 3.5. Around 100ml of Nitric acid was poured in a 250 ml beaker. The device was then adjusted to be approximately 3cm from the surface of the acid. Different exposure doses were tried, ranging from 1min to 4 minutes. In order to ensure the most accurate measurements, the device was moved to the electrical measurement setup within 1 minute of the exposure.

doi:10.6342/NTU202210171

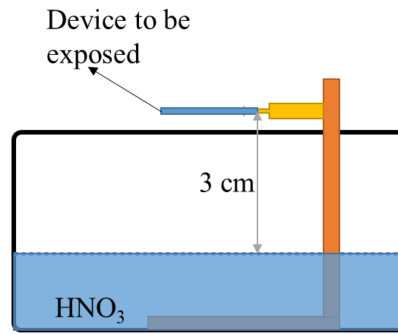

Figure 3.5: ***Nitric acid doping assembly.*** *The Teflon stand, being acid resistant, supports the sample facing downwards at the Nitric acid vapors.*

3.3 Fabrication of Graphene Devices

Once doped, the graphene film can then be fabricated into a Hall bar geometry. The first step of this process is to fabricate the masks required for contact lithography. A Heidelberg 2000 Laser Mask Writer tool was used for this purpose. Resist and chrome coated mask template was then exposed to the pattern shown in Figure 3.6. After careful alignment, a 365 nm laser was used to write the pattern on the mask template. This pattern was then developed in CD-26A developer for 1 minute and rinsed thoroughly with DI water. The chrome was then etched using a chrome etchant. After which the mask was ready to use. We then follow the steps discussed in this section to fabricate graphene devices.

doi:10.6342/NTU202210171

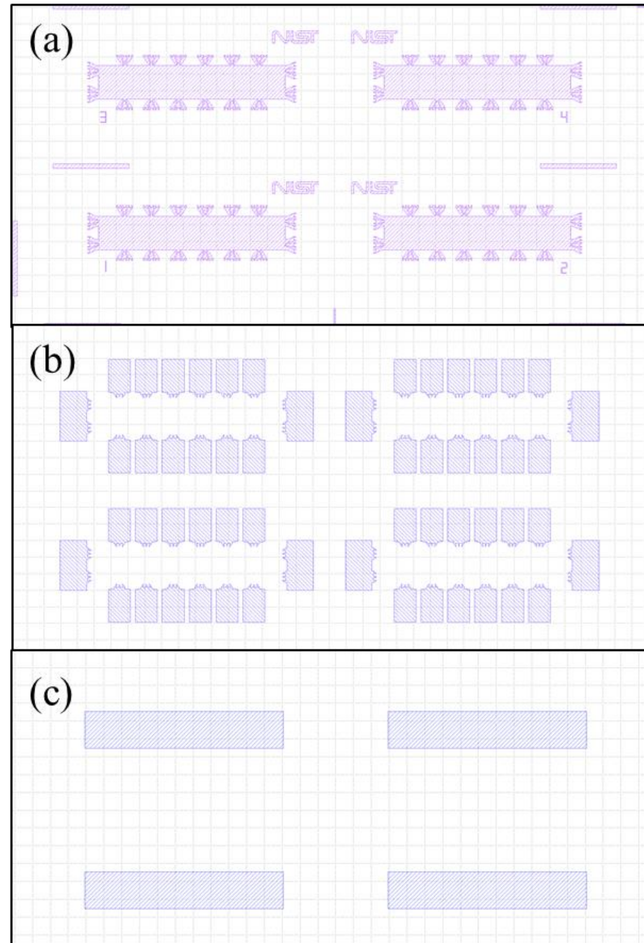

Figure 3.6: Contact lithography masks for Hall bar devices. *(a) First lithography mask, the graphene is etched in that pattern. (b) The mask design for contacts as the second lithography steps. (c) The last lithography step involves opening a window to etch the graphene protective layer using dilute aqua regia.*

Three masks were made, one for each lithography layer. The Cr doped graphene film was first coated with a protective layer of 5 nm Pd/ 5 nm Au. This ensures that the EG remains unaffected during the processing. We then coat these chips with LOR3A, a photoresist used to provide a curved undercut to the sidewalls. It was then baked at 175ºC for 5 minutes. A second layer of photoresist, S1813 was then spun on top of it at 4000 rpm for 55 s. It was then baked at 110°C for 1 minute. The chip was then exposed to the first lithography pattern shown in figure 3.6(a) and developed in CD-26 for 1 minute. The chip was then cleaned using reactive ion etching for 30 s to descum the photoresist. Another layer of 80 nm Au was deposited on this pattern and lifted off using the solvent, PG remover. The chip was then loaded into a Denton infinity 4-wave

doi:10.6342/NTU202210171

ion mill. The ion mill uses high energy plasma to etch away the graphene not covered by the photoresist, leaving behind graphene in a Hall bar geometry as shown in figure 3.6(a).

Contact pads were then patterned onto the graphene using the mask for the second lithography layer as shown in figure 3.6(b). NbTiN was selected as the contact material based on [58]. These superconducting contacts offer a close to zero contact resistance for quantum Hall measurements at low temperatures. To deposit this material, RF sputtering tool was used. A NbN target was run in parallel with a Ti target along with 30 sccm of N_2 gas flow. Running this for 5 minutes deposits around 200 nm of NbTiN on the surface. A 3rd DC target for Pt was used as a capping layer to prevent the oxidation of the NbTiN surface. The metal was then lifted off, leaving behind graphene with NbTiN contacts. Although the depiction in figure 3.6 (e) denotes an ideal case, sputtering is generally non-directional, so it is unlikely that the contacts would contact the edges of the EG and instead would completely cover the Pd/Au layer which would provide a conductive pathway which would allow for the bands of the NbTiN to align with the EG.

The third lithography step is to open a window over the protected graphene (as shown in figure 3.6(c)) in order to etch the protective layer and expose the graphene. A dilute solution of aqua-regia is mixed using a ratio of DI water: HCl: HNO_3 as 1:3:4 or 1:3:7 depending on the amount of control required over the etching process. These steps are outlined in the figure below:

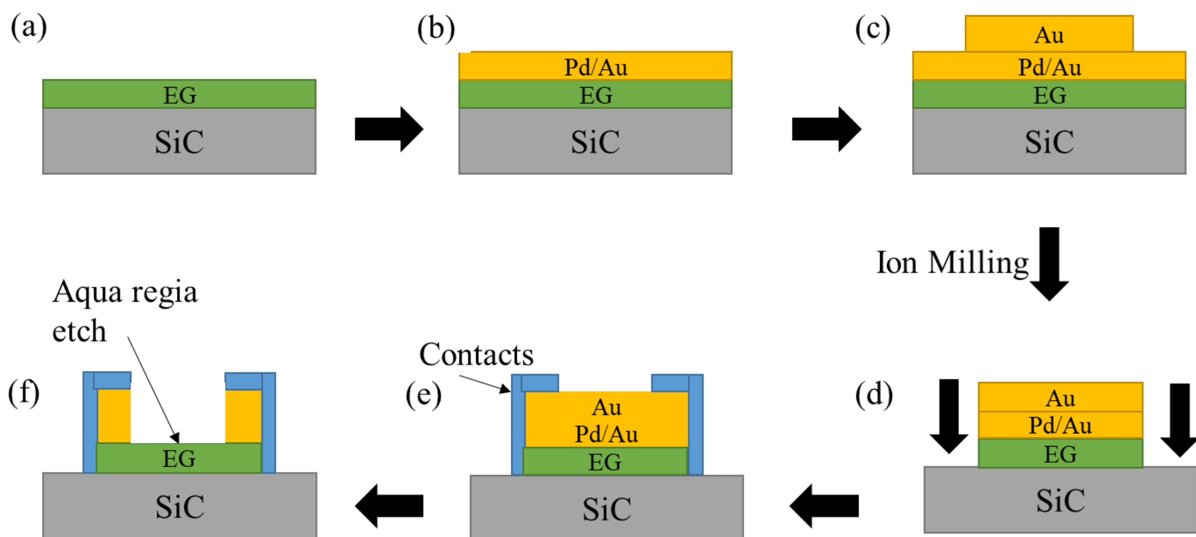

*Figure 3.7: **Graphene device fabrication process.** (a) Cross-section of the as grown EG is coated with a protective layer (b), after lifting off the first lithography layer, we have a material stack as shown in (c). (d) Shows the chip post ion-milling. (e) Device after lifting off the second lithography layer. (f) Aqua regia etches the protective layer leaving behind n-doped EG.*

doi:10.6342/NTU202210171

Once the device has been fabricated, we can then mount it on a chip carrier for us to perform electro-magnetic characterization. We use a T-08 or LCC-32 pin carriers (Figure 3.8). The TO-8 hasAu pins which prevent thermocouples from forming as in the case of LCC-32 which has Au pads but that itself is mounted on a silver holder, which at certain conditions may lead to the formation of thermocouples, giving us unwanted signals. The chip is then connected to the carrier via wirebonding. It is the process of attaching a thin Au/Al wire to the contact pads and connecting it to the pads of the chip carrier. The attachment or bonding is achieved by threading the wire through an ultrasonic needle. The temperature, force, ultrasonic power, contact time can be manipulated to achieve a good bond, depending on the wire and the surface being bonded. Au being a naturally soft metal, requires higher power with lower force and time. Whereas Al requires a higher power and force to be able to form a strong bond with the contact pads.

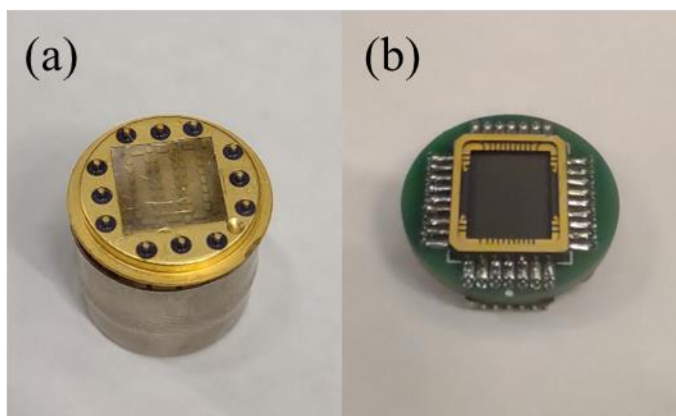

Figure 3.8: Chip carriers. *(a) A 12-pin TO-8 chip carrier with a sample device mounted and wirebonded. (b) an LCC 32-pin chip carrier.*

3.4 Raman Spectroscopy

doi:10.6342/NTU202210171

Raman spectroscopy is a quick tool that helps us analyze graphene and find the number of layers, orientation, doping, strain, functional groups and disorder in graphene[59]. When a sample is exposed to a monochromatic light, it will either undergo an inelastic Raman scattering or Raleigh scattering. We can filter out the elastically scattered light at the incident wavelength, such that the remaining light, which has been inelastically scattered can be analyzed. By measuring the change in energy of the Raman scattered light, one is able to figure out the corresponding energy of the materials phonon modes. The light can either relax into a lower energy state while releasing a higher energy photon (anti-Stokes scattering) or it can excite the system into a higher energy state (Stokes scattering. The energies of these possible phonon modes and shift are specific to a particular electronic structure or a bond of a material, once can easily identify the chemical bonds present in the sample.

The Raman spectra of our epitaxial graphene devices is a superposition of the graphene and the SiC substrate. Hence, we need to subtract the SiC background signal from the raw data. The Raman spectra of our EG shows three significant peaks, 1) the D peak at around 1350 cm^{-1}, 2) the G peak at around 1582 cm^{-1} 3) the 2D peak at around 2700 $cm^{-1.}$ The G and the 2D peak are always present whereas, the D peak is only seen when there are some structural defects or disorder in the EG lattice. Such defects may arise from a disruption of the lattice periodicity such as edges, defects or grain boundaries. In pristine graphene, the in plane vibrational mode corresponding to the E_{2g} phonon mode at the center of the Brillouin zone results in the G peak. The A_{1g} breathing mode of the ring of 6 carbon atoms can only be observed at the edges or near defects and hence it manifests itself as the D peak in the Raman spectra. When two phonons of the opposite wave vectors produce an overtone, it is observable as the 2D peak[60]. This 2D peak can be observed in pristine graphene even though there are no defects, because of conservation of momentum followed by the two opposing wave-vectors.

3.5 Electrical and Magneto-Characterization

doi:10.6342/NTU202210171

3.5.1 Basic electrical measurements

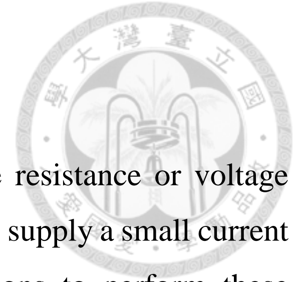

The most basic electrical characterization to be performed is the resistance or voltage measurement on any device. We then use a Keithley 2612A source meter to supply a small current and measure the voltage across the device. There are two configurations to perform these measurements, the two-probe method and the four-probe method. The two-Probe method provides a quick measurement but fails to exclude contact resistance. At room temperatures, the contact resistances can be significant and thus lead to inaccurate results. The four-probe method however, bypasses the contact resistance by measuring the voltage signal at a different pair of contacts than the source and drain. This can be realized as follows.

Consider a device under test (DUT) with a resistance R_0, with lead resistances for leads 1 and 2 being r_1 and r_2, as shown in the figure below:

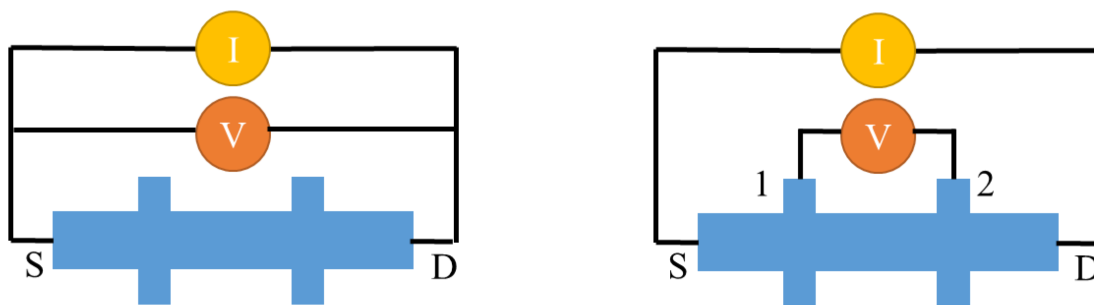

Figure 2: Two terminal and Four terminal measurement configuration. *Left- Two terminal measurement where the voltage is measured at the same terminals as the current is injected. Right- Four terminal measurement with the voltage is measured at two other terminals.*

For the two-terminal case, the voltage measured would be $V = I\,(r_1 + R_0 + r_2)$. While for the four-terminal case, the current flows through lead 1, into the voltmeter, and back into the DUT. This means that the voltmeter draws very little current from the circuit, leading to it measuring the 'true' voltage to be measured, irrespective of the lead resistances.

doi:10.6342/NTU202210171

3.5.2 Current Sources and Voltmeters

For our experiments, we used various current and voltmeters. The most commonly used instrument was the SR-830 lock-in amplifier. Lock-in amplifiers provide the best way to measure an accurate signal from an extremely noisy environment. It essentially takes the input signal, multiplies it by a reference signal, and then integrates it over a certain time period, resulting in it filtering any signal that does not have the same frequency as the reference signal. The out-of-phase signal that has the same frequency is also attenuated, meaning the lock-in amplifier is also phase-sensitive detector.

The Keithley 2612A is the main DC current source for our experiments. It is a dual channel meter with the ability to simultaneously source a DC current with one channel and measure a voltage with the other. It can also perform two terminal DC measurements using a single channel. This versatility made it essential for our DC measurements. The HP34420A nanovoltmeter was used to measure very low voltages with a high precision. While the N11 analogue nanovoltmeter was primarily used to perform longitudinal resistance measurements. The longitudinal resistance is supposed to ideally be zero, however, in practical applications, we measure a few milli-ohms of longitudinal resistance. In order to measure a signal that small, the N11 provides amplification. This meter can be connected to a digital multimeter like the HP3458 to digitally record the values from the N11 analogue voltmeter.

3.5.3 Janis Cryostat

The Janis cryostat is the crowning jewel of the Graphene lab at the Physical measurement laboratory at NIST. It is a lambda point wet cryostat which requires a constant supply of liquid helium and liquid nitrogen to keep functioning. It costs a fortune to run, but rewards its users with a superfast turnaround time. A device can be cooled from RT to 1.5 K in 30-40 minutes, which is at least 8-10 times faster than conventional recirculation systems. There are two probes available with this system. One has a T-08 holder while the other has a LCC-32 pin carrier. The T-08 probe

doi:10.6342/NTU202210171

is being phased out due to its limited number of connecting pins when compared to the LCC-32 pin carrier.

The cryostat has a very delicate design and balance. Every chamber is separated by a small vacuum space. This prevents thermal leaks and helps keep a temperature gradient within the system. The probe space is first pumped down to -25 mbarr before opening the HIVAC valve to the main sample space. The probe is then slowly lowered into the chamber, this is to avoid introducing a hot body into a liquid helium reservoir and boil off excess helium. A slow descent cools the sample slowly and by the time it reaches nearer to the LHe reservoir, it is already in equilibrium. The needle valve is then adjusted to increase or decrease the temperature. As the LHe flows through the thin needle valve, it expands and absorbs heat from the sample, cooling it. All the while, the sample space is constantly pumped to pump out the not-a-liquid-anymore He gas. Temperatures as low as 1.4 K can be achieved using this technique. The sample space needs to be continuously pumped to get rid of the excess hot gasses.

The Janis comes equipped with a 9 T superconducting magnet. This magnet is always immersed in the Lhe reservoir of the Janis. This allows the magnet to remain cold passively. The sample sits exactly in the center of this magnet, allowing it to experience a perpendicular field of up to ± 9 T.

doi:10.6342/NTU202210171

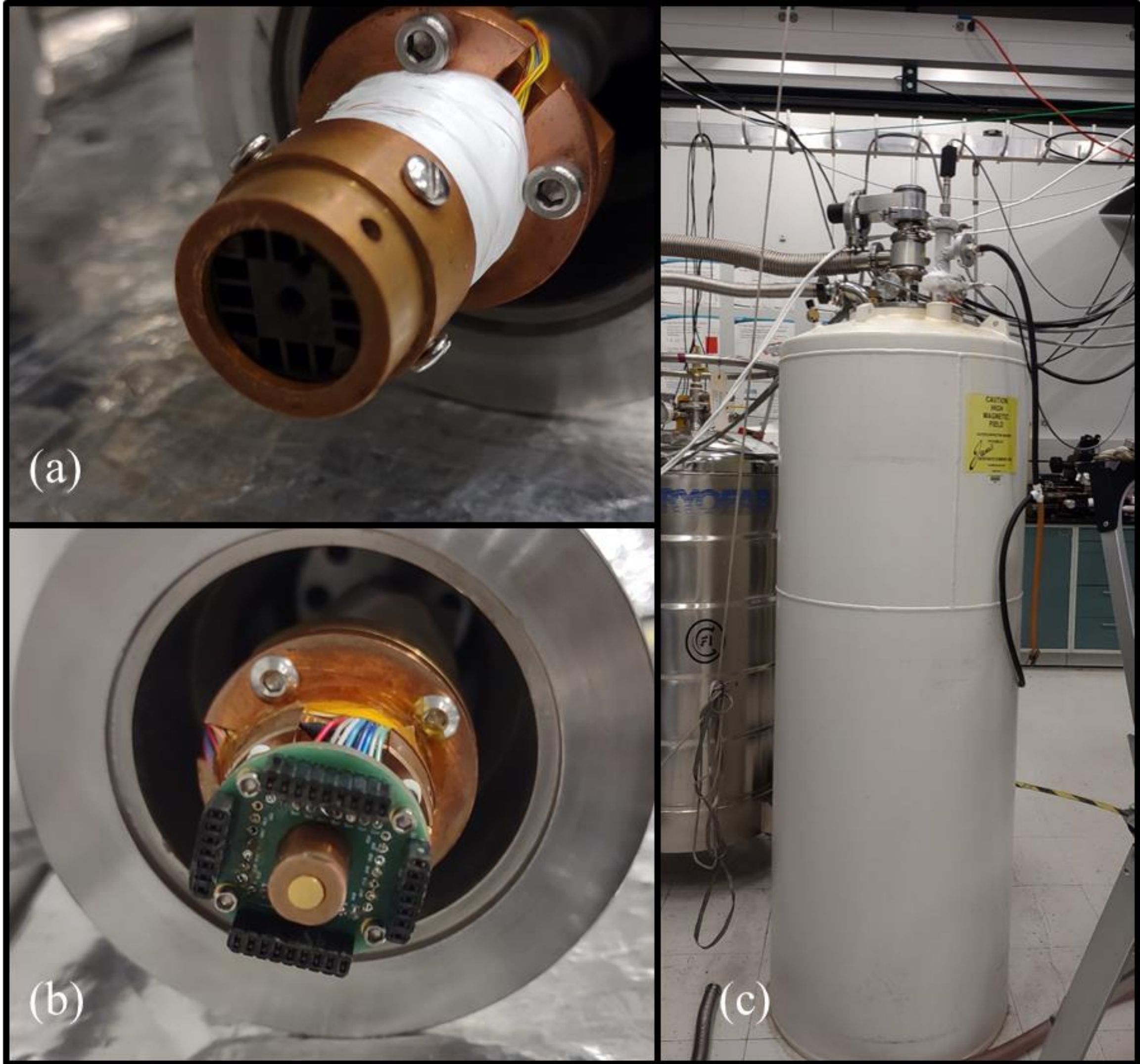

Figure 3.9: The Janis cryogenic system. *(a) Janis probe with a TO-8 mount. (b) Janis probe with an LCC-32 pin mount. (c) The Janis cryogenic system.*

doi:10.6342/NTU202210171

Chapter 4 Dynamics of Transient Hole Doping in Epitaxial Graphene

In this chapter, by using nitric acid as an adsorbent, the dynamics behind hole doping in EG are studied. Although literature exists describing these interactions [61-63], elements such as timescales associated with these processes remain to be understood. Understanding of these processes is very important for any 2D material meant to be fabricated into devices with some particular functionality, for example, devices exhibiting photovoltaic properties [64, 65] , charge density waves [66, 67], or *p-n* junctions [34, 68-72]. Moreover, the large-scale gating that opens up from the understanding of these processes can also be directly applied to photodetection, [73-77] and electron optics [78-80]. In particular, our focus here is on the low and room temperature data on the quantum transport of these devices. The main idea was to gain information about the timescales associated with the desorption process, in other words, its transient behaviour, and to this end, we monitor electrical properties of these devices after exposing it to nitric acid. In order to replicate the common laboratory conditions under which such devices would be handled, we performed these measurements under ambient conditions. In order to compare the relevant timescales obtained from the transport data to the devices optical properties, we use Raman spectroscopy. The results are supported through some discussions on a Langmuir model and these have allow us to understand how to interpret the time constants we obtained from the data.

4.1 Experimental description

The devices for the purpose of this experiments were fabricated using techniques described in the previous chapter. A single Hall bar device with multiple Hall voltage probes were fabricated, as shown in the figure 4.1. The device in Figure 4.1(a) was a part of another ongoing experiment, but was used as a functionalized device, doped with $Cr(CO)_3$. The device in figure 4.1(b) was used

doi:10.6342/NTU202210171

as the control device, the one which was to be doped using Nitric acid. The example CLSM image was captured from the region indicated by the blue box, the image is shown in figure 4.1 (d) and confirms that the as grown EG is homogenous. Fig. 1(c) shows an example of undergrown EG for comparison, we would however not use such a material for device fabrication.

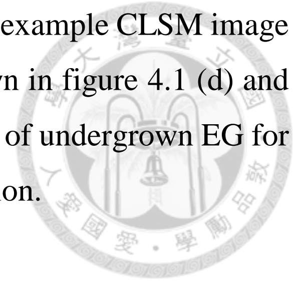

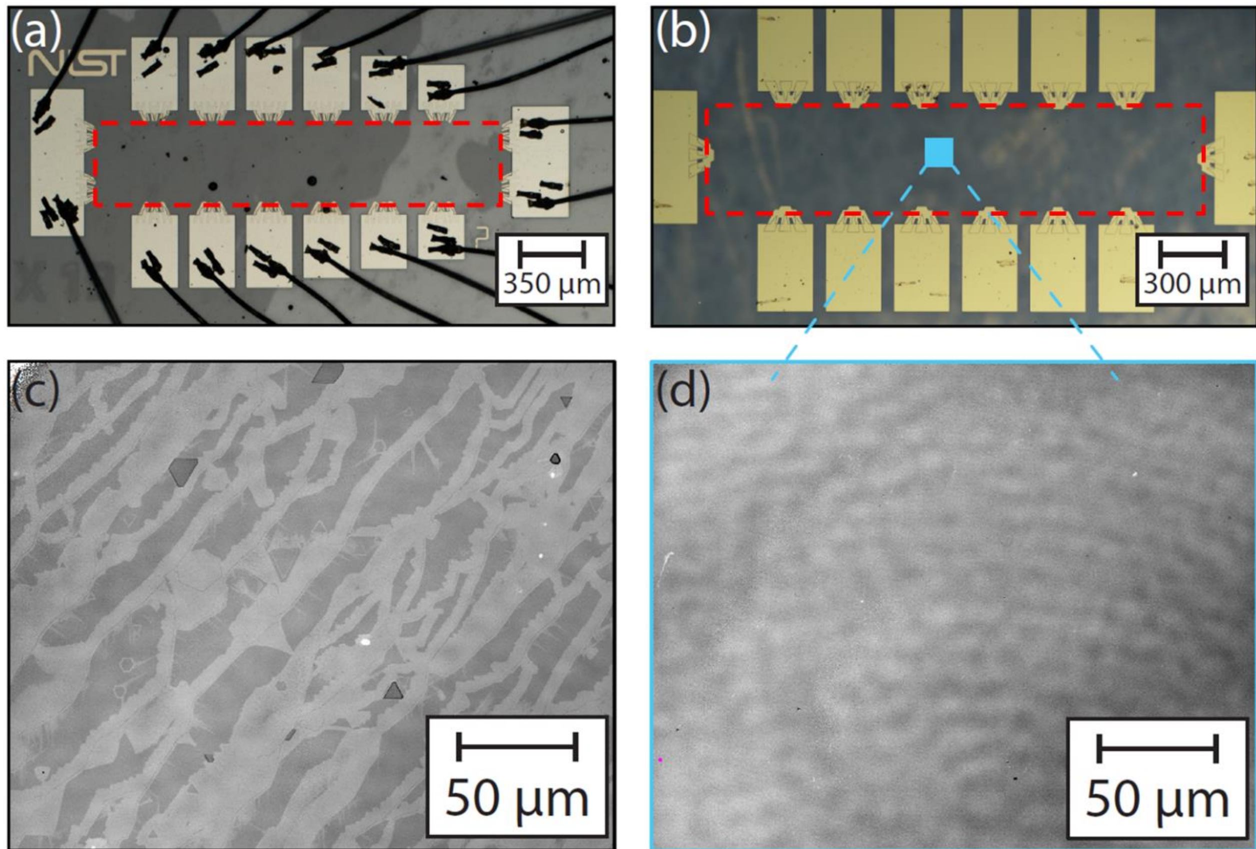

Figure 4.1 Devices for the Nitric Acid doping experiment and the EG quality. *(a) An optical image of the functionalized device. The black spots visible on the surface of the graphene are the products of the $Cr(CO)_3$ functionalization process, which only dope the graphene and do not affect it in any other way. (b) An optical image of a control device. The blue box indicates the area inspected for the quality of the graphene using CLSM. The red dashed box in both (a) and (b) indicates the epitaxial graphene area. (c) CLSM image of an example undergrown EG on SiC (d) CLSM image of the area in (b) which looks ideal with respect to homogeneity of the EG.*

The Janis Cryogenics system was used for quantum Hall transport measurements. All data was collected at magnetic fields between -9 T and 9 T and temperatures of 1.5 K, in order to

doi:10.6342/NTU202210171

determine the initial hole doping of each device. A standard fume hood was used to consistently expose all the samples to nitric acid vapors. Each exposure was done by keeping the face of the EG devices about 3cm from the surface of the liquid for 2 minutes. The time was selected based on previous reports about fast timescales for NO_3 adsorption on EG [62]. A source-drain current of 1 μA was applied and lock-in amplifiers were used to monitor the longitudinal resistances for each device.

Raman spectroscopy was employed for a dual purpose of first confirming the homogeneity of the EG layer and then to monitor its 2D (G') mode. These measurements were performed with a Renishaw InVia micro-Raman spectrometer using a 633 nm wavelength excitation laser source. All spectra were measured and collected using a backscattering configuration, 1 μm spot size, 300 s acquisition time, 1.7 mW power, 50 × objective, and 1200 mm^{-1} grating. To confirm the EG quality, rectangular Raman maps were collected with a 20 μm step size in a 5x3 raster-style grid. Many data sets were collected on a single point on the film after nitric acid exposure with a 30 s delay between measurements to monitor the time dependent behaviour.

4.2 Transport and transient doping

After exposing the control devices to nitric acid, an immediate transport measurement was performed to extract the hole density (n_h) at 1.5 K. A standard Hall measurement data for a control device is shown in Figure 4.2 (a) as a red dashed line and a black line. Another example data set of Hall measurements for a functionalized device is shown in blue, orange and green curves of different dash lengths. n_h was calculated from the Hall slope at low magnetic fields of less than 1 T. The average initial hole carrier density for the control and functionalized devices in figure 4.2 (a) were around 1.6×10^{11} cm^{-2} and 1.1×10^{12} cm^{-2}, respectively. Several pairs of contacts were used to monitor the changing R_{xx} for both control and functionalized devices after exposure to nitric acid vapors. A sample set of results are shown in Figure 4.2 (b) for a control device. Note that all the pairs of contacts used for this are from the same device.

doi:10.6342/NTU202210171

The variation of hole density throughout the control device is apparent from the varying values of R_{xx}. This is a typical behavior for such EG devices, and hence was a primary motivation for the $Cr(CO)_3$ functionalization process [34]. These treated devices will show more stable and predictable behavior in later figures. To reveal more information about the desorption process, one would have to look at the hole doping change with time. Therefore, low-field determinations of n_h are repeated to extract an approximate relationship between n_h and R_{xx} for every device. Such relationships are plotted in Figure. 4.2 (c), for two example control devices. A suitable fit with a characteristic function are necessary in order to transform the time-dependent R_{xx} curve to a time-dependent n_h curve. The ansatz or the assumed function chosen for such a fit was based on a Langmuir curve (with a, b, and c as constants), the reason for this choice would soon be described.

$$R_{xx} = \frac{1}{a + b{n_h}^{c-1}} \tag{4.1}$$

The last point that needed to be addressed is that the relationship between the room temperature longitudinal resistance and the hole density at 1.5 K is a reasonable 1:1 correspondence. Not meeting this condition would lead to confusion and inaccuracies in any further analysis for the time dependent hole carrier density. Hence, we show a set of longitudinal resistance measurements in Figure 4.2 (d) as a function of temperature from a single control device. This supports the fact that there is a 1:1 mapping from the room temperature R_{xx} to n_h at 1.5 K. [81].

doi:10.6342/NTU202210171

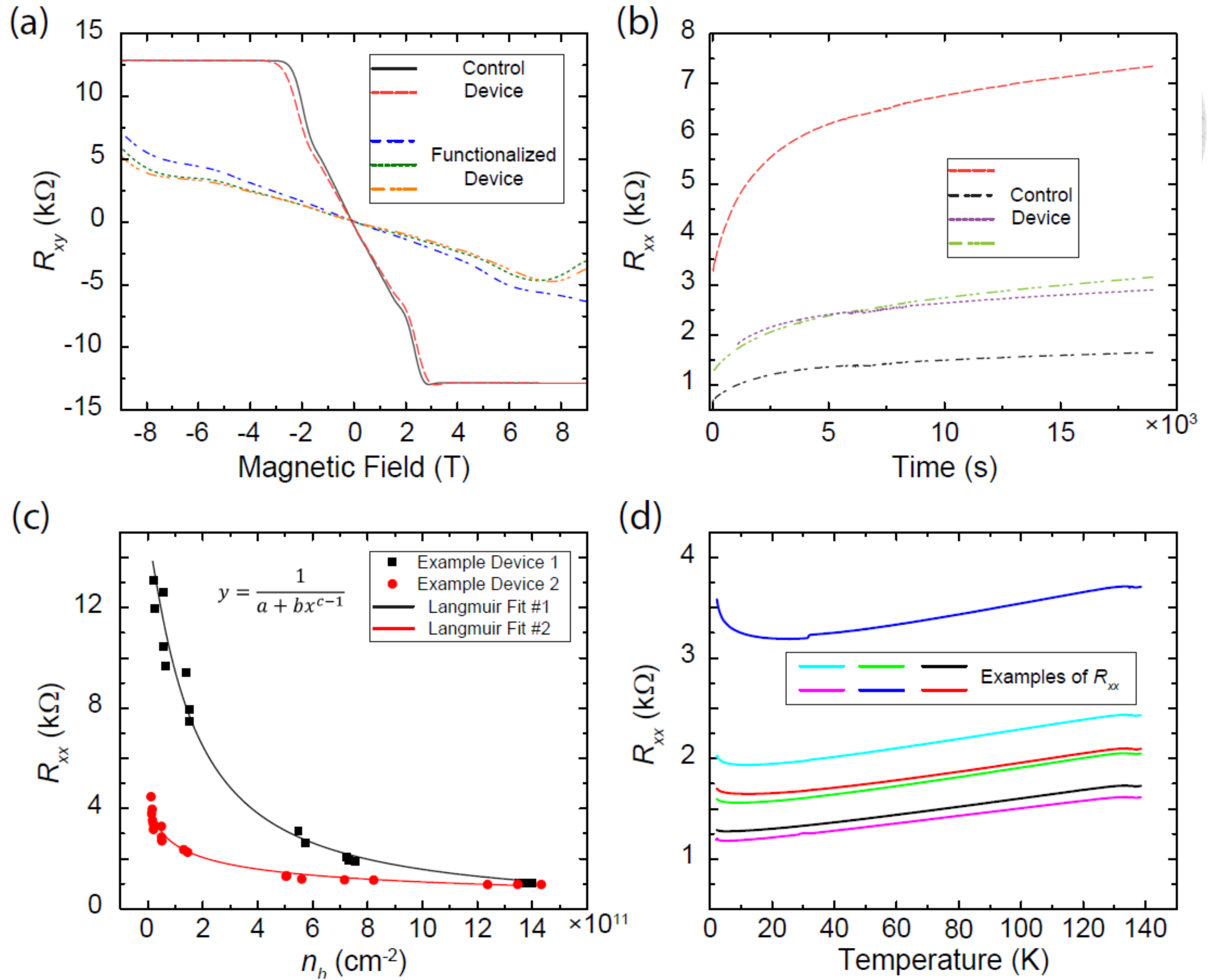

Figure 4.2: Transport and electrical data for the doping experiments. *(a) A set of Hall measurement data on a control (dashed red and solid black curves) and a functionalized device (green, blue, and orange curves). The hole densities (n_h) post-exposure were calculated using the slopes of the Hall curves at magnetic fields of less than 1 T. (b) Longitudinal resistances (R_{xx}) for different pairs of adjacent contacts of the control device in the xx direction measured after the nitric acid exposure. (c) An approximate relationship between R_{xx} and n_h extracted from measurements on two example devices. These relationships are unique to each device. (d) Verification of the 1:1 mapping of the R_{xx} values between 300 K and 1.5 K by measuring the R_{xx} as a function of temperature from a single device.*

doi:10.6342/NTU202210171

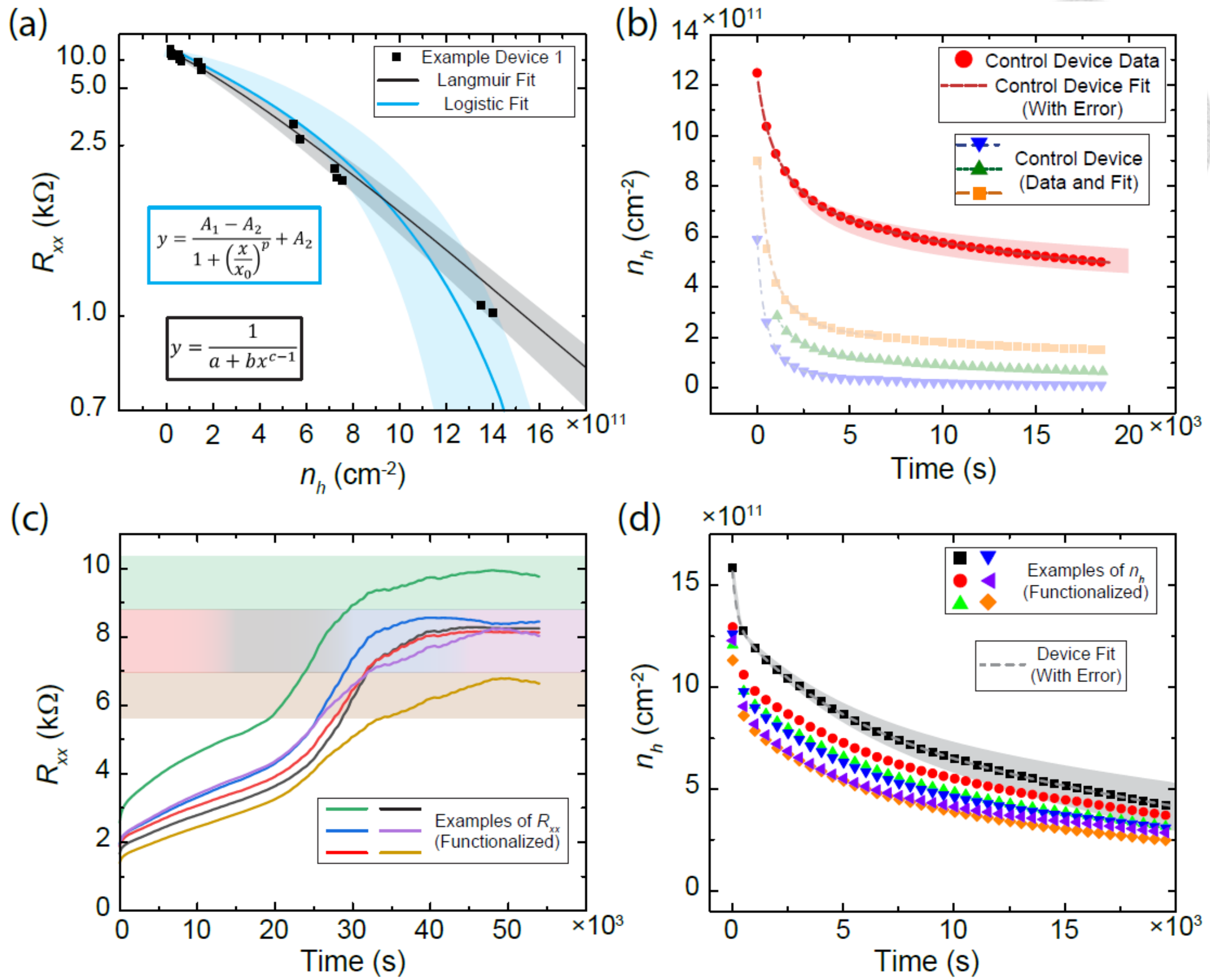

__Figure 4.3: Extracting time constants__. (a) A comparison of error between a Logistic fit (cyan) and Langmuir fit (black) showing that the Langmuir fit is suited to obtain a relationship between R_{xx} and n_h. The gray and blue shaded region from the fitting procedure indicate a 1σ error. (b) Each R_{xx} data is transformed to n_h using Langmuir fitting. The shaded region for the top data indicates a 1σ error from the fitting procedure. In order to prevent any significant overlap with the other three curves, it is only shown for the top data set. (c)In order to highlight the stabilizing property of the treatment, an example data for R_{xx} over a long duration from a functionalized device are shown. The polarity of the charge carrier may change due to the Fermi level being close to the Dirac point. Hence, the curves are color-matched to the corresponding shaded regions which indicate a region where the charge polarity may change. (d) The data in (c) is transformed to extract the time constants that characterize their doping behaviour, and example of a fit is shown for the topmost curve.

doi:10.6342/NTU202210171

The ideal relationship between the R_{xx} and n_h is approximately reciprocal and maybe used to justify the use of the Langmuir fit [82]. Another possible type of fitting one may use would be the Logistic fit (as shown in Figure 4.3 (a)) as shown below, where A_1, A_2, x_0, and p are constants:

$$R_{xx} = \frac{A_1 - A_2}{1 + \left(\frac{n_h}{x_0}\right)^p} + A_2 \tag{4.2}$$

The fitting procedures, in this work done using Origin Labs, usually have errors associated with them, these are useful to compare the adequacy of the fits, as done in Figure 4.3 (a) for an example control device. Comparing the Logistic fir (cyan) and a Langmuir fit (black) shows a clear indication that the Langmuir fit is a better indicator of the relationship between the longitudinal resistance and the hole carrier density. A 1σ error from the fitting procedure is indicated by the gray and blue shaded region. The obtained Langmuir fits are then used to transform the corresponding R_{xx} data to n_h, as shown in Figure 4.3 (b). The shaded region in this figure, indicates a1σ error from the fitting procedure. Only the top data is shown with the error in order to prevent any overlap between the other three curves. These curves correspond to the Figure 4.2 (b).

Using the data from the functionalized devices, we can perform similar transformations. For example, a set of R_{xx} data over a long period of time are shown in Figure 4.3(c), to emphasize the asymptotic behavior induced by the treatment. The polarity of the charge carrier may change due to the Fermi level being close to the Dirac point. Hence, the curves are color-matched to the corresponding shaded regions which indicate a region where the charge polarity may change. To demonstrate that the functionalized devices have a smaller variation in hole density and that similar time constants can be extracted, an example of the final transformed data are shown in Figure 4.3 (d). A dashed gray line with a gray shaded region corresponding to the 1σ fitting error is shown. Additionally, we must note that the functionalized devices consistently started at the same initial n_h post-exposure around a similar range of 10^{10} cm^{-2}), providing a more predictable doping process compared to the control devices, which had their post exposure n_h varying by around10^{11} cm^{-2}.

A three-term exponential decay was used to fit the data in order to account for the several desorbed species of molecules like NO_3, NO_2, and water that form after dissociation of nitric acid. These species get physiosorbed onto the EG surface[62]. When compared to a two term or one

doi:10.6342/NTU202210171

term decay, the three-term decays provided an optimized reduced chi-squared. We extracted three time constants from all the collected data, which are 204 s ± 95 s, 2575 s ± 326 s, and 7.35×10^4 s ± 2.43×10^4 s, to be denoted as τ_1, τ_2, and τ_3, respectively. In order to fully understand these constants, some more analysis on Langmuir modeling is required. This should not be confused with the previously described Langmuir fit which we used to transform the R_{xx} to n_h.

Figure 4.4 shows the analysis (based on Figure 4.3 (b)) to justify why a three-term exponential decay was more optimal than either a single- or double-term decay. The two-term decay has a worse reduced chi-squared when compared with the three-term decays, and so one may also rely on the existing knowledge of physical desorption processes of other species (like water and oxygen) to make a clearer distinction between the two different fitting procedures, as well as the knowledge that NO_2 is present on the EG surface.

doi:10.6342/NTU202210171

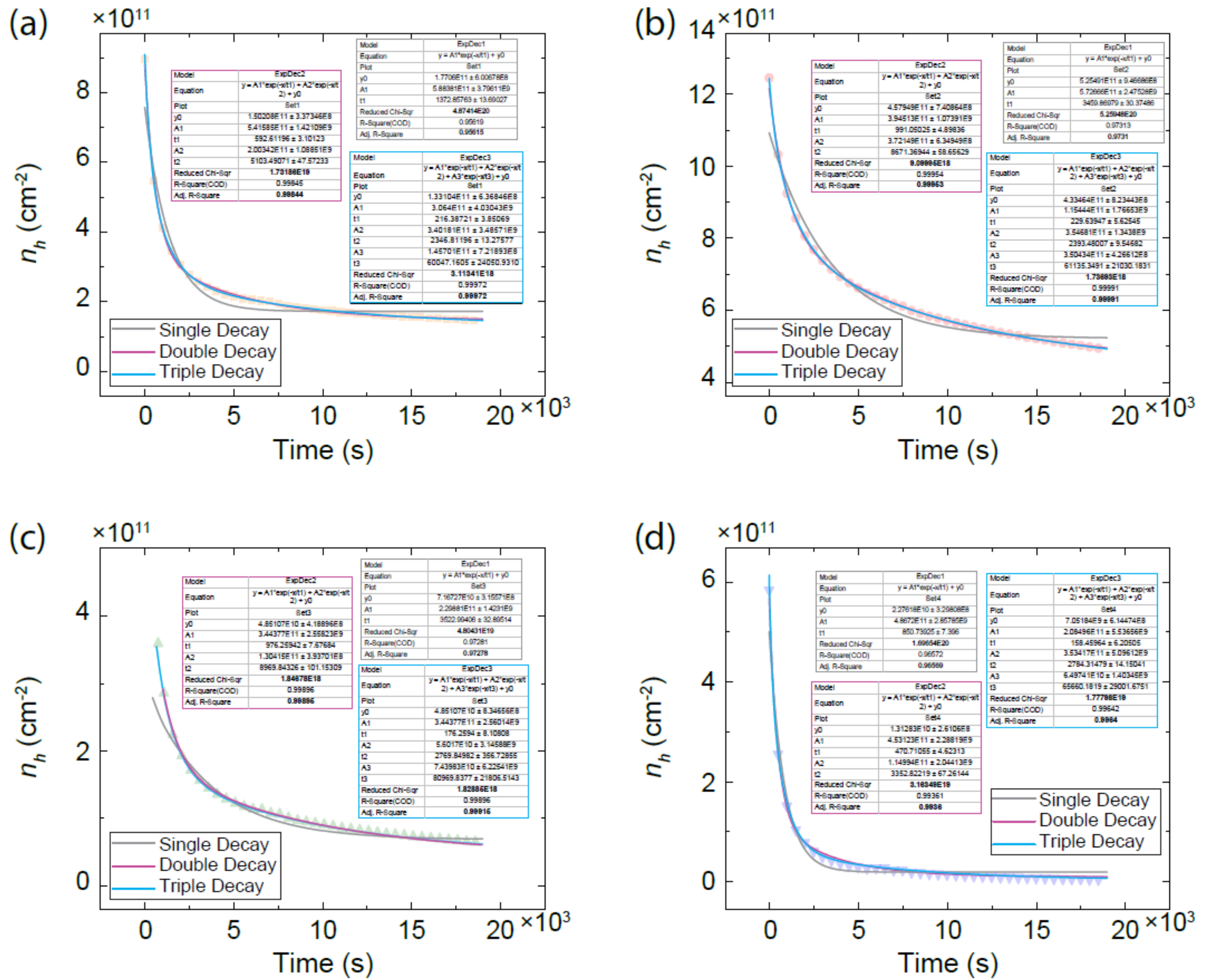

Figure 4.4: Exponential decay analysis. *Each Langmuir fit was used to transform the corresponding R_{xx} data to n_h. (a)-(d) Each time dependent n_h curve was fit to single-, double-, and triple-term exponential decay fits to verify the quality of the lattermost fit.*

Figure 4.5 shows all fits from Fig. 4.3 (d) to demonstrate the ability of extracting similar time constants. These data are just a subset of all data from control and functionalized devices.

doi:10.6342/NTU202210171

Figure 4.5. Exponential decay analysis II. *Each curve from Fig. 4.3 (d) is fit to a triple-term exponential decay to extract the relevant time constants. These data are just a subset of all data collected from control and functionalized devices.*

doi:10.6342/NTU202210171

4.3 Langmuir modelling and Raman monitoring

4.3.1 Three-Species Langmuir Model

The important question to answer involves how one may best interpret these time constants. The interpretations become a lot more straightforward for short monitoring times when we assume that the adsorbents saturate the EG surface post exposure. From previous literature on NO_2 adsorption on EG have shown time constants for this molecule being of the order of 100 s [83, 84]. This value matches quite well with the value we extracted for τ_1. There is literature also available which say that the adsorption of water and oxygen on graphene take place on the order of a few hours [85-89], and that there should not be any immediate competing effects at such short timescales. The third and the longest time constant (τ_3) may be compared with a very similar value obtained from previous literature that discusses that time constant as representing the desorption of water from the surface of EG. They reported a value of about 7×10^4 s, which again matches with the order we obtained[34]. By eliminations, we can then conclude that the remaining component of the nitric acid byproducts, NO_3, can be described by τ_2.

When competing with oxygen, water has been shown to be the dominant contributor to the desorption process. However, one cannot assume that to be true for a three species competition at longer times. Meaning its long enough to neglect contributions from NO2. Although a two species Langmuir model has been shown in the literature [90], a three-species model has not been shown. We took the opportunity and tried to set it up. To do this, we set up the three ordinary differential equations that describe the partial occupancies of NO_3, oxygen, and water on EG sites[90]:

doi:10.6342/NTU202210171

$$\frac{d\theta_{i,j,k}}{dt} = k_{i,j,k(A)}p_{i,j,k}\big(1 - \theta_i(t) - \theta_j(t) - \theta_k(t)\big) - k_{i,j,k(D)}\theta_{i,j,k}(t) \tag{4.3}$$

Here, i, j, and k represent each of the three competing species. In all cases, $k_{(A)}$ and $k_{(D)}$ are adsorption and desorption rate constants, respectively. Rate constants take on the following form: $k_{A,D} = \nu\ exp\left[\frac{-E_{ads,des}}{k_{\mathrm{B}}T}\right]$, with E_{ads} and E_{des} as the adsorption and desorption energy per molecule, respectively, ν is the attempt frequency (typically approximated as 10^{13} s^{-1} [34]), k_{B} is the Boltzmann constant, and T is temperature (K). We can define the term $P_{(LD)}$ as the Langmuir desorption pressure, which is unique to each of the gas species, and can be written as:

$$P_{LD} = \frac{k_{\mathrm{B}}T}{\left(\frac{h^2}{2\pi m k_{\mathrm{B}}T}\right)^{3/2}} \tag{4.4}$$

In order to avoid confusing the units, it is important to convert all the listen quantities in the equation to SI units or keep them limitless. In Eq. 4.4, h is the Planck constant, and m is the mass of a single molecule of one of the gas species (kg). Combining all of these elements with Eq. 4.3 we can solve for equilibrium occupancies, where the steady state solutions can be written as[90]:

$$\theta_{i,j,k} = \frac{p_{i,j,k}}{p_{i,j,k} + P_{i,j,k\ (LD)}exp\left[\frac{-E_{i,j,k}}{k_{\mathrm{B}}T}\right]\left[1 + \frac{p_{j,k,i}}{P_{j,k,i\ (LD)}}exp\left[\frac{E_{j,k,i}}{k_{\mathrm{B}}T}\right] + \frac{p_{k,i,j}}{P_{k,i,j\ (LD)}}exp\left[\frac{E_{k,i,j}}{k_{\mathrm{B}}T}\right]\right]} \tag{4.5}$$

In Eq. 4.5, p is the partial pressure (with the fractional form multiplied by the total pressure) of the gas species, which is about 0.209 for oxygen and 0.00916 for water at room temperature and 40 % relative humidity under normal ambient conditions. The net adsorption energy E is 0.15 eV and 0.1 eV for oxygen and water, respectively [86, 87]. To get any occupancy information, we need to estimate the partial pressure. For this, we use Fick's laws of diffusion along with the conditions that there are no significant air currents. We can safely use it since the probe we used has a metal casing to cover the sample holder. The mean squared displacement may be estimated as $6Dt$,

doi:10.6342/NTU202210171

where t is the time spent diffusing and D is the diffusion coefficient, which may be approximated as 10^{-5} m^2/s [91]. The condition is that a saturated sample may have most of its sites occupied, and for a 1 cm^2 area, this would amount to about 10^{15} cm^{-2} molecules.

With those conditions, one may calculate the square root of the mean squared displacement to get a example distances of about 1 cm, 25 cm, and 75 cm for the corresponding example times of t_α = 200 s, t_β = 1000 s, and t_γ = 8000 s, respectively, post exposure. These times were selected to avoid any dominant transient effects from NO_2. Spreading these molecules out from the surface of EG to the volume of diffusion yields the following three unitless partial pressures: $p_\alpha = 10^{-4}$, $p_\beta = 4 \times 10^{-6}$, and $p_\gamma = 1.33 \times 10^{-6}$. The final element needed is net adsorption energy, and this can be approximated by the rate constant formula after Eq. 3. By inverting τ_{NO_3} ($E_{des} \approx$ 1 eV) and the adsorption saturation time of 10 s (upper bound, $E_{ads} \approx$ 0.8 eV) from Ref [62], the net 0.2 eV allows one to calculate occupancies. Note that in Ref. [13], the calculation for two competing species yielded the result of about $\theta_{O_2} = 89.3$ % and $\theta_{H_2O} = 10.7$ %.

If one assumes the partial pressure at each time to be held constant, then the following occupancies serve as a lower bound estimate given the saturation of NO_3. At 200 s, the expected steady state occupancies are: $\theta_{O_2} = 84.4$ %, $\theta_{O_2} = 10.1$ %, and $\theta_{H_2O} = 5.5$ %. At 1000 s, the resulting occupancies are: $\theta_{O_2} = 89.0$ %, $\theta_{O_2} = 10.7$ %, and $\theta_{H_2O} = 0.3$ %. Lastly, at 8000 s, the results are: $\theta_{O_2} = 89.2$ %, $\theta_{O_2} = 10.7$ %, and $\theta_{H_2O} = 0.1$ %. This behavior is consistent with the case of two competing species since NO_3 is not a significant atmospheric constituent. This analysis also shows that water remains a dominant desorbing agent for longer timescales, giving additional confirmation that $\tau_{NO_3} \approx$ 2575 s ± 326 s under standard atmospheric conditions.

4.3.2 Monitoring the 2D (G') Raman Mode

Raman spectroscopy was performed on functionalized devices to gather additional evidence of the timescales associated with the desorption process. After collecting a time series of Raman spectra, some examples of which are shown in Figure 4.6 (a), the 2D (G') mode frequencies were analyzed. The four example spectra were observed at four distinct time's are labeled t_1

doi:10.6342/NTU202210171

through t_4 and correspond to 0 s, 5×10^3 s, 10^4 s, and 1.2×10^4 s, respectively. To extract the frequency, the peaks at all these times were fit to a Lorentzian profile. The fitting results are shown in Figure 4.6 (c) as black data points. The peak fitting procedure gives out errors which are indicated using the error bars denoting a 1σ error. We now need to determine the relationship between the 2D mode frequency and the n_h. We performed two types of analyses to understand this relationship.

The first analysis involved using existing literature to calculate an expected behavior of the 2D mode frequency with time. To do this, we used a best-fit cubic curve which we extracted from Ref.[92], in this thesis, it is shown by the inset of Figure 4.6 (b). This curve relating 2D mode frequency to the Fermi energy was recalculated to show the relationship between the 2D mode frequency and n_h by using$E_F = \hbar v_F \sqrt{\pi |n_h|} sign(n_h)$. For the purpose of recalculation, we used two known conditions- the first that n_h was determined by electrical transport and was predictable (about 1.1×10^{12} cm^{-2}), and the second was that the n_h could be approximated at the minimum wavenumber as corresponding to the Dirac point, according to the results of Figure 4.6 (c). Using this recalculation, average time-dependent n_h curves were transformed to calculate a predicted Raman peak shifting (gold) based on τ_{NO_3} in Figure 4.6 (c). The dashed cyan curves are repeated calculations based on different time constants to show the extent of the prediction accuracy.

doi:10.6342/NTU202210171

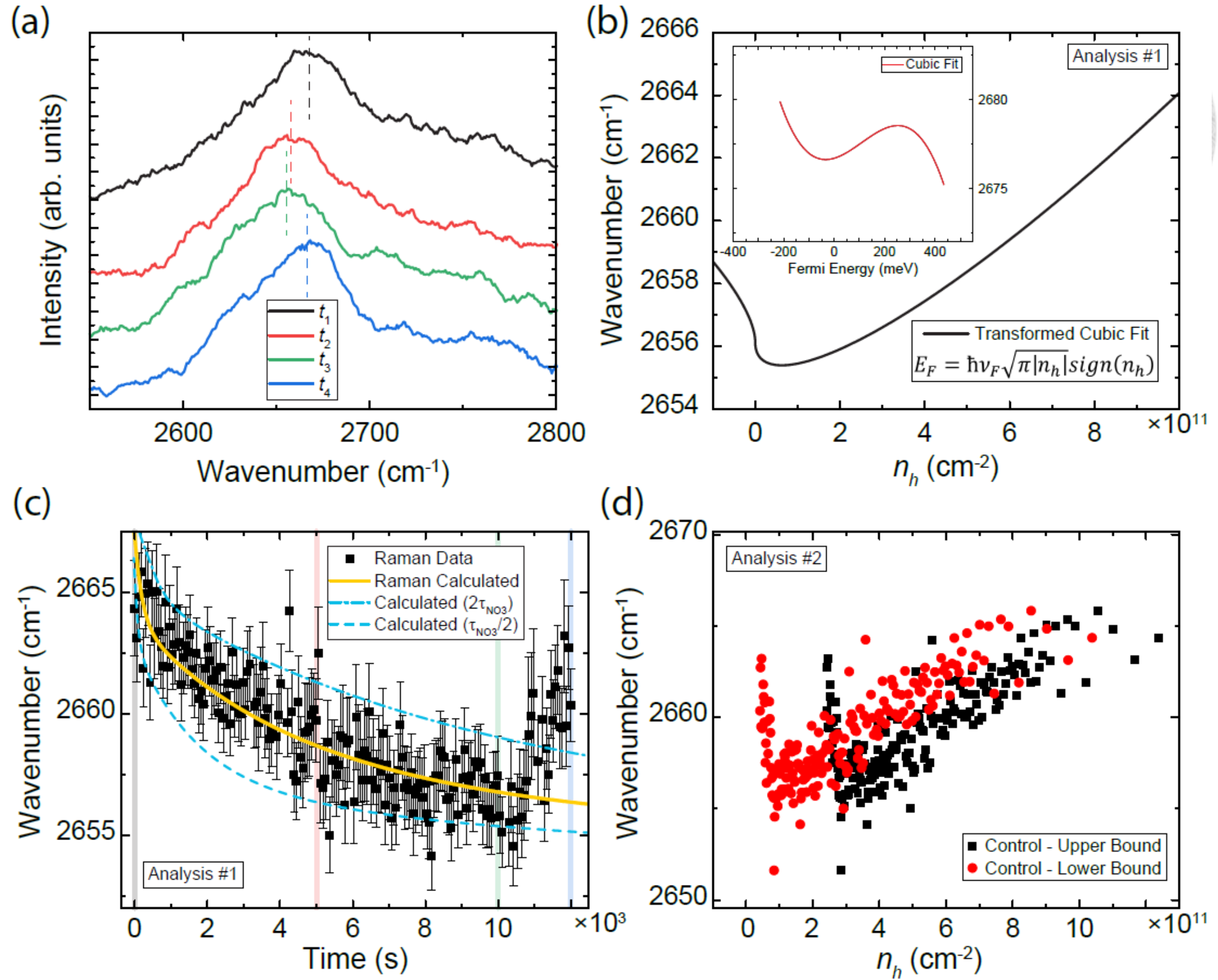

Figure. 4.6. Spectroscopic verification of observed time constants. *(a) Raman spectra for the 2D (G') mode of EG shown as an example. The four distinct times for which these spectra are observed are labelled as t_1 through t_4 and correspond to 0 s, 5×10^3 s, 10^4 s, and 1.2×10^4 s, respectively. (b)A best-fit cubic curve is extracted from Ref.[91] and used to calculate the relationship between the n_h and the 2D mode frequency. (Inset: the 2D mode frequency as a function of Fermi energy) For this analysis, the transformation is given two initial conditions: (1) n_h is known and (2) n_h is known at the minimum wavenumber (corresponding to the Dirac point). (c) A plot of the 2D mode frequencies for the time series measurements (error bars from the peak fitting procedure indicating 1σ error). Raman peak shifting trends are calculated and plotted in cyan (dashed) and gold (solid), based on the relevant time constant. The times listed in (a) are marked by four thin color-matched bands. (d) The relationship between the n_h and 2D mode frequency as extracted from the data directly is revealed through a second analysis. The mode's doping-dependence shows a reasonable behavior compared to the literature*.

doi:10.6342/NTU202210171

Before going to the second analysis, we must note that the prediction of the Raman trend (gold curve) is a simple transformation that gives a 1:1 correspondence between n_h and the 2D mode frequency. The change in polarity of the charge carrier may be the reason for the immediate rise in wavenumber that occurs after the minimum. It is a reasonable behavior considering that a similar trend can be seen in Figure 4.6 (b) as one considers crossing the Dirac point to obtain an electron density (or below $n_h \approx 0$ cm^{-2}).

For the second analysis, we decided to not use any of the predictions from the past literature. So in this approach, we can use the time-dependent n_h curve as a direct way to find the relationship between the 2D mode frequency and n_h. When compared to literature, the mode's doping-dependence, as seen in Figure 4.6 (d) for an example control device, shows a reasonable behavior [92, 93]. The major issue that arises from this approach is that the wavenumber extrema appears to occur at some arbitrary positive value of n_h. This kind of a departure from the calculation in Figure 4.6 (b) shows that, especially for devices with more variation in n_h, an unexplainable minimum can arise in the final transformed data. With this in mind, some of the error can be accounted for by introducing a rigorous horizontal error bar, however, this would ultimately reduce the predictive quality between a device's hole doping and its 2D mode frequency .

4.4 Illustration of dopant interaction

Theoretical calculations show that NO_2 is a stronger acceptor of electrons than H_2O by about a factor of 4 [94]. And given the relative similarity of H_2O and O_2 as acceptors on EG (when comparing their adsorption times and energies) [85-88], it is not unreasonable to posit NO_2 being a similarly strong acceptor when compared to O_2. Furthermore, the radicals NO_2 and NO_3 are calculated to be of similar strength in terms of electron transfer from EG [62]. On a similar note, some works report on the influence of hydrocarbons when discussing desorption or adsorption processes on graphene [95]. It should be noted that under most conditions, if a molecule does not exert a partial pressure in the total volume of its environment, it will desorb. That said, the case of

doi:10.6342/NTU202210171

Ref. [95] offers an interesting point for graphene grown by chemical vapor deposition, where it observes a signature of CH_2 in a spectrum taken with Fourier transform infrared spectroscopy after 10 min in air. We posit that due to the growth technique, it is possible that the CVD graphene has been prone to adsorbing precursor material that may have lingered on the surface. The claim that EG is less likely to exhibit this behavior can be substantiated by other EG observations using FTIR, while noticing that the CH_2 signature no longer appears [96].

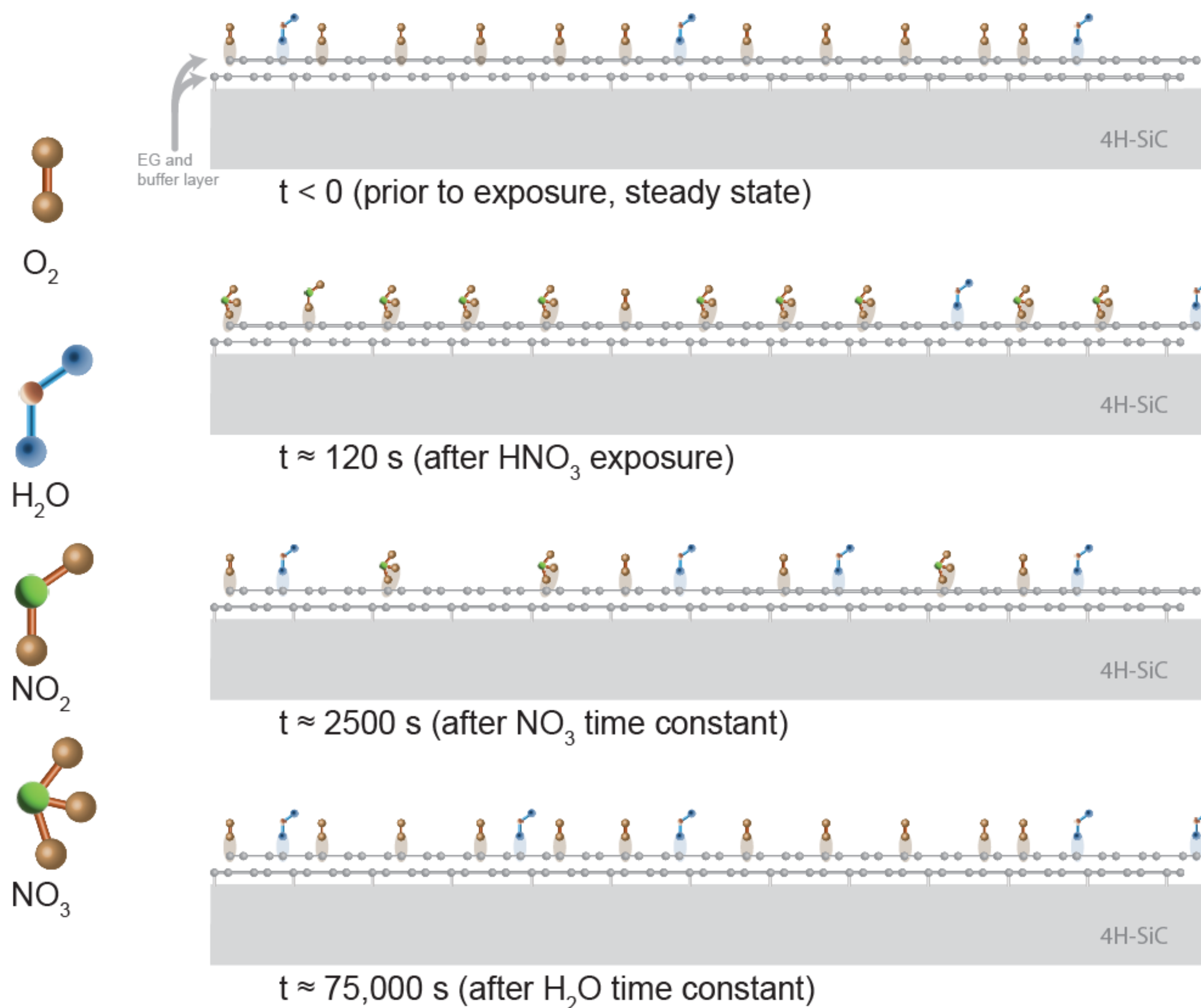

***Figure 4.7: Illustrations of dopant interactions**. Illustrations of possible configurations of surface coverage are provided here at various points of the desorption process. This figure is meant to guide intuition and is not a precise rendering or scaling of the system.*

doi:10.6342/NTU202210171

Chapter 5 Current Distribution in graphene quantum Hall devices

In this chapter, we investigate the mesoscopic nature of current flow in multiple-series circuits using single graphene Hall bar structures with less than 10 μm spacing between the side-contact voltage probes, some of which carry current in our measurements. To recap, quasi-one-dimensional edge channels are used in the Landauer-Büttiker description of edge/bulk equilibration with current flowing into the contacts along the edges of the quantized Hall device. Diamagnetic edge currents [97] do have an essential role in the theoretical description of the quantized Hall effect. However, scanning probe measurements [98] have shown that the edge-channel picture is not universally correct for larger currents in metrolrogical quantized devices. A more descriptive physical picture is provided by incompressible electronic regions in the bulk of the device channel. Incompressible regions that form between the source and drain are populated by carriers that maintain dissipationless current and these extended states enable current drift powered by the Hall potential. In this picture, when carriers are driven by electrochemical forces, a current flows with near-zero longitudinal resistance by following the incompressible strips, subject to the internal and external fields, device inhomogeneity, and edge potentials. Informative reviews of QHR device characteristics with extended states are found in Cage [48] and Jeckelmann, *et al.* [49].

Nonequilibrium electrons injected at the contacts must approach thermal equilibrium to coalesce into incompressible quantized states. For high current flow at a contact, the rate of electron cooling depends on phonon interactions in the surrounding media, including the substrate and cryogenic bath, as well as cyclotron emission rates. A study of the two-dimensional electron gas (2DEG) electrons near current contacts in S-MOSFETs has shown that hot electrons emit acoustic phonons at the cyclotron energy, and that cyclotron emission peaks when the bulk of the 2DEG is in the dissipationless QHR state [51]. Similar effects are reported in GaAs/AlGaAs heterostructures [50]. In semiconductor QHR devices the Landau level (LL) energy separations

doi:10.6342/NTU202210171

are constant, and thus the cyclotron emission signal is more distinct than in graphene, where the LL energies increase only as the square root of the electron energy [99].

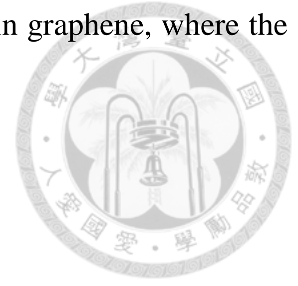

5.1 Device description

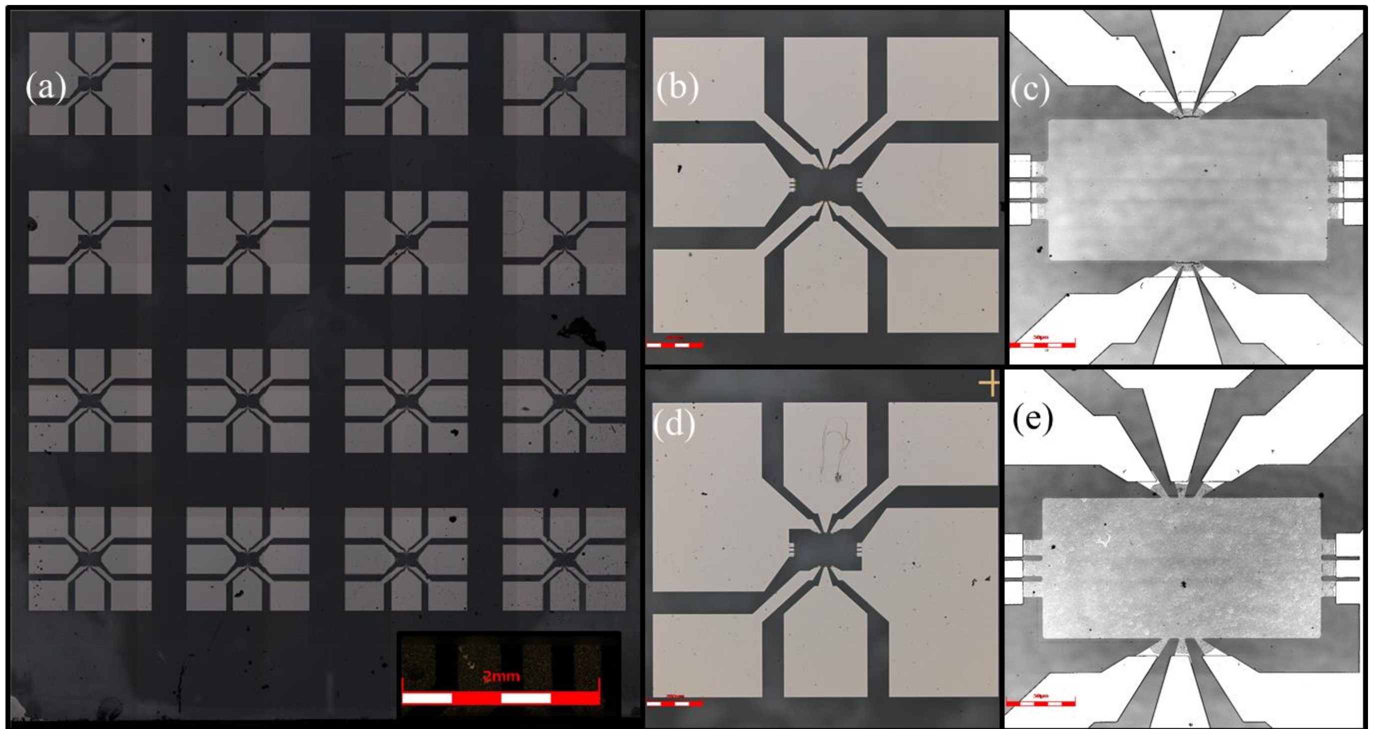

Figure 5.1: Current distribution device designs. *(a) A chip with 16 devices. Devices were labelled from the top left as D1, D2,…to D16 at bottom right corner. Top two rows are made with identical 6 contact devices, starting from the left, the spacing between its Hall contacts varies from 1μm, 3 μm, 5 μm, 7 μm. The bottom two rows are 8 contact devices with a similar spacing. (b) a close up image of the 8 contact device. (c) CLSM image showcasing the graphene quality of the 8-contact device. (d) a close up image of the 6-contact device. (e) CLSM image of the graphene for that device.*

Figure 5.1 shows details of contact design for the four devices we study in this report. The chip has a total of 16 devices. The devices are labelled as D1 to D4 from left to right in the top

doi:10.6342/NTU202210171

row, and as D5 to D8 in the second row and so on. The top two rows are 6 contact devices, a representative image for which is shown in figure 5.1(d). The bottom two rows are 8 contact devices, a representative image for the same can be seen in figure 5.1(b). In all devices, six side contacts are equally spaced about the midpoints of the 200 μm sides of the Hall bars, and source and drain contacts are centered on the ends of width 100 μm. The source, carries the full energizing current for all electrical measurements. The source and drain (S/D) are symmetric, and each consists of three well-separated branches to the epitaxial graphene channel region. In addition to these three branches, the S/D metallization of the devices labeled D6 and D7 (Fig. 5.1 (d,e)) extends to the closest of the side contacts on diagonally symmetric sides. These contact branches carry negligible current for field direction $B+$ but ensure that the relevant source or drain electrochemical potential is maintained at that contact point. Separate contact pads allow electrical access to the remaining two contacts on each side of D6 and D7, and likewise to all six of the side contacts on D10 and D11 shown in figure 5.1 (b, c) respectively.

The two types of devices were constructed to produce somewhat different electrochemical environments near the side contacts. The three-way split-contact design of the source and drain reduces the potential difference between these metallic contacts and the fully quantized QHR electrochemical potential to a negligible level, even when a HS forms. Based on the charge polarity (electrons) in our devices and the selected direction of perpendicular magnetic field ($B+$), the channel current enters or leaves the quantized 2DEG predominantly at the lower corner of the source (left) and upper corner of the drain (right) contact. This current produces an electrochemical potential along the edges, which is close to the potential at other contacts that are used in the multiple-series connections. The multiple-series circuit concept is thus enabled by the quantized Hall effect where the longitudinal resistance is negligible. Compared to resistive devices, greatly reduced current enters through the secondary branched contact points due to the absence of any appreciable potential difference at the contact/2DEG boundary, particularly at the farthest contact from the HS corner. The three voltage probes are situated ≈ 100 μm distant from the source and drain. Unbranched contacts were used in the design of the devices to allow widths of only 4 μm in all side contacts where they meet the main channel. The distance between voltage contact centers were 6 μm (D6, D10) and 10 μm (D7, D11).

doi:10.6342/NTU202210171

5.2 Contact and Longitudinal resistance

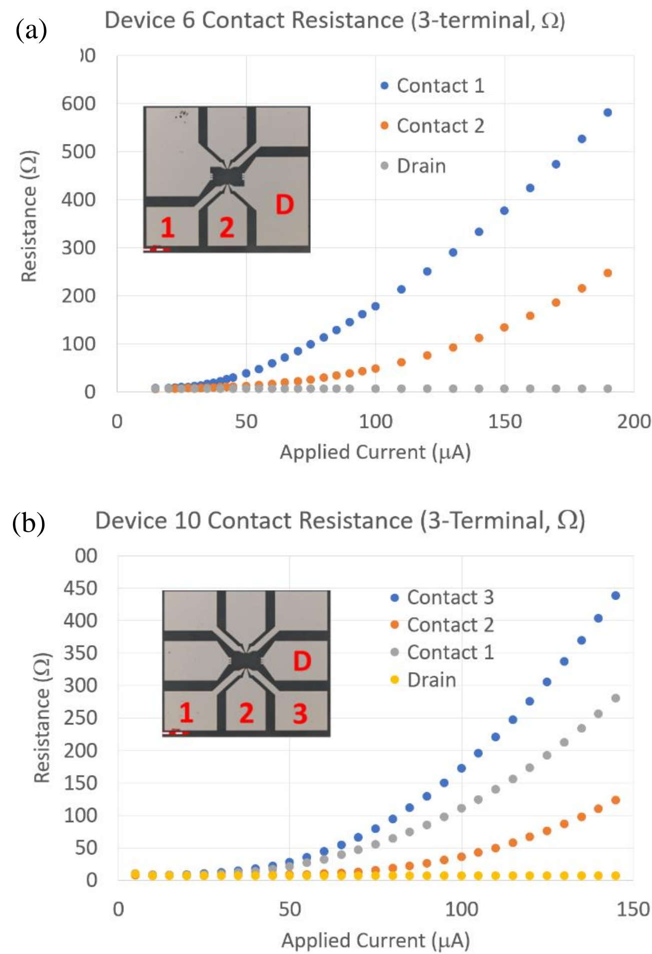

Figure 5.2: Contact resistance as a function of the applied current. *Contact resistance scaling for a 6-contact device- D6 (a) and an 8-contact device D10 (b). Insets show the assigned contact layout.*

Variable dc current levels were applied between the source and each of the isolated side contacts to measure three-terminal contact resistance with the devices at ≈ 2 K and 9 T perpendicular magnetic field. Voltage was measured between the drain and the same side contact for positive and negative current directions. The S/D contact resistance values were measured similarly, with negligible longitudinal resistance along the direction of current flow. We selected

doi:10.6342/NTU202210171

the four devices for this work to have below 1 Ω contact resistance at low current in all side contacts on at least one side of each device.

Any effect of contact resistance between the metal layer and the graphene can be effectively eliminated using multiple contact branches, as can the effect of HS resistance that develops due to heating at higher currents. For example, the contact resistance data shown in Figure 5.2(a, b) shows no increase for the drain, and is equal to the known resistance in the cryostat leads of ≈ 7 Ω.

At currents above about 25 μA to 50 μA the side-contacts begin to show higher resistance with increasing current. This corresponds to about 10 μA/μm of contact width. Experiments with exfoliated graphene on SiO_2 have indicated that breakdown occurs beginning at current densities of ≈ 8 μA/mm for samples of small width [100]. As described later, contact resistance and current distribution give similar values for the current at which internal resistance begins to increase.

If we consider a graphene film 1 mm square adjacent to the contact, 6×10^{13} electrons must enter and leave each second to maintain a current of 10 μA/mm. For ballistic motion, electrons travelling at the Fermi velocity (≈ 1.05×10^6 m/s) could cross the square in 1 ps, but the magnetic field of 9 T induces cyclotron motion. Thus, multiple scattering events must occur close to the contact. This helps to understand how the hot spot region appears at higher currents within the graphene layer itself and indicates that a radial electric field develops due to the excess of carriers within the hot spot region near the contact.

We derived the longitudinal resistance (R_{xx}) values over a wide current range from a series of fixed digital dc currents (I) applied at the S/D contacts. Longitudinal voltages were measured with a precision nanovolt meter and results for opposite current polarities were combined to yield the resistance. Typical results are shown for two adjacent side contacts of device D10 in Figure 5.3. Each of the four devices exhibited R_{xx} values consistent with full quantization for S/D currents of 150 μA or higher.

For low and moderate bulk current levels, the current I that passes the voltage probes will result in an orthogonal Hall voltage given by IR_K/n, where $n = 2$ is the Landau level index of the QHR state in our measurements. Where sets of orthogonal contacts with low contact resistance were present, we made Hall resistance measurements using an automated digital bridge with

doi:10.6342/NTU202210171

roughly 5 × 10^{-8} uncertainty. For device D11, both diagonal and orthogonal measurements were possible, and the longitudinal resistance was derived.

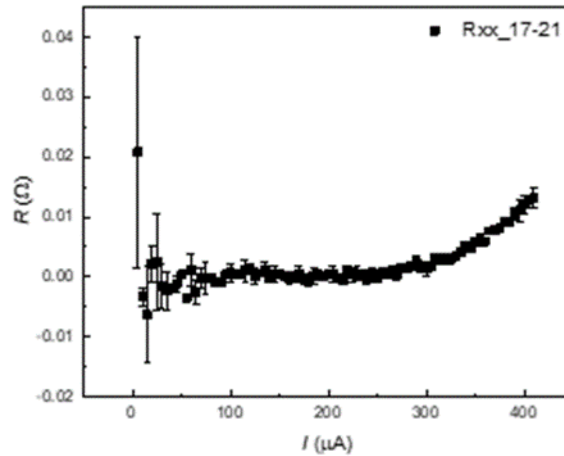

Figure 5.3: Longitudinal resistance as a function of current. *The longitudinal resistance measured at increasing currents in the adjacent contact.*

5.3 Current Distribution

While current enters the device at the source contact, we investigate various external circuits that allow current to pass through one or more side contacts that share connections to the drain, or that can serve as the drain. Understanding HS proximity effects may lead to better QHR array designs, with efficient heat dissipation at higher current and voltage levels. Placement of the side contacts close to the source and drain could allow more freedom in designing large arrays. In this study the source and drain are placed at the metrologically tested distance of one square (here, a 100 μm square) from the side contacts. The side contacts shown in Figure. 5.1 have equal widths of ≈ 4 μm where they meet the main channel. The widths of the insulating gaps between these contacts are ≈ 2 μm for devices D6 and D10 and ≈ 5 μm for D7 and D11.

The circuits of Figure 5.4(a,b) are examples of our modified double-series (2-series) arrangement, where the drain contact is disconnected and upstream and downstream side contacts are connected to the current source low output for current measurements. All triple-series (3-Series)

doi:10.6342/NTU202210171

measurements include an external room-temperature resistor of value 12906.4 Ω in series with the drain lead (not pictured) and connected to the current source low. For both 2-series and 3-series measurements, a 1 kΩ resistor in series with an upstream side contact diverts some fraction of the current to enter the device at a downstream contact. The currents measured in the final, downstream contact are compared to the values calculated from Jeffery's analysis [48] for 2-series and 3-series circuits.

For a QHR device quantized on the ν = 2 plateau and with four-terminal resistance R_K/n = 12906.4037 Ω, the fraction of the total current I_T diverted to the downstream side contact in the 2-series circuit is given by the following equation,

$$I_n = I_T R_m/(R_K/2 + R_m + R_n)$$

Here I_T is the total current in the two branches and (m,n) represent the positions of the upstream and downstream contacts, respectively. In each connection the resistance includes the resistance external to the device and the contact resistance, which may change with In Figure 5.5(a-d) we plot the currents I_n measured for the downstream contacts as the current in the upstream contact (I_m, also measured) vary. This allows us to compare the 2-series and 3-series results with equal current flowing in the upstream contact. Not surprisingly, the above equation can be used to calculate the downstream current if the upstream contact current and resistance parameters are known, even for the 3-series data. An extrapolated nominal current value is calculated and plotted using the 3-terminal contact resistance measurements for currents of 5 μA to 15 μA, where HS resistance is negligible.

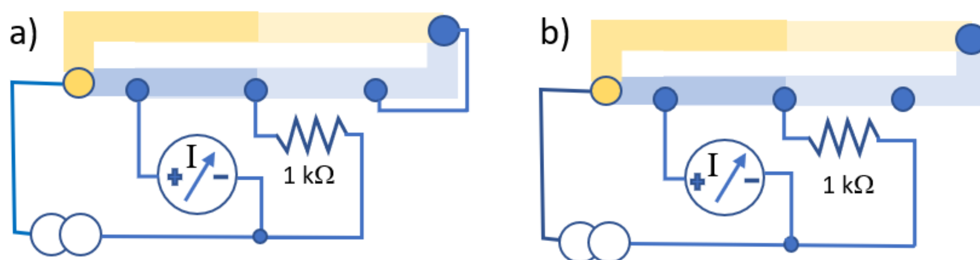

*Figure 5.4: Circuit diagrams for **the double series arrangement**, (a) devices D6 and D7 include a permanent conducting path on-chip between the drain (large blue dot) and the nearest side contact. (b) For devices D10 and D11, all side contacts have external bonding pads.*

doi:10.6342/NTU202210171

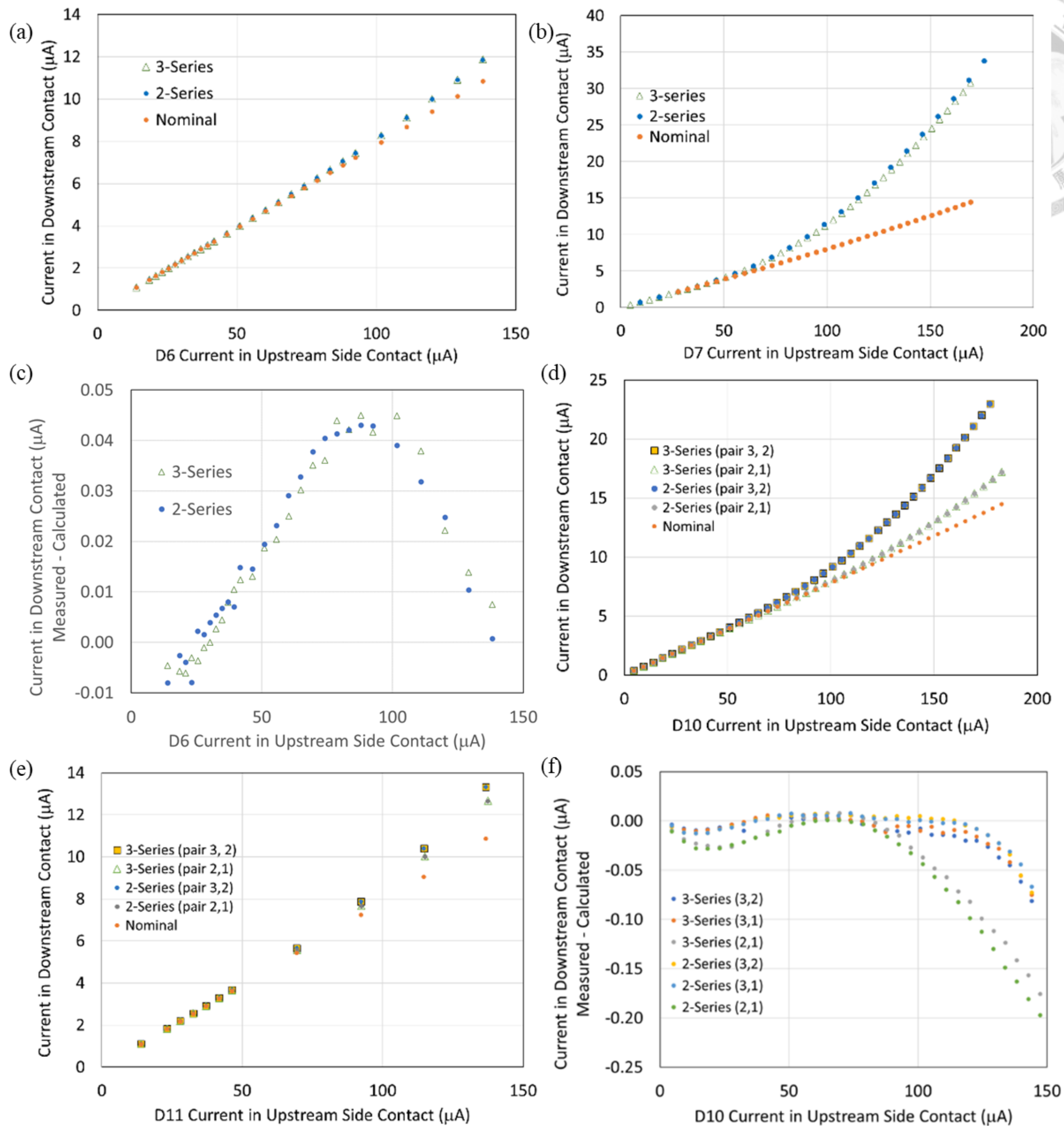

Figure 5.5: Measured currents in multi-series circuits. *Measured current for devices (a) D6, (b) D10, (c) D7, and (d) D11. The two-series and 3-series contact pairs are labeled (3,2) and (2,1) with the indices in the parenthesis corresponding to numbering in Fig. 5.2 (b). Results for the pair (3,1) are not shown because they are nearly identical to those for (3,2). This result can be explained by the direct dependance in the series equation in Chapter 2, on the resistance of the common upstream contact (3). Second-order polynomial fits to measured three-terminal contact resistance were used to calculate predicted currents, and these predicted values are subtracted from the measured values from a) and b). Results are plotted in (e) and (f) for D6 and D10.*

doi:10.6342/NTU202210171

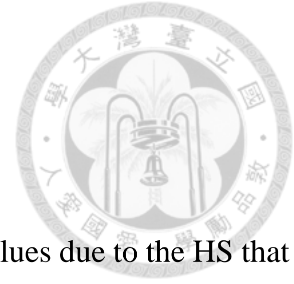

The measured current in figure 5.5(a-d) differs from the nominal values due to the HS that develops when the current in the upstream side contact exceeds ≈ 40 μA. We show the measured current for the contact pair (3,2) in figure 5.5(c,d) and data for (3,1) is omitted because it is indistinguishable at this scale. This is the first of several interesting results. The dependence of the previous equation on the downstream series resistance r_n is weak since this value appears only in the denominator, together with $R_K/2$, but our data is the first to test the circuit model with the present conditions of small contact separations and high current.

The 3-Series data, where the total current in the devices is twice as large, are very similar to the 2-series data in Figure 5.5(a-d) for all four devices. In the D7 and D10 results, the 2-Series current is slightly higher, and the HS resistance is also higher as shown by the larger increase in the current levels. For D6 and D11 the results are nearly identical. This HS resistance has little effect on the measured share of current for the drain contact, which is 49.99% at I_T = 30 μA and 49.98% at I_T = 400 μA for device D7.

It is straightforward to calculate the expected currents using the measured contact resistances. We use second-order polynomial fits to the contact resistance data shown in Figure 5.2, limited to the current range above 40 μA which minimizes the residual error. Substituting these resistance values calculated at the appropriate current levels yields results in good agreement with the measured data as shown in figure 5(e,f) for devices D6 and D10. This indicates that the HS resistance is equivalent when sampled in these circuits and is well-represented as a component of the contact resistance our figure 5.5 data

Finally, in Figure 5.6 we present measurements of R_{xx} values like those in the last section, except here the 2-series connection is made at the contact immediately downstream of the sampled region, and due to $R_K/2$ external resistance in the drain connection the current is divided evenly between drain and furthest side contact. Values of the Hall resistance deviation $\Delta R_{xy} = R_{xy} - R_K/2$ are plotted from precision DCC bridge measurements made with S/D current only, and no 2-series

doi:10.6342/NTU202210171

connection. These separate measurements show excellent agreement with the expected linear dependence given by $\Delta R_{xy} = sR_{xx}$ with $s \approx 0.26$.

In the region near the HS, a region exists where the downstream electrochemical potential increases well above that of the upstream contacts, and if the spatial extent of the HS is larger than the separation of the side contacts one might expect to see an effect on R_{xx}. For example, energetic electrons could encounter the downstream corner of a nearby metallic contact and lose energy by exiting at the upstream corner. As shown by the contact geometry in Figure. 5.1, the metalized contacts are recessed by ≈ 10 μm from the channel boundary and this likely prevents such dynamic events.

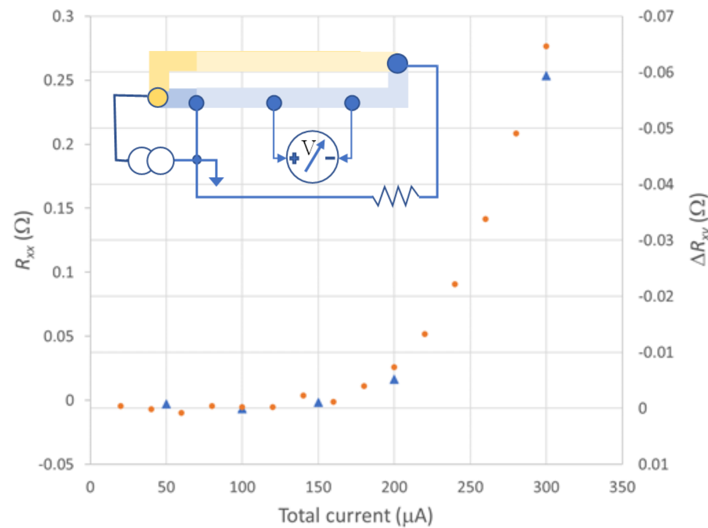

Figure 5.6: Longitudinal resistance in a double series connection compared with the deviation in Hall resistance. *R_{xx} measurements made with a double series connection immediately downstream. Compared with the deviation in Hall resistance without a double series connection, showing excellent agreement.*

doi:10.6342/NTU202210171

Chapter 6 Versatility of uniformly doped graphene quantum Hall arrays in series

In this chapter, we demonstrate a device design that confirms the concept having an array of EG based QHR devices capable of giving outputs of quantized resistance values starting from the standard value of $R_k/2$ of around 12.9 kΩ and going up to more than three orders of magnitude to around 1.29 MΩ, which is equal to a 100 QHR devices in series. Several different experimental methods are used to check the versatility and quality of the devices. These include standard lock-in techniques, CLSM imaging, precision measurements, and Raman spectroscopy. To be successfully implemented in practical applications as standards, these devices must show resistances that are well-quantized [16, 49, 101-104]. The $v = 2$ Landau level which forms the resistance plateau of $\frac{1}{2}\frac{h}{e^2} = \frac{1}{2}R_{\mathrm{K}} \approx 12906.4037\ \Omega$, where h is the Planck constant and e is the elementary charge, has been adapted as a standard for graphene-based resistances as explained in the introduction. Efforts also continue to implement the similar functions for the $v = 6$ plateau [105].

For metrological purposes of expanding the available quantized resistances, EG based standards have been a focus of fabrication. The unit of Ohm has recently been redefined by the International System of Units (SI). Historically, a single value of the QHE from the $v = 2$ LL has been used to derive the value of Ohm. This restricts the infrastructure and tools which are required to disseminate or use this unit of Ohm. This increases the value of the efforts to access new values of resistances for electrical standards. So far, there have been various attempts at demonstrating multiple Hall bars in series, parallel, or in *p-n* junction form to access quantized resistance values of qR_K, where q is a positive rational number. [46, 47, 68, 70, 106-110]. Many factors limit the development of these standards, like, the quality and the coverage of the as-grown EG, and the restriction on devices outputting one value (even though it may be a part of a set, eg: qR_K) [111, 112]. Hence, to improve the global dissemination of the ohm, there is a need to demonstrate devices that could output more than one values as resistance standards.

doi:10.6342/NTU202210171

6.1 Device description

The device design is illustrated in Fig. 6.1 (a) along with the corresponding CLSM images for two distinct array elements in Fig. 6.1 (b) and (c). Each individual array element works as a standard 12.9 kΩ Hall bar having a split-contact design that optimizes the current flow and eliminates the effect of the contact resistances [46, 58]. The CLSM image shows the contrast of a smooth layer of EG confirming its high quality. The 51st element of the array is designed for the purpose of serving as a troubleshooting tool in the event that the complete array is not well quantized. One may connect that device and measure each half of the array independently to diagnose the source of poor quantization. The large contact pads at the end of every row of 10 elements functions as a tool to access quantized values of multiples from 129 kΩ, up to as large as 1.29 MΩ. A summary of these values is shown in Fig. 6.1 (a).

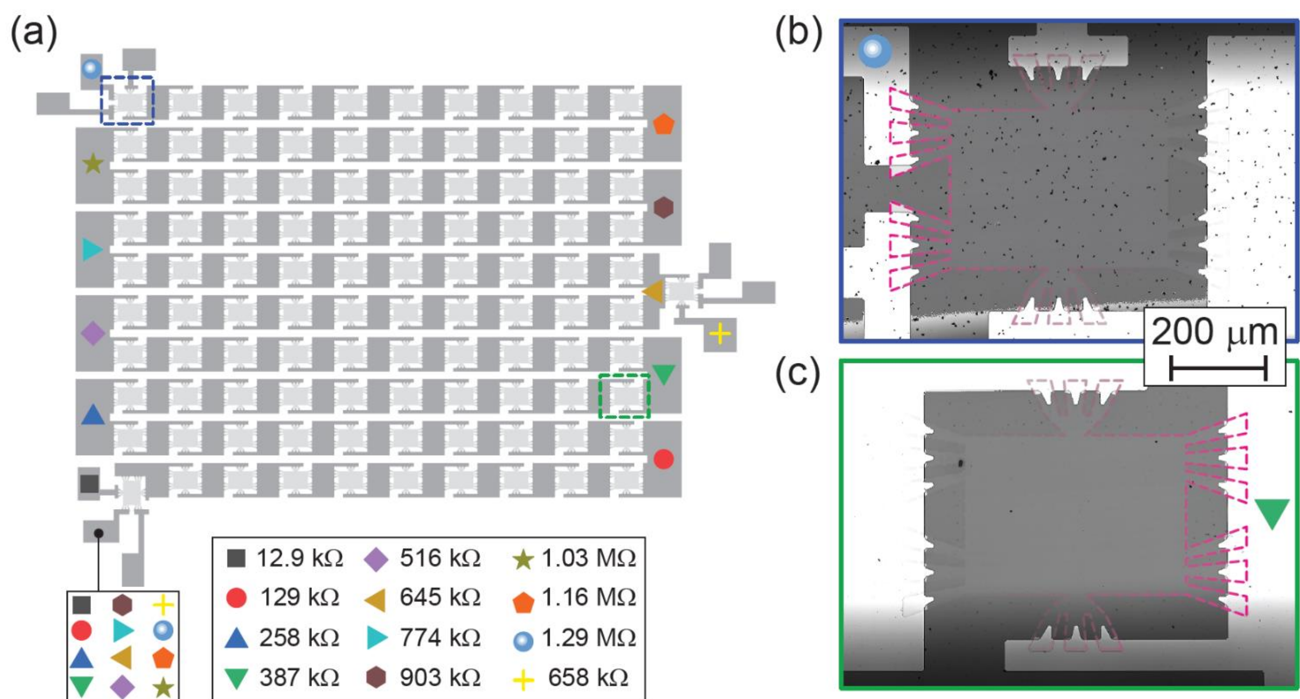

doi:10.6342/NTU202210171

Figure. 6.1:1.29 MΩ Array (a) An illustration of the 1.29 MΩ Hall array device with points denoting the measurement locations that give us the multiple values of the quantized Hall resistance. Dashed green and blue lines outline two example areas which were inspected by CLSM. (b) and (c) Show the two inspected elements which reveal a uniform growth of EG over that area. A magenta line overlaid over the EG area shows the boundary of the Hall elements. The black debris that is visible over the devices is a byproduct of the $Cr(CO)_3$ functionalization, and it does not interact with the graphene in any way other than doping it as described in the earlier sections.

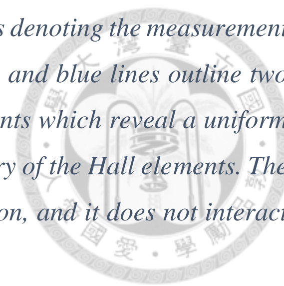

6.2 Raman Spectra

Flaws in the physical properties of the as grown EG layer are not always identified visually. A tool like Raman spectroscopy is used to confirm the uniformity of the EG film across the the centimeter scale growth. A Renishaw InVia micro-Raman spectrometer was used for such measurements with an excitation laser source of 633 nm wavelength. A 300 s acquisition time, 1 mW power, 1 µm spot size, 50 × objective, and a 1200 mm^{-1} grating was used to collect and measure the spectra using a backscattering configuration. Rectangular Raman maps with step sizes of 1 µm in a 25 × 25 raster-style grid was collected and repeated on different elements of the array of devices in order to get some statistical data on the quality of the EG. Figure 6.2 shows a summary of the Raman analysis. Two elements separated by a maximum distance are inspected closely, these devices are marked figure 6.2 (a). A 2D (G') mode from the Raman spectrum is shown as an example in figure 6.2 (b). It is used as the primary metric to compare the EG quality. The D and G peaks are not selected because the strong optical responses from the SiC substrate obscures the signals.

doi:10.6342/NTU202210171

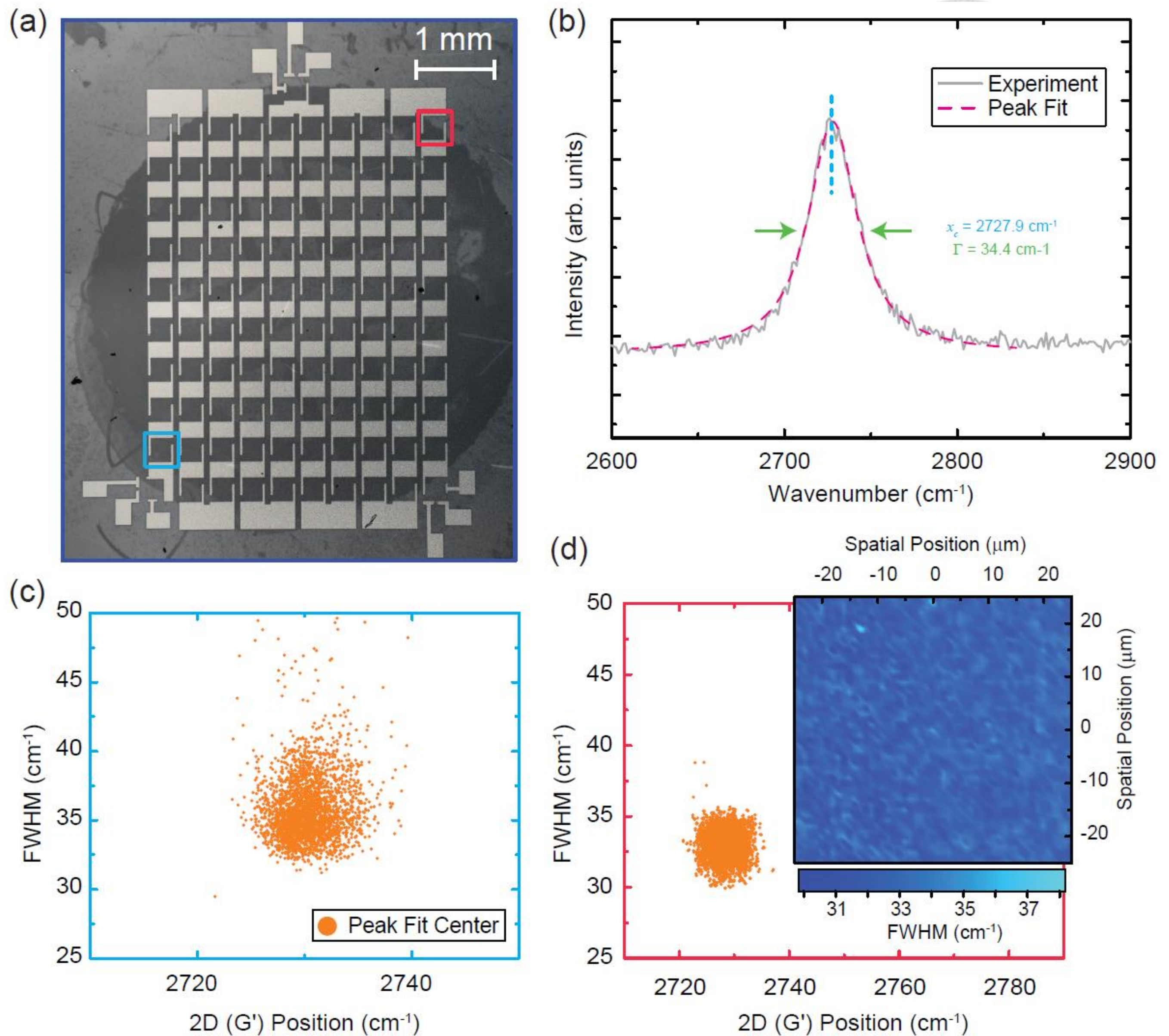

***Figure 6.2: Raman analysis of the 1.29 MΩ Array**. (a) An optical image of the complete array where the red and cyan regions indicate the two example elements whose Raman maps are shown in (c) and (d). (b)A Raman spectrum focusing on the 2D mode of EG is shown. The D and G modes have signals that are obscured because of the strong optical response from the transparent SiC substrate. An example Raman spectrum focuses on the 2D (G') mode of graphene since the D and G modes have signals that are overwhelming by neighboring optical responses from the SiC substrate. To extract the FWHM and peak center, Lorentzian profile is used to fit each measured peak. (c) A closer inspection of the array element outlined in (a) in cyan. The scatterplot shows the FWHM distribution with 2D mode peak centers. (d) The analysis is repeated for the red outlined element in (a). In addition to these scatter plots, to verify the uniformity of EG, a colored map of the position-dependent FWHM is shown.*

doi:10.6342/NTU202210171

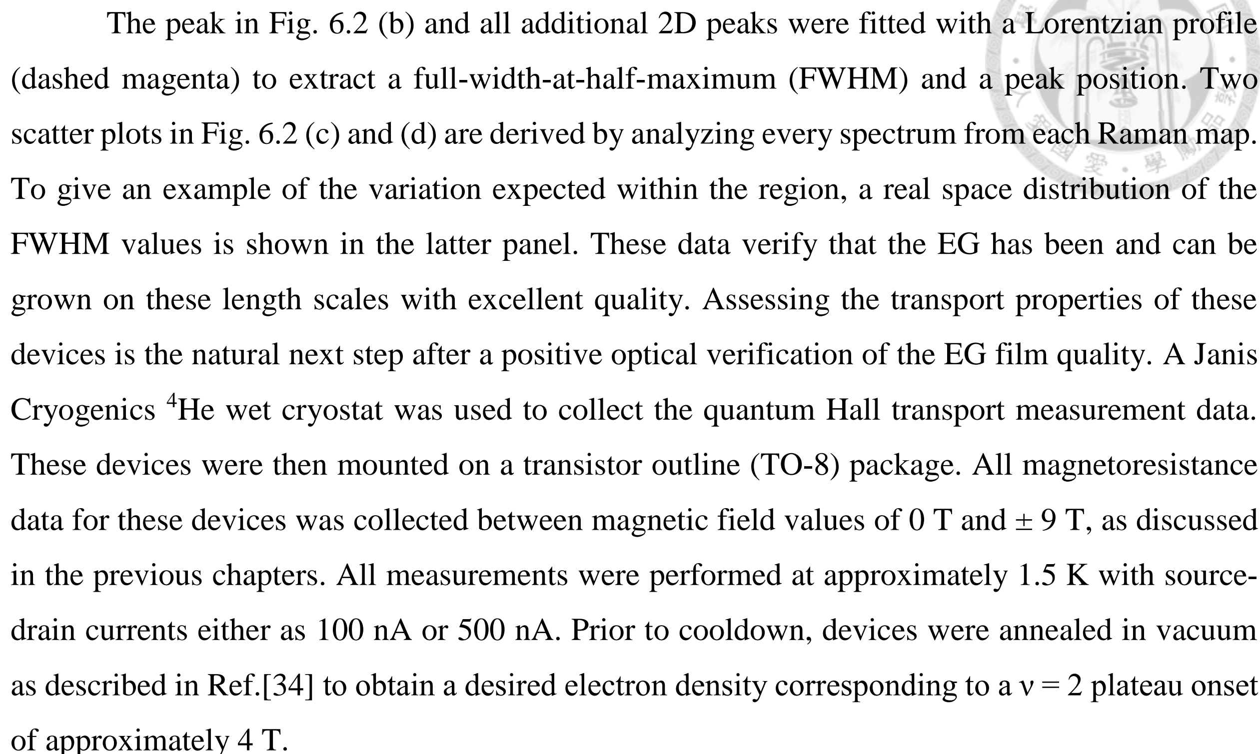

The peak in Fig. 6.2 (b) and all additional 2D peaks were fitted with a Lorentzian profile (dashed magenta) to extract a full-width-at-half-maximum (FWHM) and a peak position. Two scatter plots in Fig. 6.2 (c) and (d) are derived by analyzing every spectrum from each Raman map. To give an example of the variation expected within the region, a real space distribution of the FWHM values is shown in the latter panel. These data verify that the EG has been and can be grown on these length scales with excellent quality. Assessing the transport properties of these devices is the natural next step after a positive optical verification of the EG film quality. A Janis Cryogenics ^{4}He wet cryostat was used to collect the quantum Hall transport measurement data. These devices were then mounted on a transistor outline (TO-8) package. All magnetoresistance data for these devices was collected between magnetic field values of 0 T and ± 9 T, as discussed in the previous chapters. All measurements were performed at approximately 1.5 K with source-drain currents either as 100 nA or 500 nA. Prior to cooldown, devices were annealed in vacuum as described in Ref.[34] to obtain a desired electron density corresponding to a $\nu = 2$ plateau onset of approximately 4 T.

6.3 Hall transport measurements

The data for the transport measurements is shown in Fig. 6.3 (a). Most allowable values were measured as according to the labels in Fig. 6.1. The contact pads meant for wirebonding, limit what values can be measured. Though we can bond many intermediate values within the array by allowing special contacts in the design, alternate designs are recommended since potential damage to one element along the array will split the array into two separate devices. Lock-in amplifier techniques were used to collect the magnetoresistances shown in Fig. 6.3. Although this technique provides the advantage of swift data collection and with higher magnetic field resolution, it does potentially introduce minor errors due to equipment impedance. Specifically, the SR-830 lock-in amplifier has an internal impedance of 10MΩ, which is just one magnitude larger than the device. The values of each plateau were verified more precisely with a digital multi-meter at sufficiently high magnetic field (greater than 5 T) to account for this error. A DC current from the

doi:10.6342/NTU202210171

Keithley 2612A was used for this purpose. Verification of these values to within a part in 10^6 (explained in section 6.4) allowed for the correction of these data via offset translation and are shown as a group in Fig. 6.3 (b).

The noise in each plateau from Fig. 6.3 being relatively symmetric for both polarities of the magnetic field may be attributed to the low currents injected into the device, it may also be due to the lock-in amplifier limitations. The noise due to low currents was minimized by simply increasing the current from 100 nA to 500 nA, as shown in Fig. 6.3 (c). This kind of a comparison is done to test these devices with the goal of making them compatible with the available metrological infrastructure, such as the CCC, eventually. That is also why the 51st element was designed in the array. In the next section, the 51st device serves as an additional verification that the whole array device is well quantized. We should however note that, although higher applied currents typically result in less noise and better compatibility with metrological equipment, after a certain a point, the excessive Joule heating at various hot spots within the quantum Hall array would cause the device to lose well quantized state, which would lead to an even larger error when measuring the plateau's values.

doi:10.6342/NTU202210171

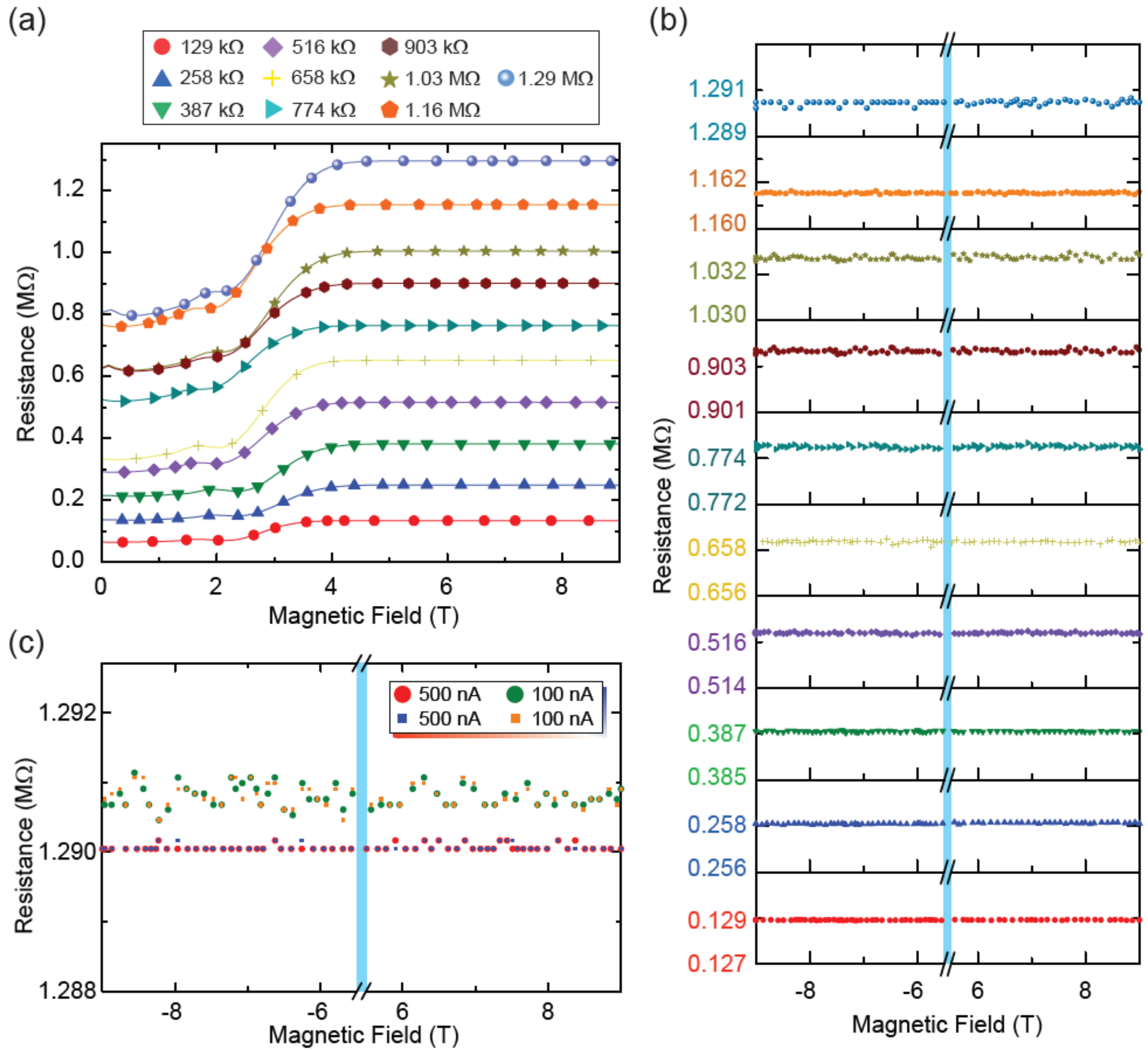

Figure 6.3: Hall data for 1.29 MΩ (a) A summary of the Hall transport measurements for each of the labels for measurements shown in figure 6.1. The magnetoresistance data was collected using lock-in amplifiers. This technique introduces some minor errors due to equipment's internal impedance. The value of each plateau was verified more precisely with a digital multimeter at sufficiently high magnetic field (greater than 5 T) to account for the error. DC currents from the Keithley 2612A were used for this purpose. Verification of these values to within a part in 10^6 using a CCC justifies the offset translation to correct these data. (b) A magnified view of each plateau shown at both polarities of the magnetic field demonstrates the noise level introduced by the lock-in amplifier technique. This noise

doi:10.6342/NTU202210171

was minimized, as shown in (c), by injecting a higher current, as is done there with the two currents of 100 nA and 500 nA.

6.4 Precision measurements

Half the array was precisely measured using a cryogenic current comparator (CCC) to validate its usage as a standard resistor. Figure 6.4 shows a collection of precision measurement data. Figure 6.4 (a) shows the deviation from the nominal value for two different pairs of contacts for the right half of the 100 device array. Recall that each terminal device has 3 contacts. One can be used to source current while the other two can be used to measure the voltage. The data is displayed for the right half of the array, i.e. measured between the 51st device and the 100th device. The fact that both pairs show a similar behaviour is a testament to the quality of the device. The maximum deviation from the nominal value of $51R_k/2$ is around 10ppm for lower currents. At low currents the signal is low and hence the CCC has trouble locking into the signal from the device, which is why we usually run it at higher currents. However, we want to avoid subjecting the array to higher voltages, hence we cannot apply higher currents. The deviation is low at around 5ppm for currents up to 5 μA, which is a great benchmark to be used as a standard resistor.

The figure 6.4 (b) shows the deviations from the nominal value for the left half of the array at different magnetic field strengths. We see that at higher currents, and different values of the magnetic field, the deviation is fairly close and consistent with values of around 20-30ppb and is of a superior quality compared to its right half. The differences in the quality for the right and left half arise from the different quality of coverage of the epitaxial graphene. The width of the terraces and the density of bilayer graphene is mildly inconsistent across a millimeter scale, which results in the different deviations for the array.

doi:10.6342/NTU202210171

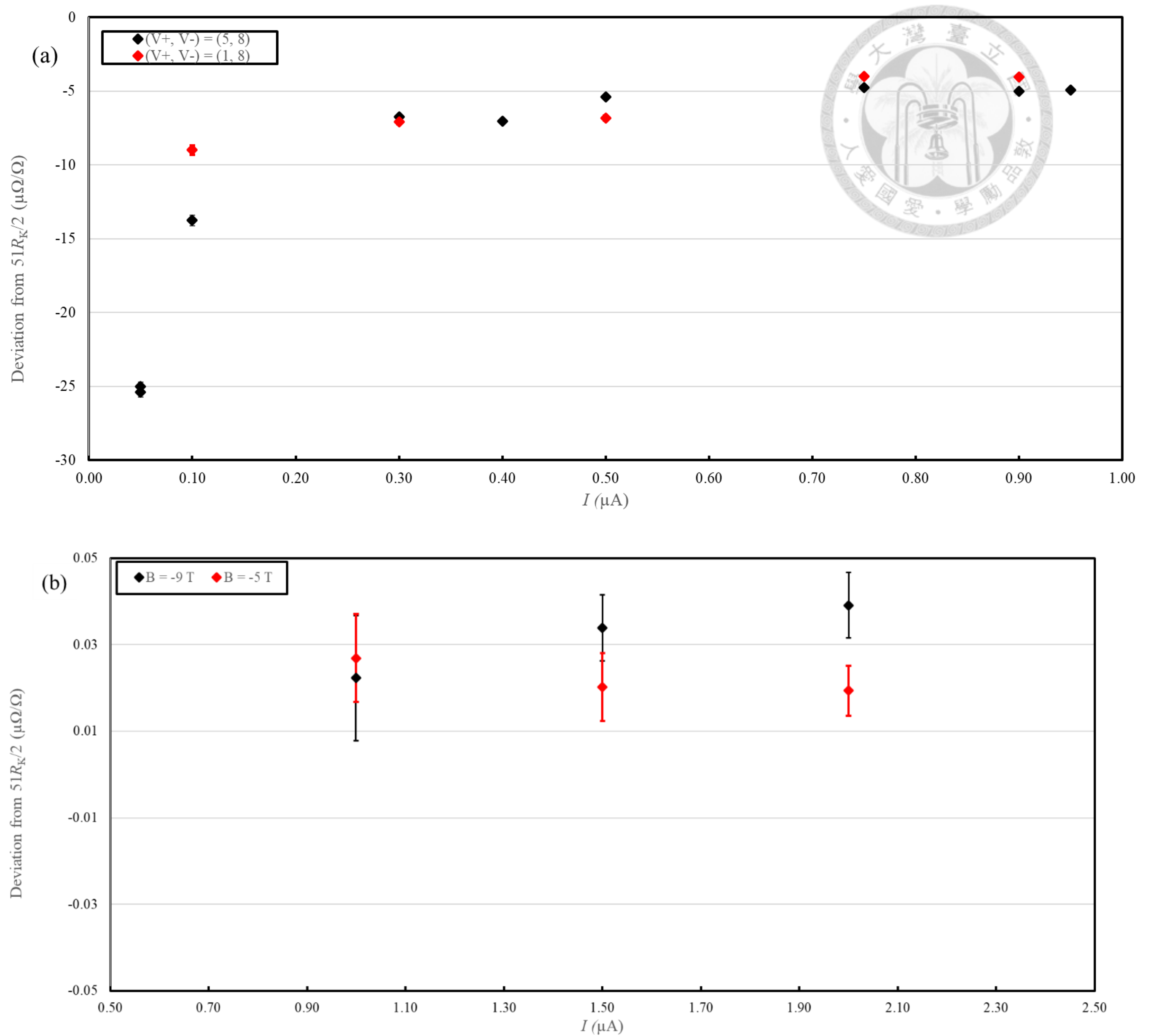

***Figure 6.4: Precision measurement data for each half of the array**. (a) Shows the deviation from the nominal value of Rk/2 for different current values compared using two different voltage terminals for the right half of the array. (b) Deviation from the nominal value as at different magnetic fields for the left half of the array.*

doi:10.6342/NTU202210171

Chapter 7 Summary and Outlook

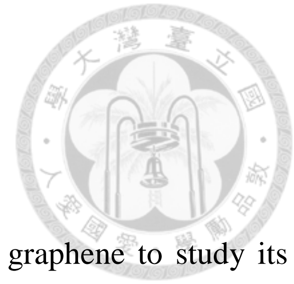

In this thesis, we have fabricated special devices using epitaxial graphene to study its electrical transport and charge carrier doping properties. These devices have improved our understanding of the desorption process when doping epitaxial graphene with nitric acid. We have pushed the limits of closely spaced contacts and proved their capabilities in the quantum Hall regime, paving the way for much smaller and densely packed EG QHR arrays. We have also demonstrated a proof of concept of a versatile QHR array for values ranging from 129 kΩ up to 1.29 MΩ. This chapter summarizes the results discussed in the core chapters of this thesis and provides an outlook for future experiments.

In Chapter 4, the dynamics of adsorption and desorption process after transient hole doping using nitric acid, are reported for the EG devices. A comparison of both as-grown EG and functionalized EG are reported. The timescales associated with the desorption using nitric acid are determined from the Hall transport and the electrical data at room and low temperatures of 1.5 K. Such an understanding of the gateless reversible hole doping is crucial for practical applications where the device dimensions restrict the fabrication of a metallic gate. The dynamics were further studied by monitoring the optical properties of the EG post exposure to nitric acid, using Raman spectroscopy techniques. The data from the Raman spectroscopy supports the determined NO_3 desorption time constants. These results provide a pathway for further devices where a need for p-type doping would arise without a feasible metallic gate.

In Chapter 5, we fabricated epitaxial graphene (EG) quantized Hall resistance (QHR) devices with closely spaced voltage-probe contacts and investigated the currents flowing in these contacts using double-series and triple-series circuits. Multi-series contact design can effectively eliminate interconnection errors only when the current branches behave as independent contacts and distribute current as described by Eq. 5.1. We find no deviations from Eq. 5.1 above 0.05 % at or below 100 µA in contacts of width ≈ 4 µm at separations of ≈ 2 µm as shown in Fig. 5.5. Another major conclusion from these results is that the interaction of large currents entering the devices from different points at wide spacing is minimal. The double-series and triple-series data

doi:10.6342/NTU202210171

shown in Fig. 5.5 and Fig. 5.6 argues in support of two related concepts: current entering a device at an upstream contact does not significantly influence the conditions that cause a HS to form at a downstream contact; and, the longitudinal resistance in a given region of the Hall bar depends on the current which enters upstream, and is not significantly changed by any large current which may enter downstream of the measured region.

In Chapter 6, for developing quantum Hall arrays, the boundaries for limiting factors were pushed to a point that several orders of magnitude of measurable quantized resistances could be realized. This milestone was possible due to a combination of high-quality material growth at the centimeter scale, and the implementation of superconducting contacts. Specifically, the standard Hall resistance value at the $\nu = 2$ LL plateau of approximately 12.9 kΩ, was used as a building block to reach values as high as 1.29 MΩ. The superior material quality of the devices was verified by means of optical microscopy, Raman spectroscopy, and confocal laser scanning microscopy. This demonstration will greatly benefit any device manufacturing requiring outputting of more than a single quantized value of resistance. This work further helps in the design and fabrication of more complex arrays, while keeping the several experimental methods described in this thesis as ways to assess the quality of those devices.

In future work, attempts could be made to achieve a *p*-type doping with the ultimate goal of having stable *p-n* junctions on an EG device. Electron beam lithography could be performed to fabricate devices with closer and thinner contacts to further push the limits of how close we can get the contacts to be, before observing any quantum effects. Overall, my experiments have increased our understanding of the carrier interactions, contact spacing effects at a mesoscopic level and helped implement these ideas in the form of a versatile QHRS array. This work paves the way for smaller and more efficient EG device arrays to achieve a diverse range of standard resistance values.

doi:10.6342/NTU202210171

References:

[1] B.C. Brodie, XIII. On the atomic weight of graphite, Philosophical Transactions of the Royal Society of London, 149 (1859) 249-259.

[2] H.P. Boehm., A. Clauss, G.O. Fischer, U. Hofmann, Dünnste Kohlenstoff-Folien, Zeitschrift für Naturforschung B, 17 (1962) 150-153.

[3] H.P. Boehm, A. Clauss, G.O. Fischer, U. Hofmann, Das Adsorptionsverhalten sehr dünner Kohlenstoff-Folien, Zeitschrift für anorganische und allgemeine Chemie, 316 (1962) 119-127.

[4] H.P. Boehm, R. Setton, E. Stumpp, Nomenclature and terminology of graphite intercalation compounds, Carbon N Y, 24 (1986) 241-245.

[5] E.G. Acheson, Manufacture of graphite, 1896.

[6] D.V. Badami, X-Ray studies of graphite formed by decomposing silicon carbide, Carbon N Y, 3 (1965) 53-57.

[7] A.J. Van Bommel, J.E. Crombeen, A. Van Tooren, LEED and Auger electron observations of the SiC(0001) surface, Surface Science, 48 (1975) 463-472.

[8] C. Berger, Z. Song, T. Li, X. Li, A.Y. Ogbazghi, R. Feng, Z. Dai, A.N. Marchenkov, E.H. Conrad, P.N. First, W.A. de Heer, Ultrathin Epitaxial Graphite: 2D Electron Gas Properties and a Route toward Graphene-based Nanoelectronics, The Journal of Physical Chemistry B, 108 (2004) 19912-19916.

[9] A.K. Geim, K.S. Novoselov, The rise of graphene, Nature Materials, 6 (2007) 183-191.

[10] K.S. Novoselov, A.K. Geim, S.V. Morozov, D. Jiang, Y. Zhang, S.V. Dubonos, I.V. Grigorieva, A.A. Firsov, Electric Field Effect in Atomically Thin Carbon Films, Science, 306 (2004) 666-669.

[11] K.S. Novoselov, A.K. Geim, S.V. Morozov, D. Jiang, M.I. Katsnelson, I.V. Grigorieva, S.V. Dubonos, A.A. Firsov, Two-dimensional gas of massless Dirac fermions in graphene, Nature, 438 (2005) 197-200.

[12] A.H. Castro Neto, F. Guinea, N.M.R. Peres, K.S. Novoselov, A.K. Geim, The electronic properties of graphene, Reviews of Modern Physics, 81 (2009) 109-162.

[13] C. Virojanadara, M. Syväjarvi, R. Yakimova, L.I. Johansson, A.A. Zakharov, T. Balasubramanian, Homogeneous large-area graphene layer growth on $6H$-SiC(0001), Physical Review B, 78 (2008) 245403.

[14] K.V. Emtsev, A. Bostwick, K. Horn, J. Jobst, G.L. Kellogg, L. Ley, J.L. McChesney, T. Ohta, S.A. Reshanov, J. Röhrl, E. Rotenberg, A.K. Schmid, D. Waldmann, H.B. Weber, T. Seyller, Towards wafer-size graphene layers by atmospheric pressure graphitization of silicon carbide, Nature Materials, 8 (2009) 203-207.

doi:10.6342/NTU202210171

[15] C. Riedl, C. Coletti, T. Iwasaki, A.A. Zakharov, U. Starke, Quasi-Free-Standing Epitaxial Graphene on SiC Obtained by Hydrogen Intercalation, Physical Review Letters, 103 (2009) 246804.
[16] A. Tzalenchuk, S. Lara-Avila, A. Kalaboukhov, S. Paolillo, M. Syväjärvi, R. Yakimova, O. Kazakova, T.J.B.M. Janssen, V. Fal'ko, S. Kubatkin, Towards a quantum resistance standard based on epitaxial graphene, Nature Nanotechnology, 5 (2010) 186-189.
[17] M. Kruskopf, D.M. Pakdehi, K. Pierz, S. Wundrack, R. Stosch, T. Dziomba, M. Götz, J. Baringhaus, J. Aprojanz, C. Tegenkamp, J. Lidzba, T. Seyller, F. Hohls, F.J. Ahlers, H.W. Schumacher, Comeback of epitaxial graphene for electronics: large-area growth of bilayer-free graphene on SiC, 2D Materials, 3 (2016) 041002.
[18] D.M. Pakdehi, K. Pierz, S. Wundrack, J. Aprojanz, T.T.N. Nguyen, T. Dziomba, F. Hohls, A. Bakin, R. Stosch, C. Tegenkamp, F.-J. Ahlers, H.W. Schumacher, Homogeneous Large-Area Quasi-Free-Standing Monolayer and Bilayer Graphene on SiC, ACS Applied Nano Materials, DOI (2019).
[19] A.F. Rigosi, M. Kruskopf, H.M. Hill, H. Jin, B.-Y. Wu, P.E. Johnson, S. Zhang, M. Berilla, A.R.H. Walker, C.A. Hacker, Gateless and reversible Carrier density tunability in epitaxial graphene devices functionalized with chromium tricarbonyl, Carbon N Y, 142 (2019) 468-474.
[20] G.G.D. Huang, Plasmon Excitations in Mesoscopic Structures, Properties of Interacting Low-Dimensional Systems2011, pp. 83-112.
[21] S. Lee, Z. Zhong, Nanoelectronic circuits based on two-dimensional atomic layer crystals, Nanoscale, 6 (2014) 13283-13300.
[22] Y. Xu, H. Cao, Y. Xue, B. Li, W. Cai, Liquid-Phase Exfoliation of Graphene: An Overview on Exfoliation Media, Techniques, and Challenges, Nanomaterials, 8 (2018) 942.
[23] G. Deokar, J. Avila, I. Razado-Colambo, J.L. Codron, C. Boyaval, E. Galopin, M.C. Asensio, D. Vignaud, Towards high quality CVD graphene growth and transfer, Carbon N Y, 89 (2015) 82-92.
[24] A. Reina, X. Jia, J. Ho, D. Nezich, H. Son, V. Bulovic, M.S. Dresselhaus, J. Kong, Large Area, Few-Layer Graphene Films on Arbitrary Substrates by Chemical Vapor Deposition, Nano Letters, 9 (2009) 30-35.
[25] J. Coraux, A.T. N'Diaye, C. Busse, T. Michely, Structural Coherency of Graphene on Ir(111), Nano Letters, 8 (2008) 565-570.
[26] X. Li, W. Cai, J. An, S. Kim, J. Nah, D. Yang, R. Piner, A. Velamakanni, I. Jung, E. Tutuc, S.K. Banerjee, L. Colombo, R.S. Ruoff, Large-Area Synthesis of High-Quality and Uniform Graphene Films on Copper Foils, Science, 324 (2009) 1312-1314.
[27] S. Ullah, X. Yang, H.Q. Ta, M. Hasan, A. Bachmatiuk, K. Tokarska, B. Trzebicka, L. Fu, M.H. Rummeli, Graphene transfer methods: A review, Nano Research, 14 (2021) 3756-3772.
[28] I. Shtepliuk, F. Giannazzo, R. Yakimova, Epitaxial Graphene on 4H-SiC (0001) as a Versatile Platform for Materials Growth: Mini-Review, Applied Sciences, 11 (2021) 5784.
[29] F. Schopfer, W. Poirier, Graphene-based quantum Hall effect metrology, MRS Bulletin, 37 (2012) 1255-1264.

doi:10.6342/NTU202210171

[30] B. Guo, Q. Liu, E. Chen, H. Zhu, L. Fang, J.R. Gong, Controllable N-Doping of Graphene, Nano Letters, 10 (2010) 4975-4980.
[31] D. Wei, Y. Liu, Y. Wang, H. Zhang, L. Huang, G. Yu, Synthesis of N-Doped Graphene by Chemical Vapor Deposition and Its Electrical Properties, Nano Letters, 9 (2009) 1752-1758.
[32] J. Wu, L. Ma, R.M. Yadav, Y. Yang, X. Zhang, R. Vajtai, J. Lou, P.M. Ajayan, Nitrogen-Doped Graphene with Pyridinic Dominance as a Highly Active and Stable Electrocatalyst for Oxygen Reduction, ACS Applied Materials & Interfaces, 7 (2015) 14763-14769.
[33] Z. Luo, N.J. Pinto, Y. Davila, A.T.C. Johnson, Controlled doping of graphene using ultraviolet irradiation, Applied Physics Letters, 100 (2012) 253108.
[34] A.F. Rigosi, M. Kruskopf, H.M. Hill, H. Jin, B.-Y. Wu, P.E. Johnson, S. Zhang, M. Berilla, A.R. Hight Walker, C.A. Hacker, D.B. Newell, R.E. Elmquist, Gateless and reversible Carrier density tunability in epitaxial graphene devices functionalized with chromium tricarbonyl, Carbon N Y, 142 (2019) 468-474.
[35] S.M. Mhatre, N.T.M. Tran, H.M. Hill, D. Saha, A.R. Hight Walker, C.-T. Liang, R.E. Elmquist, D.B. Newell, A.F. Rigosi, Dynamics of transient hole doping in epitaxial graphene, Physical Review B, 105 (2022) 205423.
[36] H.L. Stromer, The Fractional Quantum Hall Effect, Nobel Lecture, DOI (1998).
[37] J.J. Sakurai, Modern Quantum Mechanics, 2017.
[38] C. Kittel, Introduction to Solid State Physics, 1953.
[39] C.H.W. Barnes, Quantum Electronics in Semiconductors.
[40] K.v. Klitzing, G. Dorda, M. Pepper, New Method for High-Accuracy Determination of the Fine-Structure Constant Based on Quantized Hall Resistance, Physical Review Letters, 45 (1980) 494-497.
[41] J.R. Nikolajsen, Edge States and Contacts in the Quantum Hall Effect, 2013.
[42] H. He, Engineering Epitaxial Graphene for Quantum Metrology: Uniform, Stable and Tuneable Chemical Doping, Chalmers Tekniska Hogskola (Sweden), Ann Arbor, 2018, pp. 77.
[43] M. Büttiker, Absence of backscattering in the quantum Hall effect in multiprobe conductors, Physical Review B, 38 (1988) 9375-9389.
[44] L. Schubnikow, W.J. De Haas, A New Phenomenon in the Change of Resistance in a Magnetic Field of Single Crystals of Bismuth, Nature, 126 (1930) 500-500.
[45] U. Klaß, W. Dietsche, K. von Klitzing, K. Ploog, Imaging of the dissipation in quantum-Hall-effect experiments, Zeitschrift für Physik B Condensed Matter, 82 (1991) 351-354.
[46] M. Kruskopf, A.F. Rigosi, A.R. Panna, M. Marzano, D. Patel, H. Jin, D.B. Newell, R.E. Elmquist, Next-generation crossover-free quantum Hall arrays with superconducting interconnections, Metrologia, 56 (2019) 065002.
[47] F. Delahaye, Series and parallel connection of multiterminal quantum Hall-effect devices, Journal of Applied Physics, 73 (1993) 7914-7920.
[48] A. Jeffery, R.E. Elmquist, M.E. Cage, Precision Tests of a Quantum Hall Effect Device DC Equivalent Circuit Using Double-Series and Triple-Series Connections, J Res Natl Inst Stand Technol, 100 (1995) 677-685.

doi:10.6342/NTU202210171

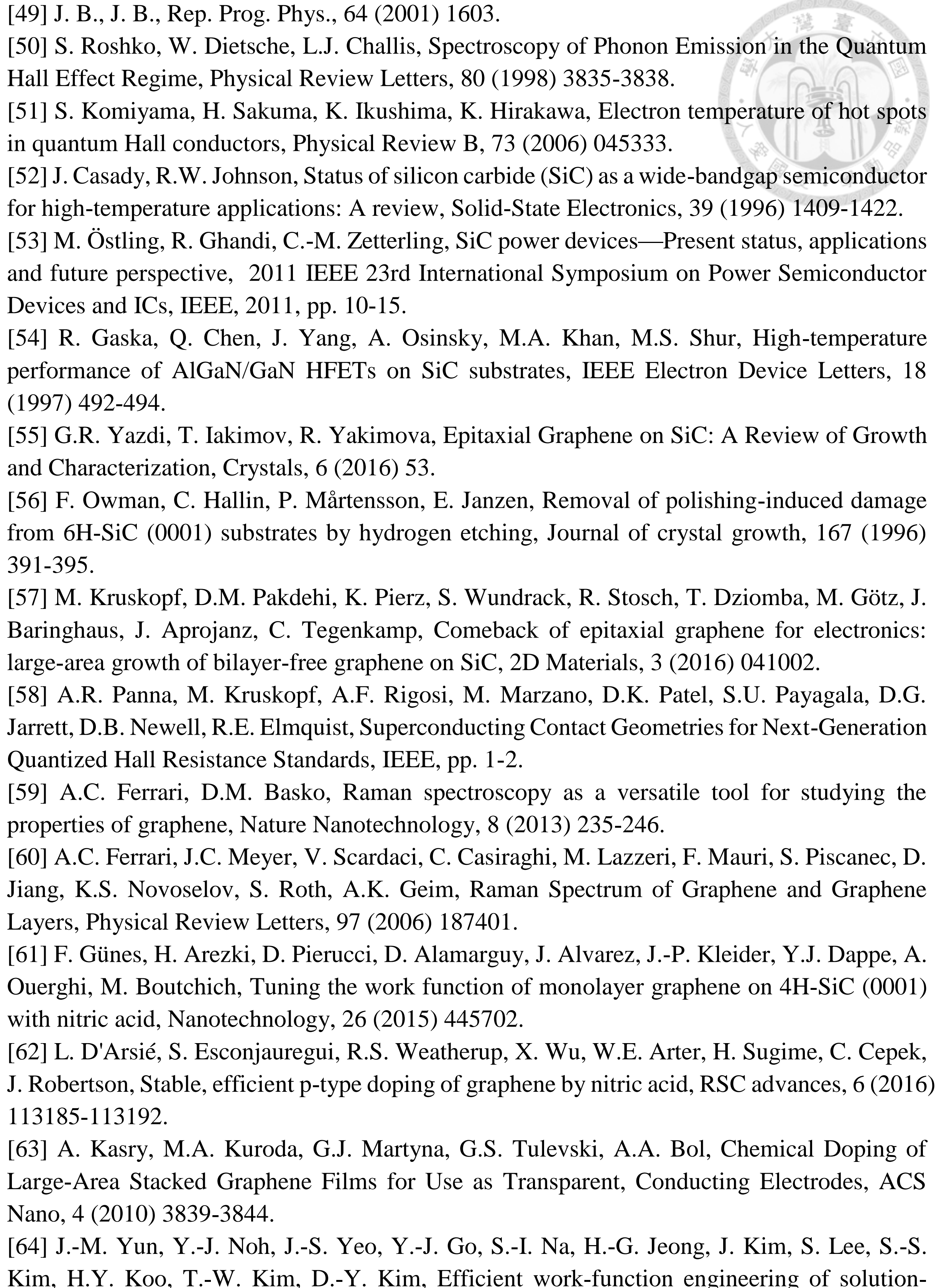

[49] J. B., J. B., Rep. Prog. Phys., 64 (2001) 1603.
[50] S. Roshko, W. Dietsche, L.J. Challis, Spectroscopy of Phonon Emission in the Quantum Hall Effect Regime, Physical Review Letters, 80 (1998) 3835-3838.
[51] S. Komiyama, H. Sakuma, K. Ikushima, K. Hirakawa, Electron temperature of hot spots in quantum Hall conductors, Physical Review B, 73 (2006) 045333.
[52] J. Casady, R.W. Johnson, Status of silicon carbide (SiC) as a wide-bandgap semiconductor for high-temperature applications: A review, Solid-State Electronics, 39 (1996) 1409-1422.
[53] M. Östling, R. Ghandi, C.-M. Zetterling, SiC power devices—Present status, applications and future perspective, 2011 IEEE 23rd International Symposium on Power Semiconductor Devices and ICs, IEEE, 2011, pp. 10-15.
[54] R. Gaska, Q. Chen, J. Yang, A. Osinsky, M.A. Khan, M.S. Shur, High-temperature performance of AlGaN/GaN HFETs on SiC substrates, IEEE Electron Device Letters, 18 (1997) 492-494.
[55] G.R. Yazdi, T. Iakimov, R. Yakimova, Epitaxial Graphene on SiC: A Review of Growth and Characterization, Crystals, 6 (2016) 53.
[56] F. Owman, C. Hallin, P. Mårtensson, E. Janzen, Removal of polishing-induced damage from 6H-SiC (0001) substrates by hydrogen etching, Journal of crystal growth, 167 (1996) 391-395.
[57] M. Kruskopf, D.M. Pakdehi, K. Pierz, S. Wundrack, R. Stosch, T. Dziomba, M. Götz, J. Baringhaus, J. Aprojanz, C. Tegenkamp, Comeback of epitaxial graphene for electronics: large-area growth of bilayer-free graphene on SiC, 2D Materials, 3 (2016) 041002.
[58] A.R. Panna, M. Kruskopf, A.F. Rigosi, M. Marzano, D.K. Patel, S.U. Payagala, D.G. Jarrett, D.B. Newell, R.E. Elmquist, Superconducting Contact Geometries for Next-Generation Quantized Hall Resistance Standards, IEEE, pp. 1-2.
[59] A.C. Ferrari, D.M. Basko, Raman spectroscopy as a versatile tool for studying the properties of graphene, Nature Nanotechnology, 8 (2013) 235-246.
[60] A.C. Ferrari, J.C. Meyer, V. Scardaci, C. Casiraghi, M. Lazzeri, F. Mauri, S. Piscanec, D. Jiang, K.S. Novoselov, S. Roth, A.K. Geim, Raman Spectrum of Graphene and Graphene Layers, Physical Review Letters, 97 (2006) 187401.
[61] F. Günes, H. Arezki, D. Pierucci, D. Alamarguy, J. Alvarez, J.-P. Kleider, Y.J. Dappe, A. Ouerghi, M. Boutchich, Tuning the work function of monolayer graphene on 4H-SiC (0001) with nitric acid, Nanotechnology, 26 (2015) 445702.
[62] L. D'Arsié, S. Esconjauregui, R.S. Weatherup, X. Wu, W.E. Arter, H. Sugime, C. Cepek, J. Robertson, Stable, efficient p-type doping of graphene by nitric acid, RSC advances, 6 (2016) 113185-113192.
[63] A. Kasry, M.A. Kuroda, G.J. Martyna, G.S. Tulevski, A.A. Bol, Chemical Doping of Large-Area Stacked Graphene Films for Use as Transparent, Conducting Electrodes, ACS Nano, 4 (2010) 3839-3844.
[64] J.-M. Yun, Y.-J. Noh, J.-S. Yeo, Y.-J. Go, S.-I. Na, H.-G. Jeong, J. Kim, S. Lee, S.-S. Kim, H.Y. Koo, T.-W. Kim, D.-Y. Kim, Efficient work-function engineering of solution-

doi:10.6342/NTU202210171

processed MoS2 thin-films for novel hole and electron transport layers leading to high-performance polymer solar cells, Journal of Materials Chemistry C, 1 (2013) 3777-3783.
[65] Z. Liu, S.P. Lau, F. Yan, Functionalized graphene and other two-dimensional materials for photovoltaic devices: device design and processing, Chemical Society Reviews, 44 (2015) 5638-5679.
[66] M. Yoshida, Y. Zhang, J. Ye, R. Suzuki, Y. Imai, S. Kimura, A. Fujiwara, Y. Iwasa, Controlling charge-density-wave states in nano-thick crystals of 1T-TaS2, Scientific Reports, 4 (2014) 7302.
[67] H.M. Hill, S. Chowdhury, J.R. Simpson, A.F. Rigosi, D.B. Newell, H. Berger, F. Tavazza, A.R. Hight Walker, Phonon origin and lattice evolution in charge density wave states, Physical Review B, 99 (2019) 174110.
[68] J. Hu, A.F. Rigosi, M. Kruskopf, Y. Yang, B.-Y. Wu, J. Tian, A.R. Panna, H.-Y. Lee, S.U. Payagala, G.R. Jones, M.E. Kraft, D.G. Jarrett, K. Watanabe, T. Taniguchi, R.E. Elmquist, D.B. Newell, Towards epitaxial graphene p-n junctions as electrically programmable quantum resistance standards, Scientific Reports, 8 (2018) 15018.
[69] B. Huard, J.A. Sulpizio, N. Stander, K. Todd, B. Yang, D. Goldhaber-Gordon, Transport Measurements Across a Tunable Potential Barrier in Graphene, Physical Review Letters, 98 (2007) 236803.
[70] J. Hu, A.F. Rigosi, J.U. Lee, H.-Y. Lee, Y. Yang, C.-I. Liu, R.E. Elmquist, D.B. Newell, Quantum transport in graphene $p\text{\ensuremath{-}}n$ junctions with moir\'e superlattice modulation, Physical Review B, 98 (2018) 045412.
[71] H. Schmidt, J.C. Rode, C. Belke, D. Smirnov, R.J. Haug, Mixing of edge states at a bipolar graphene junction, Physical Review B, 88 (2013) 075418.
[72] A.F. Rigosi, M. Marzano, A. Levy, H.M. Hill, D.K. Patel, M. Kruskopf, H. Jin, R.E. Elmquist, D.B. Newell, Analytical determination of atypical quantized resistances in graphene p-n junctions, Physica B: Condensed Matter, 582 (2020) 411971.
[73] X. Gan, R.-J. Shiue, Y. Gao, I. Meric, T.F. Heinz, K. Shepard, J. Hone, S. Assefa, D. Englund, Chip-integrated ultrafast graphene photodetector with high responsivity, Nature Photonics, 7 (2013) 883-887.
[74] F. Xia, T. Mueller, Y.-m. Lin, A. Valdes-Garcia, P. Avouris, Ultrafast graphene photodetector, Nature Nanotechnology, 4 (2009) 839-843.
[75] T. Mueller, F. Xia, P. Avouris, Graphene photodetectors for high-speed optical communications, Nature Photonics, 4 (2010) 297-301.
[76] S. Schuler, D. Schall, D. Neumaier, L. Dobusch, O. Bethge, B. Schwarz, M. Krall, T. Mueller, Controlled Generation of a p–n Junction in a Waveguide Integrated Graphene Photodetector, Nano Letters, 16 (2016) 7107-7112.
[77] J. Fang, D. Wang, C.T. DeVault, T.-F. Chung, Y.P. Chen, A. Boltasseva, V.M. Shalaev, A.V. Kildishev, Enhanced Graphene Photodetector with Fractal Metasurface, Nano Letters, 17 (2017) 57-62.

doi:10.6342/NTU202210171

[78] M.M. Elahi, K.M. Masum Habib, K. Wang, G.-H. Lee, P. Kim, A.W. Ghosh, Impact of geometry and non-idealities on electron "optics" based graphene p-n junction devices, Applied Physics Letters, 114 (2019) 013507.
[79] R.N. Sajjad, A.W. Ghosh, High efficiency switching using graphene based electron "optics", Applied Physics Letters, 99 (2011) 123101.
[80] S. Chen, Z. Han, M.M. Elahi, K.M.M. Habib, L. Wang, B. Wen, Y. Gao, T. Taniguchi, K. Watanabe, J. Hone, A.W. Ghosh, C.R. Dean, Electron optics with p-n junctions in ballistic graphene, Science, 353 (2016) 1522-1525.
[81] S. Weingart, C. Bock, U. Kunze, K. Emtsev, T. Seyller, L. Ley, Influence of the growth conditions of epitaxial graphene on the film topography and the electron transport properties, Physica E: Low-dimensional Systems and Nanostructures, 42 (2010) 687-690.
[82] N.J. Couto, D. Costanzo, S. Engels, D.-K. Ki, K. Watanabe, T. Taniguchi, C. Stampfer, F. Guinea, A.F. Morpurgo, Random strain fluctuations as dominant disorder source for high-quality on-substrate graphene devices, Physical Review X, 4 (2014) 041019.
[83] P.D. Kaushik, M. Rodner, G. Lakshmi, I.G. Ivanov, G. Greczynski, J. Palisaitis, J. Eriksson, P. Solanki, A. Aziz, A.M. Siddiqui, Surface functionalization of epitaxial graphene using ion implantation for sensing and optical applications, Carbon N Y, 157 (2020) 169-184.
[84] M.W. Nomani, R. Shishir, M. Qazi, D. Diwan, V. Shields, M. Spencer, G.S. Tompa, N.M. Sbrockey, G. Koley, Highly sensitive and selective detection of NO2 using epitaxial graphene on 6H-SiC, Sensors and Actuators B: Chemical, 150 (2010) 301-307.
[85] C. Melios, C.E. Giusca, V. Panchal, O. Kazakova, Water on graphene: review of recent progress, 2D Materials, 5 (2018) 022001.
[86] F.R. Bagsican, A. Winchester, S. Ghosh, X. Zhang, L. Ma, M. Wang, H. Murakami, S. Talapatra, R. Vajtai, P.M. Ajayan, Adsorption energy of oxygen molecules on graphene and two-dimensional tungsten disulfide, Scientific reports, 7 (2017) 1-10.
[87] S. Böttcher, H. Vita, M. Weser, F. Bisti, Y.S. Dedkov, K. Horn, Adsorption of water and ammonia on graphene: evidence for chemisorption from X-ray absorption spectra, The Journal of Physical Chemistry Letters, 8 (2017) 3668-3672.
[88] I. Silvestre, E.A. de Morais, A.O. Melo, L.C. Campos, A.-M.B. Goncalves, A.R. Cadore, A.S. Ferlauto, H. Chacham, M.S. Mazzoni, R.G. Lacerda, Asymmetric effect of oxygen adsorption on electron and hole mobilities in bilayer graphene: long-and short-range scattering mechanisms, ACS nano, 7 (2013) 6597-6604.
[89] F. Yavari, C. Kritzinger, C. Gaire, L. Song, H. Gulapalli, T. Borca-Tasciuc, P.M. Ajayan, N. Koratkar, Tunable bandgap in graphene by the controlled adsorption of water molecules, small, 6 (2010) 2535-2538.
[90] K. Maier, A. Helwig, G. Müller, P. Hille, J. Teubert, M. Eickhoff, Competitive adsorption of air constituents as observed on InGaN/GaN nano-optical probes, Sensors and Actuators B: Chemical, 250 (2017) 91-99.
[91] E.L. Cussler, Diffusion: mass transfer in fluid systems, Cambridge university press2009.

doi:10.6342/NTU202210171

[92] G. Froehlicher, S. Berciaud, Raman spectroscopy of electrochemically gated graphene transistors: Geometrical capacitance, electron-phonon, electron-electron, and electron-defect scattering, Physical Review B, 91 (2015) 205413.
[93] A. Das, S. Pisana, B. Chakraborty, S. Piscanec, S.K. Saha, U.V. Waghmare, K.S. Novoselov, H.R. Krishnamurthy, A.K. Geim, A.C. Ferrari, Monitoring dopants by Raman scattering in an electrochemically top-gated graphene transistor, Nature nanotechnology, 3 (2008) 210-215.
[94] O. Leenaerts, B. Partoens, F. Peeters, Adsorption of H 2 O, N H 3, CO, N O 2, and NO on graphene: A first-principles study, Physical Review B, 77 (2008) 125416.
[95] Z. Li, Y. Wang, A. Kozbial, G. Shenoy, F. Zhou, R. McGinley, P. Ireland, B. Morganstein, A. Kunkel, S.P. Surwade, Effect of airborne contaminants on the wettability of supported graphene and graphite, Nature materials, 12 (2013) 925-931.
[96] C.N. Santos, F. Joucken, D. De Sousa Meneses, P. Echegut, J. Campos-Delgado, P. Louette, J.-P. Raskin, B. Hackens, Terahertz and mid-infrared reflectance of epitaxial graphene, Scientific reports, 6 (2016) 1-12.
[97] A. MacDonald, P. Středa, Quantized Hall effect and edge currents, Physical Review B, 29 (1984) 1616.
[98] J. Weis, K. Von Klitzing, Metrology and microscopic picture of the integer quantum Hall effect, Philosophical Transactions of the Royal Society A: Mathematical, Physical and Engineering Sciences, 369 (2011) 3954-3974.
[99] A.C. Neto, F. Guinea, N.M. Peres, K.S. Novoselov, A.K. Geim, The electronic properties of graphene, Reviews of modern physics, 81 (2009) 109.
[100] A. Baker, J. Alexander-Webber, T. Altebaeumer, R. Nicholas, Energy relaxation for hot Dirac fermions in graphene and breakdown of the quantum Hall effect, Physical review B, 85 (2012) 115403.
[101] Oe, T., Rigosi, A.F., Kruskopf, M., Wu, B.Y., Lee, H.Y., Yang, Y., Elmquist, R.E., Kaneko, N.H. and Jarrett, D.G., Comparison between NIST graphene and AIST GaAs quantized Hall devices, IEEE Trans. Instrum. Meas., 69 (2019) 3103.
[102] R. Ribeiro-Palau, F. Lafont, J. Brun-Picard, D. Kazazis, A. Michon, F. Cheynis, O. Couturaud, C. Consejo, B. Jouault, W. Poirier, Quantum Hall resistance standard in graphene devices under relaxed experimental conditions, Nature nanotechnology, 10 (2015) 965-971.
[103] Rigosi, A.F. and Elmquist, R.E., The quantum Hall effect in the era of the new SI, Semicond. Sci. Technol., 34 (2019) 093004.
[104] H. He, S. Lara-Avila, T. Bergsten, G. Eklund, K.H. Kim, R. Yakimova, Y.W. Park, S. Kubatkin, Stable and tunable charge carrier control of graphene for quantum resistance metrology, 2018 Conference on Precision Electromagnetic Measurements (CPEM 2018), IEEE, 2018, pp. 1-2.
[105] Panna A. R., Hu I.-F., Kruskopf M., Patel, D. K., Jarrett D. G., Liu C.-I., Payagala S. U., Saha D., Rigosi A. F., Newell D. B., Liang C.-T., Elmquist R. E., Graphene quantum Hall effect parallel resistance arrays, Phys. Rev. B, 103 (2021) 075408.

doi:10.6342/NTU202210171

[106] Novikov S., Lebedeva N., Hamalainen J., Iisakka I., Immonen P., Manninen A. J., Satrapinski A., Mini array of quantum Hall devices based on epitaxial graphene, J. Appl. Phys., 119 (2016) 174504.
[107] Rigosi A. F., Patel D., Marzano M., Kruskopf M., Heather H. M., Jin H., Hu J., Hight-Walker A. R., Ortolano M., Callegaro L., Liang C.-T., Newell D. B., Atypical quantized resistances in millimeter-scale epitaxial graphene pn junctions, Carbon N Y, 154 (2019) 230.
[108] Lartsev A., Lara-Avila S., Danilov A., Kubatkin S., Tzalenchuk A., Yakimova R., A prototype of R_K/200 quantum Hall array resistance standard on epitaxial graphene, J. Appl. Phys., 118 (2015) 044506.
[109] Park J., Kim W.-S., Chae D.-H., Realization of 5 he 2 with graphene quantum Hall resistance array, Appl. Phys. Lett., 116 (2020) 093102.
[110] Momtaz Z. S., Heun S., Biasiol G., Roddaro S., Cascaded Quantum Hall Bisection and Applications to Quantum Metrology, Phys. Rev. Appl., 14 (2020) 024059.
[111] Momtaz Z. S., Heun S., Biasiol G., Roddaro S., Cascaded Quantum Hall Bisection and Applications to Quantum Metrology, Phys. Rev. Appl., 14 (2020) 024059.
[112] Rigosi A. F., Patel D. K., Marzano. M., Kruskopf M., Heather H. M., Jin H., Elmquist R. E., Newell D. B., Analytical determination of atypical quantized resistances in graphene pn junctions, Physica B, 582 (2019) 411971.

doi:10.6342/NTU202210171